Measurements of optical turbulence on the Antarctic Plateau and their impact on astronomical observations.

Author:
Travouilon, Tony

Measurements of Optical Turbulence on the Antarctic Plateau and their Impact on Astronomical Observations.

Tony Travouillon

Submitted in total fulfilment of the requirements
of the degree of Doctor of Philosophy

School of Physics
University of New South Wales

September 2004

Abstract

Atmospheric turbulence results taken on the Antarctic plateau are presented in this thesis. Covering two high sites: South Pole and Dome C, this work describes their seeing and meteorological conditions.

Using an acoustic sounder to study the turbulence profile of the first kilometre of the atmosphere and a Differential Image Motion Monitor (DIMM) to investigate the integrated seeing we are able to deduce important atmospheric parameters such as the Fried parameter (r_0) and the isoplanatic angle (θ_0). It was found that at the two sites, the free atmosphere (above the first kilometer) was extremely stable and contributed between $0.2''$ and $0.3''$ of the total seeing with no evidence of jet or vortex peaks of strong turbulence. The boundary layer turbulence is what differentiates the two sites. Located on the Western flank of the plateau, the South Pole is prone to katabatic winds. Dome C on the other hand is on a local maximum of the plateau and the wind conditions are amongst the calmest in the world. Also linked to the topography is the vertical extent of the temperature inversion that is required to create optical turbulence. At the South Pole the inversion reaches 300 m and only 30 m at Dome C. This difference results in relatively poor seeing conditions at the South Pole ($\simeq 1.8''$) and excellent at Dome C ($0.27''$). The strong correlation between the seeing and the ground layer meteorological conditions indicates that even better seeing could be found at Dome A, the highest point of the plateau.

Having most of the turbulence near the ground is also incredibly advantageous for adaptive optics. The isoplanatic angle is respectively $3.3''$ and $5.7''$ for the South Pole and Dome C. This is significantly larger than at temperate sites where the average isoplanatic angle rarely exceeds $2''$. This means that wider fields can be corrected without the complication of conjugation to specific layers. For such purpose the potential is even more

interesting. We show that ground conjugated adaptive optics would decrease the natural seeing to $0.22''$ for a wide field of $1'$ and $0.47''$ for a field of $10'$ at the South Pole. At Dome C the results are less impressive due to the already excellent seeing, but a gain of $0.1''$ can still be achieved over $10'$.

These results show that high angular resolution observations can be done better on the Antarctic plateau than any other known site.

Declaration

Acknowledgements

I never thought I'd say that, but this PhD went too fast... Time flies when you have fun and when you like what you do and the team you work with:

My first thoughts go to my supervisors Michael Burton and John Storey who have obviously done this job before since they have given me the perfect balance of autonomy and support. I want to thank them for teaching me rigor, patience, and a whole lot of grammar. In particular, Michael, thank you for the teaching skills that I hope to have picked up along with your enthusiasm to promote science to a larger audience. John, thank you for all you have done to help me develop myself professionally and your exquisite taste in films. I hope one day to be able to give public speeches of your standards (but without the help of a table...).

To the Antarctic team, thank you for being who you are: Michael Ashley, I don't know what we would have done without you. Honestly, how was I supposed to guess that to fix a corrupted compressed file all I had to do is type: "dd if=hdb BS=102983 skip=3"? To me, it makes just as much sense as a movie from David Lynch. Jon Lawrence, a great companion on every trip to Antarctica. An ideas man, that Jon: I still don't know how you got the siderostat pointing so well, but I won't forget when the star showed up on the eye piece on the first try. Paolo Calisse, the only other person in the group who understands the importance of cheese in the life of a human being. Jon Everett, a great man to work with despite his love for Alpha Romeo cars. Jessica Dempsey with whom I share the same fascination for Antarctica and who has been on that road with me since first year physics. Finally, Suzanne Kenyon who has joined us recently and who will write a sequel to this thesis.

To my colleagues and friends from the University of Nice who have been strongly involved in this work: Eric Fossat thank you for adopting me in

Contents

List of Figures

List of Tables

Chapter 1

Introduction

1.1 Motivations

The advance of modern astronomy is driven by the desire to increase spatial resolution and see deeper into our universe. Cosmologists need high photometric and spectral precision to trace the history and evolution of our universe, while other astrophysicists need higher resolution to study individual events occurring more locally.

These advances are achieved by building better instruments and larger telescopes. For example, the introduction of CCD technology allowed for the detection of fainter objects due to the high quantum efficiency (beyond 90% for CCDs compared to typically 4% for photographic plates) and for the simplification of data acquisition and storage. Similarly, the increase in telescope size has been beneficial to both light gathering power and resolution.

Unfortunately, we have long reached the point where we are limited not by our engineering capabilities, but by our own atmosphere. Its dynamic and chemical properties set the photometric and angular precision we can achieve, as well as the spectral range we can observe. The obvious solution to this problem is to place telescopes above the atmosphere. Space based telescopes such as the Hubble Space Telescope (HST) and COBE have been able to make observations currently impossible from the ground.

Putting a telescope in orbit has, however, several important drawbacks.

- First, is the obvious problem of cost. Space telescopes require funding at national or even international level. The total cost (estimated at

US$8.5 billion for HST) must include a long engineering phase, the launching, and very expensive running costs.

- Secondly, the diameter of the primary mirror is limited by the size of the space vehicle, estimated at approximately 2 m unless it can be "folded" prior to launch. This limitation is non-existent for ground based telescope with plans for telescopes of up to 100 m in diameter (OWL).

- Most importantly, the impossibility (or at least very costly) upgrade or repair of space telescopes strongly limits their life time. This is compounded by the long development of space telescopes, so that by the time of launching, much of the technology is already obsolete.

A cheaper and more flexible solution is to find on Earth locations where the effects of the atmosphere are least, in order to maximize the scientific output of a telescope. Therefore, one of the initial phases of telescope construction is the site testing campaign. Candidate sites, usually preselected by knowledge of their suitable meteorological conditions, and subjected to a more elaborate series of measurements. Over a period of time these measurements determine, with high precision, the parameters that will affect the performance of the telescope.

This manuscript describes part of a wide site testing campaign on the Antarctic plateau begun by the University of New South Wales in 1992. The objective is to assess and compare several sites on the plateau with each other and with the best astronomical sites elsewhere. In the following section is a summary and explanation of the geophysical parameters measured in site testing. The core of this thesis will focus on atmospheric turbulence. This phenomenon is often thought of as the most important as it limits the resolution of a telescope. This thesis will describe and interpret the turbulence measurements made at two Antarctic stations: the South Pole and Dome C.

1.2   Characteristics

As telescopes become larger and more precise, the requirements they place on the characteristics of the atmosphere also increase. Site testing campaigns therefore become more elaborate, measuring more quantities with better

resolution than the previous generation. Beyond the obvious requirements of low cloud cover, and minimum man-made pollution such as street lights and radio noise, the effects limiting the observations are described below.

1.2.1 Atmospheric extinction

Atmospheric extinction is due to two processes: absorption and scattering. In the absorption process a photon is destroyed by a molecule it encounters as it passes through the atmosphere, increasing the energy level of this molecule. The absorption of incoming photons in the atmosphere is dominated by the molecules H_2O, CO_2, O_2 and O_3. Rayleigh scattering results in a change in the direction of a photon as it scatters off an air molecule. Rayleigh scattering is proportional to λ^{-4}. In addition, photons can be scattered by dust and aerosols in the atmosphere.

Extinction restricts observations to spectral "windows" (see Fig 1.1). Spectral regions shorter than the optical are totally opaque because of Raleigh scattering and the absorption bands of O_2, O_3 and N_2. Only in the near ultraviolet does the first window becomes usable. This window covers the entire visible spectrum and extends to the near-infrared. Between 0.8 to 1.3 μm the sky transmission becomes spectrally intermittent because of several absorption bands of water, oxygen and carbon dioxide. The regions of low absorption, called atmospheric windows, are present up to the mid infrared. Between 15 μm and 400 μm, the atmosphere is opaque at most sites.

It is important to note the importance of the water vapor content in the atmosphere above a selected site. One of the major sources of atmospheric absorption, the water content is highly dependent on temperature and altitude. The selection of a high and cold site results in better transmission of already existing windows and can potentially open new ones. The selection criteria of other absorbers are different. Their variations are pressure dependent and may also be latitude dependent, such as O_3. It is therefore a complex combination of criteria that rules the selection of high transmission sites.
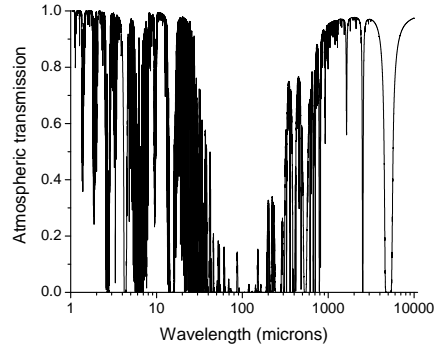
Figure 1.1: ATRAN (Lord (1993)) simulation of the sky transmission between 1 micron and 10 cm at Mauna Kea (Burton et al. (1994)).

1.2.2 Atmospheric emission

Atmospheric emission, also referred to as sky background, is caused by thermal emission of the molecules present in the atmosphere. The thermal emission corresponds to a temperature of roughly 250 K, and peaks in the infrared. This phenomenon is closely related to the process of absorption and is present in the same bands. Longward of 2 μm the thermal emission of the telescope itself can become dominant making observation increasingly difficult at higher wavelengths. Also contributing to the sky background is the radiative de-excitation of upper atmosphere atoms, also called "airglow". Located at an altitude of around 100 km, the airglow is most important in the near infrared. The fast fluctuation of the airglow is one of the strongest limitations to the photometric accuracy of ground based telescopes at these wavelengths.

The sky background can therefore be minimized by the choice of a very cold site in order to limit the thermal emission and water vapour content, and a high altitude site in order to minimize the amount of atmosphere to look through.

1.2.3 Atmospheric turbulence

Turbulence will only be briefly introduced in this section, section 3 provides more details. In astronomy, turbulence refers to optical turbulence generated in the atmosphere. The spatial and temporal variations of the refractive

index, n, change the path of light as it travels through the atmosphere, causing image motion, blurring and changes in intensity. Turbulence limits the resolving power of telescopes and is therefore one of the parameters most studied during site testing campaigns. Turbulence is usually more intense near the ground because of the thermal interaction between the ground and the local air. The cooling of the boundary layer, combined with wind shear, causes this effect. The physics of the boundary layer will be discussed in a later section. Strong turbulence can also be present at high altitude in regions where air layers of different temperatures mix. The most commonly known is the jet stream that exists at mid latitude sites and is located near the tropopause. This constantly mixes warm air coming from the equator and cold air coming from the poles.

The choice of a good site must, as an imperative, include a consideration of the amount of turbulence and its location in the atmosphere. A site with low integrated turbulence will be one that is located away from high altitude jets and has a stable boundary layer.

1.2.4 Further criteria

In the age of extremely large telescopes (ELTs), further criteria for site selection are necessary. The increase of telescope structural size added to the need for increasing engineering precision requires the ground wind speed and seismic activity of the site to be taken into account.

The effects of wind on the telescope structure are both static and dynamic. Both effects are proportional to the wind speed squared and to the surface area of the object. While the direct force onto the surface is static, the creation of local vortices generate forces perpendicular to the wind flow and can result in large amplitude oscillations. This mainly affects the steel structure of the telescope and creates disturbances at frequencies that can be lower than one Hertz. The primary mirror is subject to lesser wind speeds than the enclosure. For large telescopes however, the vibrations on the mirror can be faster than a tenth of a Hertz, strongly affecting the pointing. Beyond the operational restrictions caused by the wind, the survival requirements of telescopes are strongly influenced by the wind conditions of the site as the telescope must survive the top wind speed that may occur. This is also true of seismic activity. The level of ground acceleration has a impact on the design and therefore cost of the telescope. In the case of ELTs, these

two criteria are therefore important in the total cost of the project.

1.3 Why Antarctica?

After the list of criteria considered in the previous sections, one must wonder what type of location will give the ideal observing conditions. The first element to be considered is latitude. In order to evade the jet stream and high cloud cover, the latitudes within the tropics and below the polar circles are inclined to have better conditions. Secondly, the site must be located at a high altitude in order to evade the planetary boundary layer and minimize sky emission and absorption. Finally, the choice of the topography is to be considered. So far, island and coastal sites have been the choice of the larger facilities. Sites like Hawaii and the Chilean Atacama mountain range benefit from the unperturbed airflow coming from the sea. Inland sites can also be considered. Single peaks located within arid deserts benefit from the same airflow conditions as island sites. In addition, given that they are high enough, their atmosphere should contain a lower amount of water vapour and result in better transparency. The last type of site to be considered is the Antarctic plateau. The following section will go through the different advantages posed by this continent.

1.3.1 The near space atmosphere

First we must point to the fact that Antarctica is a large continent nearly twice the size of Australia. It is obviously cold as it lies almost completely below the southern polar circle and, equally importantly, it is the highest continent in the world. Most of the continent is covered by a plateau that peaks at an altitude of roughly 4200 metres. The combination of altitude and temperature is advantageous at several levels. The water content is minimum and observations in the infrared are strongly favored. The low pressure minimizes the opacity and the broadening of spectral lines. The low ground temperature plays an important role in the thermal emission of the telescope structure and optics , which means better sensitivity and dome seeing.

The Antarctic plateau is the driest place on earth and the middle of the continent has excellent cloud coverage conditions. It is also completely isolated from intense human activity. While there are several permanent

bases on the Antarctic coast, the plateau is almost totally unpolluted by light sources or radio signals. The region is amongst the most seismically quiet in the world and Antarctica also offers the unique opportunity of continuous observation. With the night lasting several months, it is the only continent where a telescope can track a singular object in darkness continuously and measure slowly changing events (as required in the field of astro-seismology.)

The turbulence conditions on the Antarctic plateau are the main subject of this thesis. We will investigate the characteristics of both boundary layer and free atmosphere turbulence and their implication for the performance of future observatories.

1.3.2 Brief history of Antarctic Astronomy

The advantages offered by the Antarctic continent only became apparent during the geophysical year of 1957. Motivated by the high geomagnetic latitude it was a cosmic ray experiment led by Martin Pomerantz that began modern Antarctic Astronomy (Pomerantz (2000)). First located on the coastal base of Mc Murdo, a second cosmic ray detector was moved to the South Pole in 1964. It was during this experiment that the South Pole site qualities were evaluated leading to a recommendation by Arne Wyller in 1970 to consider the South Pole as an observatory site.

In 1979 the next experiment came to life at the South Pole when a team composed of Eric Fossat, Gerard Grec and Martin Pomerantz made the first continuous measurements of the sun (Grec et al. (1980)). The experiment made an unbroken observation of 120 hours of our star in order to determine its modes of oscillation (helioseismology). This success was followed by a surge of interest to develop infrared and sub-millimeter astronomy. With the creation of the Center for Astrophysical Research in Antarctica (CARA), and its Australian counterpart JACARA (Joint Australian Centre for Astronomical Research in Antarctica - Burton et al. (1996)), the need for better site characterization became apparent. The testing started in 1994 with the measurement of the near IR brightness (Ashley et al. (1996)). As expected the results were exceptional with a sky 10 to 100 times darker than typical temperate sites. Simultaneously a collaboration between UNSW and the University of Nice led to the first turbulence measurements at the South Pole. As we will show in the following sections, this early partnership led to a comprehensive testing of the Antarctic plateau by the two institutions.

A complete expose on the history of Antarctic Astronomy can be found in Indermuehle et al. (2005).

1.3.3   The sites

The work in this thesis will cover two sites: the South Pole and Dome C. The South Pole was the first site to be characterized. Being (with Vostok) the first fully developed inland station in Antarctica, the choice of the South Pole was made for both political and logistical reasons. The station is located at the exact geographic South Pole (90°S). A separate section, called the Dark Sector and located a kilometer away from the main buildings, is set aside for astrophysical research. At an altitude of 2835 m, the South Pole is on the "western" flank of the Antarctic plateau.

In 2002, the French-Italian base located at Dome C (Candidi and Ferrari (2003)) became sufficiently developed to allow a similar characterization. As the third highest local maximum of the Antarctic plateau, Dome C (75°06.06′S, 123°20.74′E) was always regarded as a more promising site than the South Pole because of its higher altitude (3268 m) and flatter terrain.

There are plans in the future to expand the site testing to Dome A, the peak of the Antarctic plateau (more than 4200 m). It is at this place that the ultimate earth based observing conditions are expected to be found.

1.4   The AASTO: A Site Testing Philosophy

The Australian site testing campaign was debuted at the South Pole by JACARA with the measurement of the sky brightness in the near infrared in 1994 - 1996. The Infrared Photometer Spectrometer (IRPS- Ashley et al. (1996)) was originally used at the Anglo-Australian Observatory before being moved to the Pole. During the same period, the first seeing measurements were made using microthermal sensors, both tower-based (Marks et al. (1996)) and balloon-born (Marks et al. (1999)). These critical measurements lead to a more ambitious programme of site testing on several sites of the Antarctic plateau. In order to facilitate the testing of remote sites completely inaccessible for the major part of the year, the example of the AGO (Automated Geophysical Observatory, see Doolittle (1986)) was followed and improved to make the site testing completely unmanned and automated. The Automated Astrophysical Site Testing Observatory (AASTO) was born

in 1996 (Storey et al. (1996)). Designed and built like a standard AGO it was equipped with a series of instruments consuming a modest amount of power supplied to the whole building by a thermo-electric generator (50 W). The AASTO was placed in the dark sector of the South Pole station along with the G-Tower, a 5 metre tower which was linked to the AASTO and capable of fitting two small size telescopes. The data gathered by the instruments and house keeping information were transferred to Sydney on a daily basis by MARISAT satellite. The two way link it provided was also used to change instruments settings remotely.

In 2001 the site testing was exported to Dome C and the same philosophy of observation was followed. A second observatory (Lawrence et al. (2003)), the AASTINO, (Automated Astrophysical Site Testing INternational Observatory) was build using a sectional structure with modified roof tops to fit the array of instruments used for the characterization of the site. Unlike the South Pole, the Concordia station was not operational in winter during these first two years of testing. The automatization and reliability of the AASTINO was therefore greatly improved using the experience of the AASTO. In this spirit the thermo-electric generators were replaced by two Stirling cycle engines each providing 500 W of electrical power and 5 kW of heat to the building. In addition, two 150 W solar panels are used to keep the instruments powered up in case of an engine failure. Communication with the outside was made by Iridium satellite because of its lower cost of operation, lower power requirements and simpler antenna compared to the MARISAT system. In its first unmanned mission at Dome C, the AASTINO stayed alive and collected measurements for a continuous time of 143 days.

1.5   The Site Testing Instruments

The series of instruments used in the programme were the following ones:

- AFOS: The Antarctic Fibre Optic Spectrometer ((Boccas et al. (1998)) is a 30 cm telescope located on the G-Tower that feeds through a fibre optics cable to an imaging grating spectrometer with a CCD detector located inside the AASTO. The grating decomposes the light in the range 280 to 840 nm. The instrument has multiple goals: to measure the cutoff wavelength at the UV end of the spectrum, the intensity of several absorption bands and the strength of airglow and auroral line

emission. The AFOS was operational at the South Pole between 2001 - 2003 (Dempsey et al. (2004)).

- NISM: The Near Infrared Sky Monitor (Storey et al. (1999)) measures the sky brightness by performing a sky dip from horizon to horizon, sending the sky signal to a cooled filter centered at 2.379 μm. The calibration of the instrument is done by a black body of known temperature placed along the scan. The NISM operated at the South Pole in 2000 - 2001 during which time it measured the near infrared sky brightness. The low temperature of the atmosphere of Antarctica explains the low emission in the near infrared. The NISM data showed that the sky emission at 2.38 μm (K_{dark}) is on average equal to 220 μJy.arcsec^{-2} which is 20 times lower than the Maunea Kea site, giving the South Pole the lowest sky emission ever recorded for a ground-based site (Lawrence et al, 2002).

- MISM: The low level of dust, aerosol and water vapor is also an advantage present in Antarctica (Storey et al. (1999)). This effect can be seen in the mid-infrared. The mid infrared counterpart of the NISM measures the sky brightness in the wavelength range 4.3 to 14.1 μm using a circular variable filter, as well as a narrow band filter covering 10.6 to 11.3 μm to allow more sensitive measurements of this region of low sky brightness. The MISM and the NISM are both located on the roof of the AASTO sharing the same black body source. The average flux between 8.78 and 9.09 μm was 20 Jy.arcsec^{-2} as recorded in a 140 day period in 1998. The average flux profile measured between 5 and 14 microns shows that the sky background is an order of magnitude lower than at Mauna Kea (Chamberlain et al, 2000).

- SUMMIT: The sub-millimeter sky brightness is measured at 350 μm with the SUMMIT (Calisse et al. (2004)). This sub-millimeter tipper optically is identical to the radiometers jointly developed by the National Radio Astronomy Observatory (NRAO) and the Cargenie Mellon University (CMU). The mirror can rotate through 360° measuring the sky radiation as well as the temperature of the two black bodies used for calibration. Data were gathered in the winter 2001 at the South Pole base (Calisse et al. (2004)) and a median zenith opacity of 1.85 was measured at 350 μm (best 25%: 1.60, best 75%: 2.15).

The SUMMIT experiment was sent to Dome C during the summer of 2000. The first day-time measurements of the sub-millimeter sky opacity were taken. The SUMMIT recorded data between 21 December 2000 and 26 January 2001. The median zenith opacity was 1.60 during this period (Best 25%: 1.45, best 75% 1.75).

- ICECAM: One of the most important characteristics of a site for astronomy is the cloud coverage. At Dome C, we have implemented an automated CCD camera (Icecam) that is able to run continuously on batteries for a whole winter (no station power is yet available in winter). The instrument "wakes up" from an idle mode every two hours to record, compress and store a direct averaged image of the sky, giving an unambiguous picture of the sky condition. Data taken between February and November 2001 consists of 2095 images which have undergone preliminary analysis by visual inspection (Ashley et al. (2003)). Although 22% of the data were unusable due to frost or image corruption, the images showed that for the remainder of the time the sky was clear for 74% of the time while the remaining 26% showed some clouds. The Icecam will continue to record data for a few years to obtain a statistically meaningful sample.

- SODAR: One of the two instruments central to this thesis, the SODAR (SOund Detection And Ranging) follows the principles of RADAR by using acoustic waves to determine the turbulence and wind profiles in the first kilometer of the atmosphere. The SODAR has no moving parts and is therefore a very reliable instrument to make turbulence measurements in the low atmosphere. We will show that the boundary layer turbulence is critical and justifies the use of a dedicated instrument. The SODAR was situated on the roof of the AASTO throughout 2001-2002 (Travouillon et al. (2003b)) and at Dome C throughout 2003-2004 (Travouillon et al. (2003)).

- ADIMM: The second instrument used to characterize the turbulence of the high plateau is the Automated Differential Image Motion Monitor (Dopita et al. (1996)). DIMMs have become the common method to measure the integrated turbulence above a site. By dividing the light of a star into two or more sub-apertures and measuring the relative motion of the resulting images, the DIMM directly assesses the

loss of resolution arising from the turbulence in the atmosphere. The ADIMM is located on the G-tower, sharing the G-mount with the AFOS instrument. The results of the measurements made in 2002 at the South Pole will be detailed in this thesis (See also Travouillon et al. (2003a)).

Chapter 2

Meteorology of Antarctica

2.1 Generalities

Writing about the meteorology of Antarctica is a task beyond the scope of this thesis. Instead, I will concentrate on the high Antarctic plateau which is the part of the continent of interest to astronomers for the reason elaborated in this chapter. A thorough work on the climatology of Antarctica can be found in Schwerdtfeger (1984) and King and Turner (1997).

2.1.1 The Topography of the Antarctic Continent

As discussed in the introduction, one of the criteria that defines a good site is altitude. With an average elevation of 2,300 m (Schwerdtfeger (1984)), Antarctica is by far the highest continent on the planet (Asia is second with 800 m). Created by millions of years of snow accumulation, the Antarctic plateau comprises a vast desert of ice of which more than 3.5 million square kilometres is located above 3,000 m. As illustrated in figure 2.1, the plateau culminates above 4,000 m at a location called Dome A. It must be pointed that Dome A, while a prime candidate for future site testing missions, is yet to be reached by man. At a lower latitude, Dome C is another local maximum of the Antarctic plateau. Separated from Dome A by a dip where the Russian station of Vostok is built, Dome C culminates at an altitude of 3,235 m. Thanks to the development of a base undertaken by the French and Italian polar institutes, the topography of its surrounding is very well known. The region is so flat that the Concordia station is centered on a surface of approximately 400 km^2 where the elevation remains constant within 5 m
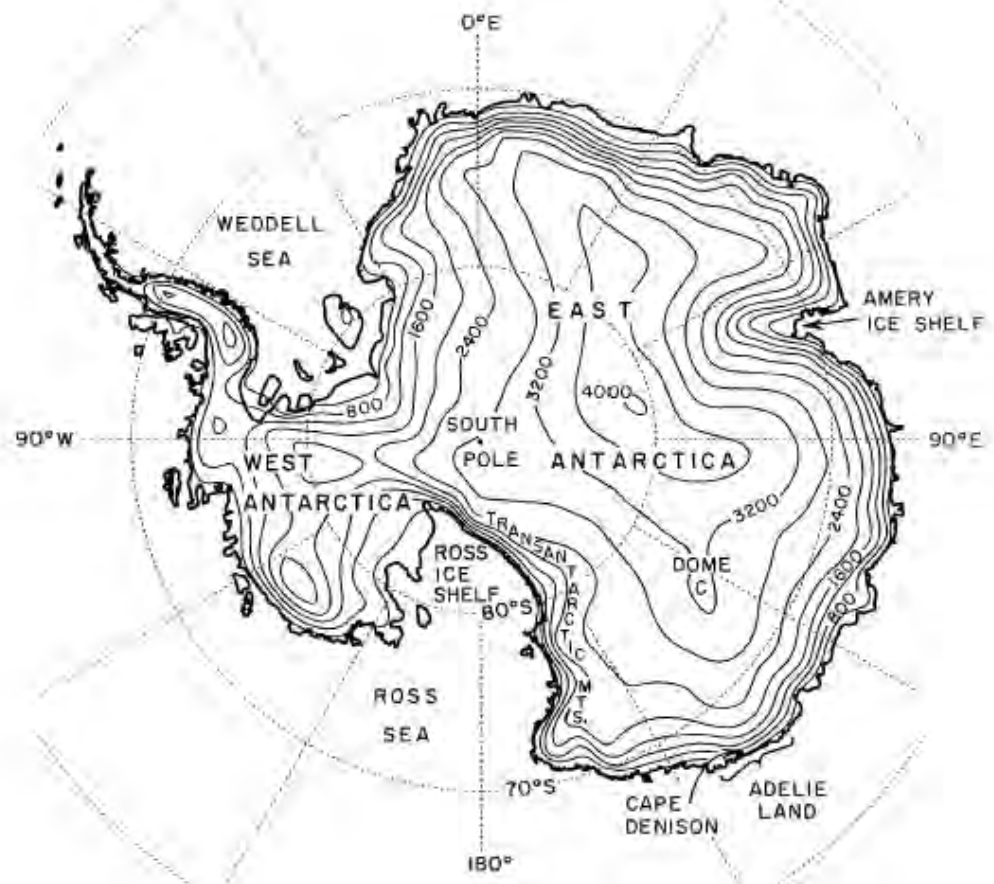
Figure 2.1: Topographic map of the Antarctic continent showing the major region of interest.(Taken from Parish and Cassano (2002))

(Tabacco et al. (2002)). Similarly, within 10,000 km^2 the elevation difference never exceeds 10 m. In general, it can be said that the Antarctic plateau is a very flat surface and its average slope (1/5000) has important implications for the climate of the continent.

It is also a particularity of interest to astronomy for more technical reasons. Long baseline interferometry may be the first niche to take advantage of the topology of the plateau. Many other sites in the world with excellent atmospheric conditions are located on high mountains that are too narrow to accommodate an interferometer of very long baseline. This issue becomes irrelevant on the plateau where the flat terrain and the lack of obstacles makes virtually any interferometer length possible. Another technical advantage of the topography resides in the telecommunication access to places like Dome C. Indeed, line of sight is required for high bandwidth microwave communication with costal sites like Dumont D'Urville or Terra Nova Bay. This level of communication is essential for large facilities where large amounts of data is collected.

2.1.2 Temperature

The importance of temperature for an astronomical site is two-fold. Firstly, the temperature dictates the strength of sky emission beyond 2.2 μm and secondly the thermal stratification of the atmosphere influences the amount of optical turbulence responsible for the loss of resolution of the telescopes. Regarding the first point is rapidly evident that the Antarctic plateau combines perfectly the two factors affecting temperature: altitude and latitude. Located almost entirely below 70° S, Antarctica is the coldest continent. It was in fact at the station of Vostok that the lowest temperature on earth, -89.6°C, was recorded. The extreme cold is largely influenced by the high albedo of ice in the infrared and its effect on the surface heat budget. This budget, unique to the Antarctic continent explains two particularities of its climate.

First, there is the strong temperature inversion present near the surface. While inversions are commonly found at night at most places, it is in Antarctica that they are the strongest, reaching up to 25°C within tens or hundreds of metres above the surface. In winter, when there is no solar radiation, most of the surface heat exchange is done radiatively. With an emissivity of almost 99% (Schwerdtfeger (1984)), the ice typically radiates

125 Wm^{-2}. The atmosphere, on the other hand, is partially transparent and emits only about 100 Wm^{-2}. This difference makes the ground cooler than the air right above it and creates the so-called inversion. The coldest temperatures and strongest inversions are found when the sky is clear as clouds also have a strong infrared emissivity. In summer, however, the shortwave radiation from the Sun is strong enough despite the larger albedo to invert the heat budget and dissipate the inversion. An example of such dissipation can be found p. 35 in Schwerdtfeger (1984). The temperature inversion also has important consequences to the air transport on the continent that will be addressed in the next section.

The second effect is what it commonly referred to as the "core-less winter" of Antarctica. As illustrated in Stearns et al. (1993) for several types of Antarctic locations, this property is common to the entire continent. The winter typically spans April to September and during this period shows consistent temperatures despite the strong daily variations due to the passage of clouds. While the prolonged absence of the Sun is important to this phenomenon, it is the low heat conductivity and capacity of the ice that leads to this fast thermal equilibrium. The core-less winter is more emphasised in the middle of the plateau, as far from the ocean there are is variation in the ground conditions. Due to the same ice properties, the summer conditions are closely matched to the Sun elevation. The hottest temperatures are usually recorded a few days after the summer solstice in contrast to mid- latitudes, the heat exchange with the ground delays the hottest day by approximately a month.

2.1.3   Surface Winds

Aided by the simplicity of the topography, the surface winds blowing on the Antarctic plateau can be easily described. Created by the temperature inversion, the motion of air mass near the surface is also qualified of inversion wind. Even for a lightly inclined terrain, the temperature gradient between two points of different elevations will gravitationally drive the air flow from the higher elevation (lower temperature) point to the lower elevation (higher temperature) one. This effect means that locations of larger slope will have higher wind speeds. Inversion winds exist everywhere on the continent but those generated on the highest parts of the plateau accelerate as they descend towards the coast. Their higher speeds informally differentiate them

as katabatic winds. Schwerdtfeger (1984) uses the following criterion as a definition. The Rossby number is defined as the ratio between the inertial and coriolis force:

$$R_0 = \frac{U^2/L}{Uf} = \frac{U}{Lf} \qquad (2.1)$$

where U is the wind speed, L is the horizontal length of the flow and f is the Coriolis parameter. Flows with Rossby number $R_0 < 1$ are classified as inversion winds while $R_0 > 1$ defines katabatic winds.

Katabatic and inversion winds have the following characteristics:

- Larger winds speeds in clear conditions

- High directionality

- Correlated with local slope

- Large change of direction with height (typical of unstable boundary layer conditions)

- Prevailing direction deviates 30 to 50 degrees from the direction of the slope

These characteristics are very positive to astronomy. Indeed, the higher points on the plateau which are already advantageous due to their lower temperatures become equally interesting because of their lower wind speeds. As seen in Fig 2.2, the three local maxima of the plateau, namely the Dome A region ($\sim$75°E), Dome F ($\sim$30°E) and Dome C ($\sim$120°E) are where the winds originate and therefore where the speeds are the lowest. While no data are available from Dome A, ample statistics have confirmed with prediction with data from Dome F (Hirasawa et al. (1999)) and Dome C (This work). This is illustrated in Table 2.1 where several plateau and coastal sites, sorted in increasing terrain slope, confirm the relationship between topography and wind conditions. On local maxima the wind speed is the lowest and the direction highly variable due to the lack of clearly defined slope. As one goes down the plateau the slope increases along with the wind speed and directionality.

As we will see in a later chapter, the surface wind speed is strongly correlated with the low-atmosphere turbulence. This is a region of the atmosphere that contributes strongly to the total degradation of a telescope's

Table 2.1: Surface wind conditions at several places in Antarctica, adapted from Schwerdtfeger (1984).

Station	Description	Wind speed (m/s)	directional consistency (%)
Dome C	local maximum	2.9	45
Vostok	high	5.1	81
South Pole	near local maximum western flank of the E. plateau	5.8	79
Byrd	small slope western plateau	7.7	86
Denison	medium slope coastal, large slope	19.5	97
	large slope		
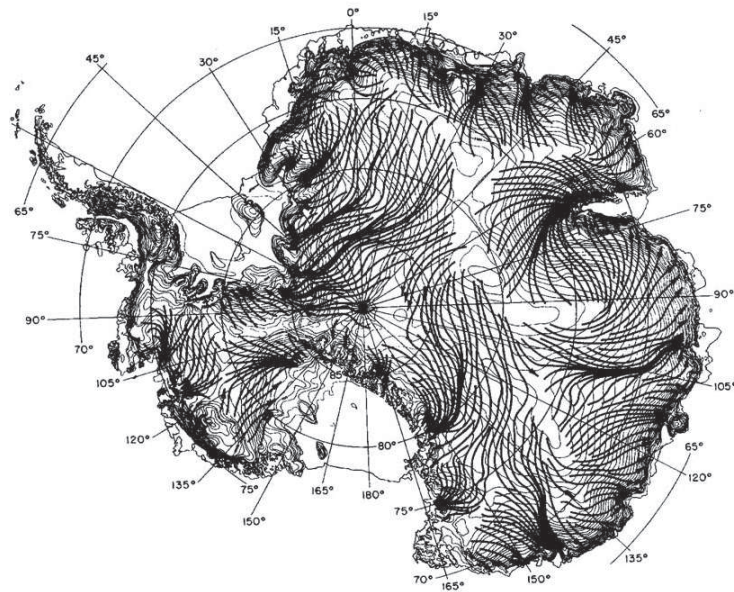
Figure 2.2: Katabatic flows on the Antarctic continent (Taken from Parish and Bromwich (1987)).

resolution because it is in this region that the pressure is the largest and the thermal exchange the more important. A low wind site is therefore expected to have better boundary layer turbulence conditions.

2.1.4 High Altitude Winds: The Polar Vortex

While knowledge of the surface wind conditions are crucial to both structural and turbulence issues, the high-altitude winds are also important as they may trigger turbulence responsible for poor isoplanatic angles. Temperate sites suffer from high altitude turbulence created by the mixing of cold air coming from the poles and warm air coming from the equator such as the jet stream or other mesoscale system caused by their topography and location. Such systems are essentially absent on the Antarctic plateau and represent another of the key advantages of Antarctica.

Arising from a large temperature gradient between the coast and the open ocean, a quasi-perfect geostrophic wind known as the polar vortex circles the Antarctic continent. Highly decoupled from the boundary layer, the vortex is not centered on the South Pole but closer to the center of mass of the continent. This almost purely geostrophic wind creates a barrier that protects the plateau from the intrusion of jets. In sub-polar regions, the speed of the vortex decreases with increasing latitude. Since turbulence is created by large wind speed gradients, sites located well within the vortex will present less turbulence at these altitudes. It is important to note the difference of behaviour of the vortex above and below the tropopause. In the troposphere, the seasonal variation of the vortex is minimal and the wind gradually increases in speed. In the stratosphere, however, the wind speed gradually levels out or decreases in summer but increases again in the winter months, peaking in September at the top of the stratosphere. A good example of such a seasonal variation can be found on p 132 of Schwerdtfeger (1984).

Again the conclusion to draw for astronomy is straightforward. In the centre of the plateau, the protection from the vortex is maximum while the high altitude wind speed remains low. We will now investigate in more details the meteorology of the two sites selected for this work. The data we present from the South Pole was gathered by the local meteorological team since 1957 and taken from multiple quoted references. For Dome C, parts of the data presented come from the Automated Weather Station (AWS) since

1984 and were analysed by Christian Meyer and John Storey. The balloon data were gathered in a collaborative work with the University of Nice and the participation of the University of Idaho (Aristidi et al. (2005)). The contributions of the author to this paper include data gathering, interpretation and writing.

2.2   South Pole

The first of our two target sites, the South Pole, has very well characterised meteorological conditions. A year-round meteorological team has been present at the South Pole since 1957 when the station was first opened for winter. The opening was chosen to coincide with the International Geophysical year and, not so surprisingly considering the political climate, the same year as the Russian station Vostok.

   While not on the highest part of the plateau, the South Pole is still at a respectable height of 2835 m and a mean pressure of 680 millibars. The annual mean temperature is -49°C, -28°C in summer and -58°C in winter. The monthly averages are shown for both South Pole and Dome C in Fig 2.3. At both sites the core-less winter represents about 6 months of the year of quasi-constant temperatures. The larger variation observed on the Dome C data comes from the smaller statistical sample. The long period of extremely cold temperatures is remarkable for telescope sensitivity (Lawrence (2004)). It is interesting to note that while Dome C winter temperatures are lower because of the altitude difference, South Pole has the longest winter because of its latitude. A compromise must therefore be made between sensitivity and total observation time below a given sky brightness.

   The effect of temperature on telescope sensitivity has already been measured in the infrared (Lawrence et al. (2002b)) and sub-millimeter (Peterson and Radford (2003)). However, temperature gradients are also important to study the resolution limit that can obtained at the South Pole. It was pointed out by Marks et al. (1999) using daily weather balloon profiles that besides the usual tropopause temperature gradient, the only temperature variation capable of generating turbulence at the South Pole was located in the boundary layer. Indeed the South Pole is located well within the circumpolar vortex and is protected from high altitude jet streams. As shown in Fig 2.4, the boundary layer inversion extends several hundred meters from
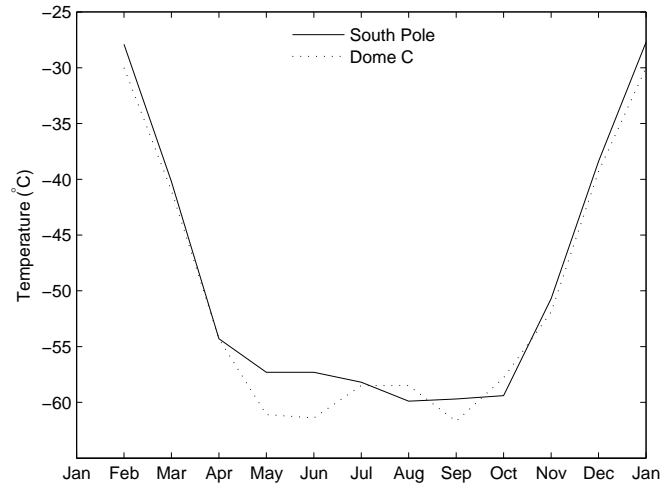
Figure 2.3: Monthly average temperatures at South Pole (26 year average) and Dome C (5 year average)

the ground. This region is where strong turbulence is located as was confirmed by Neff (1981) and Travouillon et al. (2003b). The strength of the inversion is between 20°C and 25° which is comparable to what is found in the highest points of the plateau. However, it is the physical extent of the large gradient which is the biggest problem as, varying between 100 and 600 m, it is too high to be eliminated artificially. The inversion is present 10 months a year. It only disappears in December and January when the Sun's radiation is strong enough to warm the ground and equilibrate the heat budget.

The effect of the inversion at the South Pole is, as discussed earlier, completely correlated with the ground wind speed. As shown in Fig 2.5, the mean wind speed rapidly increases when the the temperatures drop at the beginning of winter and remain high until the core-less winter ends in October. With a yearly average of 5.5 m/s, the South Pole wind, which can be classified as katabatic, flows in from the slopes of Dome A. It is strong compared to higher altitude station in Antarctica like Dome F (2.6 m/s) or Dome C (2.8 m/s) but is comparable to the wind speed of other astronomical observatories (see Table 2.2). The effect of the combined inversion and katabatic wind on turbulence is one of the main studies of this thesis and
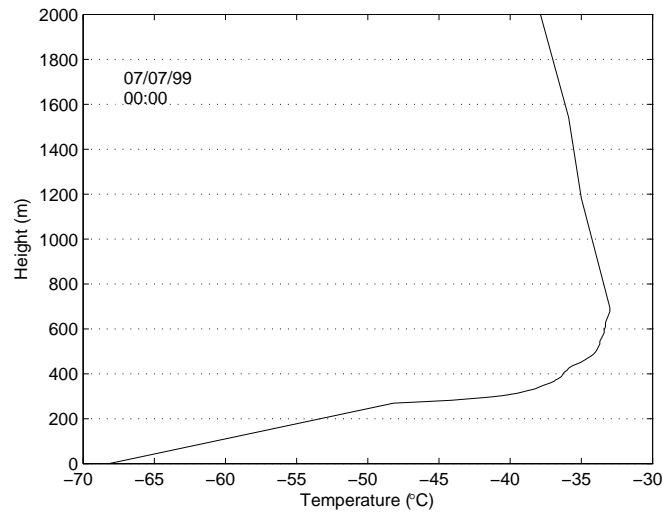
Figure 2.4: Typical winter temperature profile at South Pole taken with a balloon borne radiosonde.

will be properly quantified in a later chapter using acoustic sounding.

Site	Wind speed (m/s)	Reference
Dome C (1984-1995)	2.7	Aristidi et al. (2005)
Dome C II (1996-2003)	3.2	Aristidi et al. (2005)
Dome C plus Dome CII (1984-2003)	2.9	Aristidi et al. (2005)
Maidanak	2.1	Ehgamberdiev et al. (2000)
Mauna Loa	4.4	Barnes (2004)
La Silla	4.6	Hainaut (2004)
South Pole	5.5	Mefford (2004)
La Palma	6.6	La Palma (2004)
Paranal	6.6	Hainaut (2004)

Table 2.2: Mean wind speeds at Dome C and other astronomical sites for which long-term data exist.

2.3 Dome C

Being potentially a better site than the South Pole because of the higher altitude and the flatter surface, Dome C is the current subject of a thorough site testing campaign. We present in this section the results of the
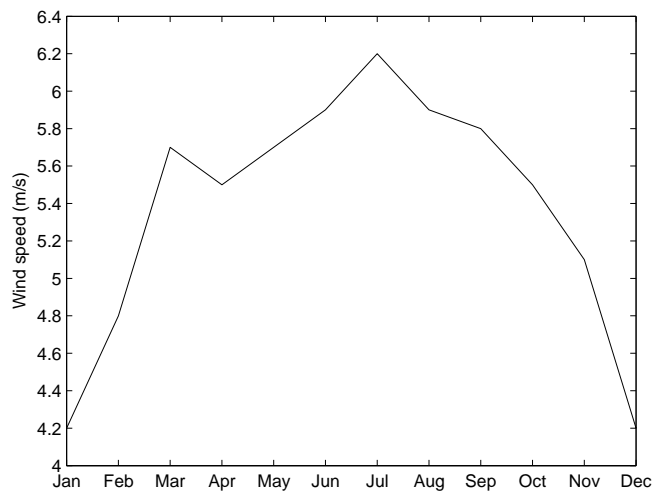
Figure 2.5: Mean monthly wind speed at the South Pole (1977 to 1998).

meteorological data obtained at Dome C.

2.3.1 Data acquisition

Weather sondes

The data were acquired at the Dome C station (75°06′S 123°19′E) using balloon-borne weather sondes (model RS80 and RS90) manufactured by Vaisala. The sonde measures wind speed and direction by GPS triangulation as well as temperature, pressure and humidity from its in-built sensors. The humidity data will not be presented in this paper due to inconsistencies between the two types of sondes and their inaccuracies in this temperature regime.

The data were taken between November and February over four seasons (2000-2004) with a good statistical coverage of all sun zenith angles. Fig 2.6 shows the daily and monthly distribution of the sample used in this paper, consisting of a total of 145 successful balloons launches. The inversion layer, which is usually very low at Dome C, has been further sampled using captive sondes. These measurements were motivated both by the irregularity of the temperature data within the first few tens of metres of the balloon launch and by the importance that this part of the atmosphere has to astronomical

Figure 2.6: Time distribution of the measurements as a function of hour of the day and month.

site testing. The boundary layer is typically a major contributor to the seeing. It is therefore crucial to obtain numerous and accurate measurements of the temperature and wind profile of the low troposphere. The captive sonde temperature data were obtained by attaching the sonde to a pulley and raising it up to the top of a 30 m tower. The sonde was then slowly pulled down while the measurements were taken.

As each balloon explodes at a different height, the analysis of the next sections precludes data above altitudes for which the statistical noise dominates because the number of sonde data is low. This altitude varies depending on the type of data and the time span of the particular analysis. Typically, the analysis range reaches to between 16 km and 20 km.

2.3.2   Results

In the following sections, the height is defined with respect to the Dome C ice level rather than the altitude above sea level (unless specified).

Wind speed and direction

On the Antarctic continent, the wind profile is characterized by two phenomena. At the surface, katabatic winds descend from the high plateau and
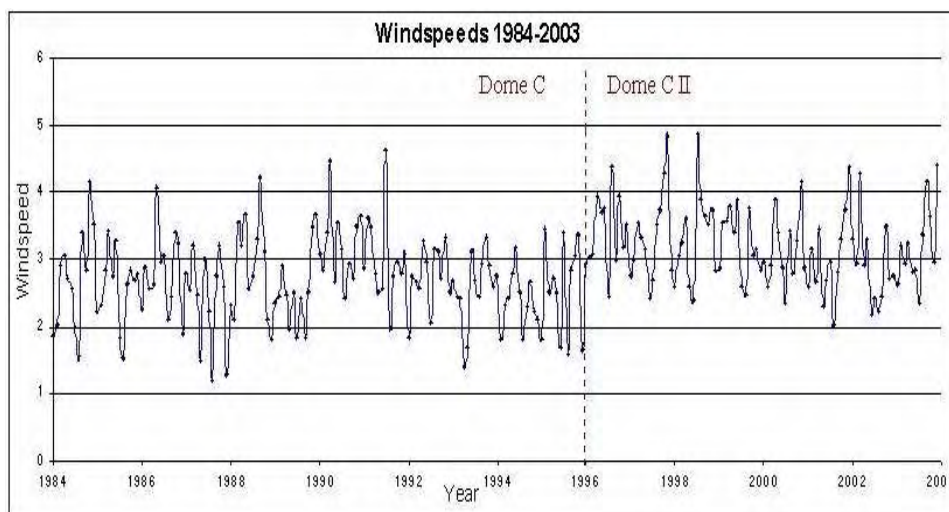
Figure 2.7: Mean monthly wind speed at Dome C and Dome C II from the beginning of 1984 to the end of 2003 (courtesy of C. Meyer).

increase in speed as they reach the coast. Similar to inversion winds, their speed is closely related to the slope of the local terrain. At Dome C, where the slope is near zero the ground speed is very low (2.9 m/s average). In Fig 2.7 we present the mean wind speed for each month from the beginning of 1984 to the end of 2003.

Dome C being a point of origin, the prevailing wind is not as consistent as it is along the slope of the plateau (see Fig 2.8). The prevailing inversion wind points North, however, towards the coastal base of Dumont D'Urville and along the direction of greatest slope. Wendler et al. also report the wind conditions using several AWS between the two stations showing increasing wind speeds toward the coast and very consistent directionality.

The wind speed profile (see Fig 2.9) is ruled by the second phenomenon that characterises the wind conditions in Antarctica, the circumpolar vortex. In sub-polar regions, the speed of the vortex decreases with increasing latitude. In the troposphere, the seasonal variation of the vortex is minimum while in the stratosphere the vortex increases in speed in winter. This is demonstrated in Fig 2.12. While winter-time data do not yet exist, our first measurement from mid-November show speeds of up to 40 m/s at 20 km altitude. After early December the stratospheric wind drops and rarely exceeds 10 m/s. This behavior has also been observed at a latitude of 60°S
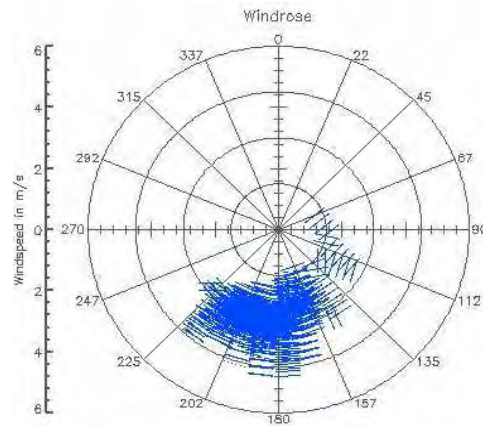
Figure 2.8: Wind rose, showing the probability that the wind will be of a particular speed and in a particular direction, for Dome C and Dome C II combined, for the same period as in Fig 2.7 (courtesy of C. Meyer).
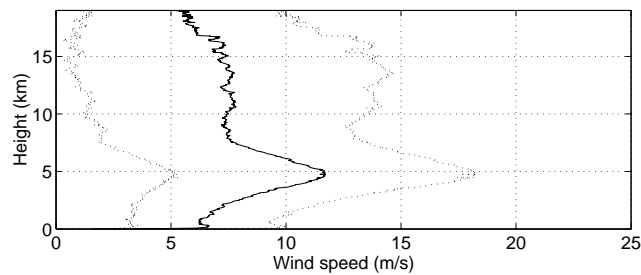
Figure 2.9: Mean wind speed profile at Dome C. The two outer lines delimit the standard deviation

(see Fig. 4.8., p132, in Schwerdtfeger (1984)). To observe such a large stratospheric wind speed at the latitude of Dome C is unexpected and is likely a rare event triggered by the breaking of the vortex in 2002-2003, as suggested by Chanin (2003).

Fig 2.10 shows the wind statistics at 200 mB, corresponding to an altitude of 7 km above Dome C. The wind speed at this altitude is often taken as a reference altitude in site testing. Usually corresponding to the mean turbulence-weighted altitude of several Chilean sites, it has been found that the wind speed at this altitude is inversely related to the coherence time of the site (Vernin (1986)). While it remains to be shown that the mean turbulence altitude at Dome C is at 200 mB, we will show in section four

	Dome C			
	ground	*trop.-330mB*	*200mB-11km*	*50mB*
N data	8741	145	123	75
Mean w speed	3.6	12.2	7.4	6.6
Med. w speed	3.5	10.7	5.9	4
W speed std dev	2.5	7.2	5.3	6.1
Max w speed	10.5	41	25.7	34.4
Mean direc.	180.3	187.6	211.6	193
Direc. std dev	74.4	92.6	90.8	121.6
	South Pole			
	ground	*trop.-330mB*	*200mB-11km*	*50mB*
N data	668	666	662	621
Mean w speed	4.7	10	7	9.2
Med. w speed	4.5	8.1	5.7	4.7
W speed std dev	2	7	4.9	9.6
Max w speed	13	47.8	35.4	56
Mean direc.	105.9	213.7	203.6	155.3
Direc. std dev	112.3	113.3	114.4	100.4

Table 2.3: Wind statistics at Dome C and South Pole over the period of time covered by the balloon launches.

that at least part of the turbulence is generated at this altitude. With a mean of 7.6 m/s, the summer time tropopause wind at Dome C is much lower than at typical mid-latitude sites during the same season. At Mauna Kea and Paranal, for example, the mean 200 mB wind speeds in December are 24.7 m/s and 22.2 m/s respectively (Vernin (1986)). While we do not have Dome C data in the middle of winter, it is known that at this latitude, the vortex does not normally vary greatly with seasons (see Fig. 4.8., p132, in Schwerdtfeger (1984)).

A site testing campaign having been carried out at the South Pole station, a comparison of the wind conditions at the two sites is now possible. Table 2.3 gives the winds statistics of Dome C and South Pole. Note that the two data sets use AWS data for the ground values and cover the same period as the balloon data.

At ground level, the wind speed is lower at Dome C. This is explained by the difference of slope between the two sites. Located on a local maximum, Dome C is rarely affected by katabatic winds. At the South Pole the gentle slope drives the surface wind from higher points of the plateau. The very
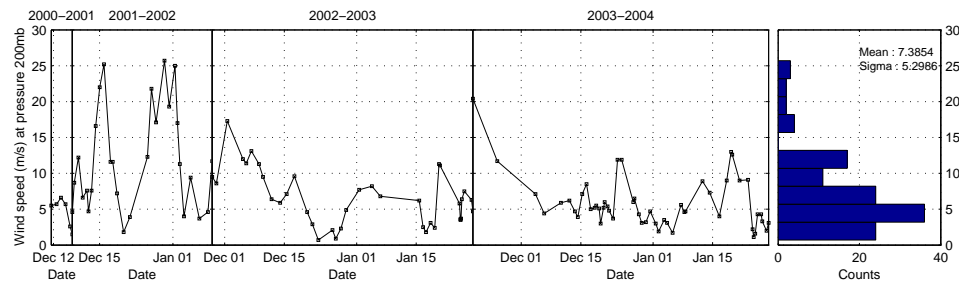
Figure 2.10: 200mB wind speed distribution at Dome C (Aristidi et al. (2005)).
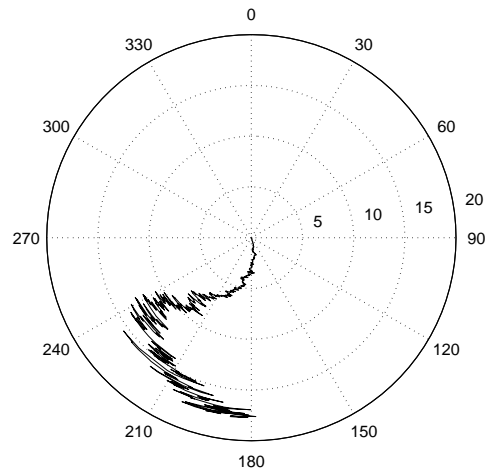
Figure 2.11: Average wind direction profile as a function of altitude at Dome C (Aristidi et al. (2005)).

low average wind speed and the absence of strong gusts makes Dome C a very suitable location for the building of an observatory.

Up to an altitude of 14 km the wind direction is very stable, slowly moving from a south to a south-easterly direction (see Fig 2.11). This direction follows the topological wind flow pattern described in Parish and Bromwich (1987). Above 14 km, an abrupt change is observed, the wind moving rapidly clockwise. This effect is probably due to the sonde traveling north and eventually being caught by the stratospheric vortex that circles the continent in the same direction.

Compared to other well known astronomical sites, the wind speed profile at Dome C is very encouraging. Fig 2.12 shows a typical summer (full line)
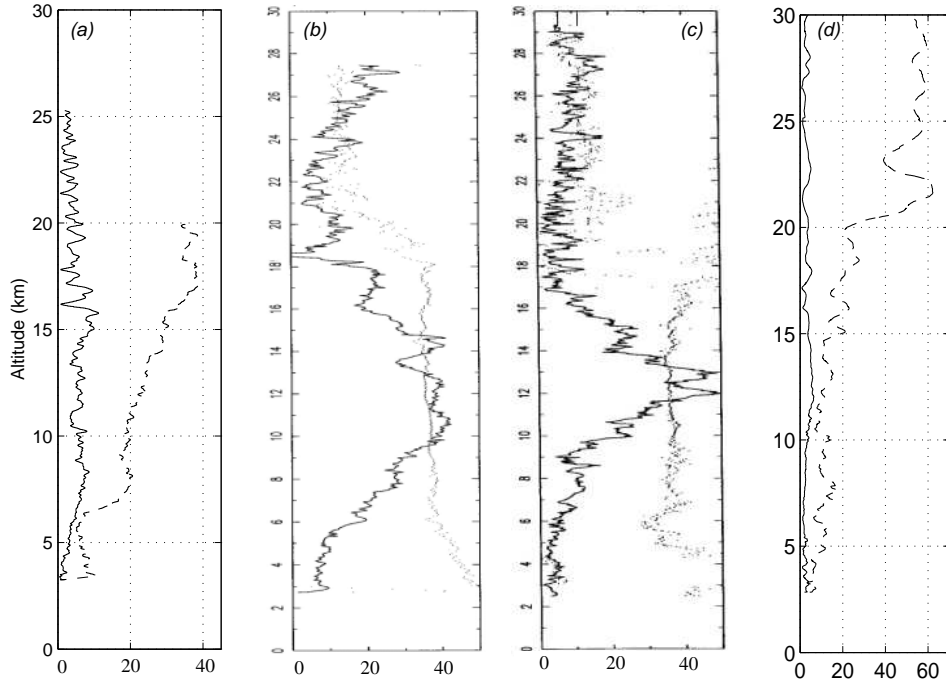
Figure 2.12: typical wind speed profiles at (a) Dome C, (b) Paranal (Chile), (c) Mauna Kea (Hawaii) (d) and South Pole. In the case of the Dome C and South Pole, the profile in dashed line is representative of the end of winter while the full line is a typical summer profile. Note: the altitude is here expressed from sea level. The Paranal and Mauna Kea plots are courtesy of J. Vernin. The South Pole data is courtesy of the local meteorological team.(Aristidi et al. (2005)).

and end of winter (in dash) profile at Dome C and at South Pole compared with typical profiles at Mauna Kea and Paranal. In the temperate sites, the jet stream is clearly observed at an altitude of 12 km where the most intense turbulence of the free atmosphere normally occurs. The Antarctic sites have very flat summer profiles with no presence of high altitude winds. Our first measurements taken in mid-November can be interpreted as a good indication of the winter conditions. Due to the presence of the stratospheric vortex, wind speeds show a broad peak at an altitude of 20 km, substantially higher than at temperate sites.
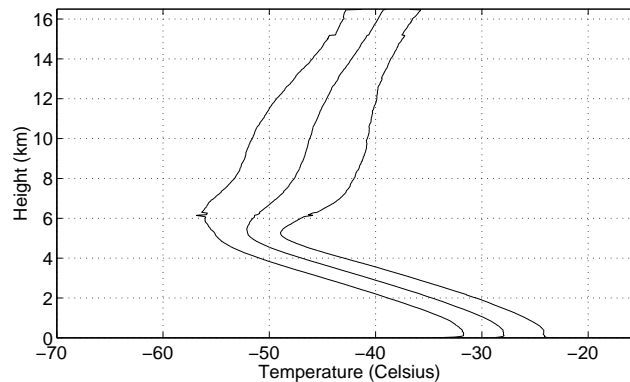
Figure 2.13: Mean temperature profile at Dome C. The two outer lines delimit the standard deviation.

Temperature

The average temperature profile for Dome C is presented in Fig 2.13. The tropopause, defined by the minimum temperature gradient, is found at a height of 5.5 km (330 mB) above the ice and followed by a very brief isothermal layer less them 1 km wide. This feature is known to be less evident in winter from South Pole observations when the stratosphere cools. An analysis by time period shown in Fig 2.14a demonstrate the stability of the troposphere temperature profile. Larger thermal fluctuations are observed in the stratosphere. More important to astronomical sites is the strength and depth of the inversion layer. This is particularly true at the South Pole, where a large majority of the seeing is generated within the boundary layer, as shown at the South Pole (Travouillon et al. (2003b), Marks et al. (1999)). Fig 2.14b shows the inversion layer at Dome C as a function of time of day. In winter we expect the inversion to resemble that of the summer night time measurement with a more pronounced temperature gradient. The important point to note is the narrow depth of the inversion. Extending to only 50 m this is much lower than the boundary layer at the South Pole (220 m, Marks et al. (1999)) or Vostok (300 to 500 m, King and Turner (1997)). While the seasonal variation of the inversion depth is unknown, it is unlikely that it will increase greatly due to the geographical location of Dome C. King and Turner (1997) have measured larger variations on coastal stations than inland ones.

In order to further investigate the temperature profile of the boundary
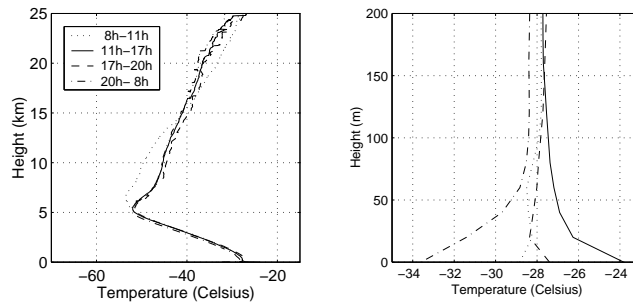
Figure 2.14: Temperature profiles for different local time periods. The second graph focuses on the inversion zone.

layer, we have launched balloons at two-hourly intervals during two days of 2003 and 2004. We have chosen the two days to be almost exactly a year apart to make the data more comparable. Fig 2.15 shows the temperature profiles of these two days as well as representative data measured using sensors pulled down from the 30 m tower.

Balloon borne sondes can measure up to ten points in the first 30 m while the number of point obtained from the tower experiment is only limited by the speed at which we pull the sonde (we typically obtained 4 points per metre). The results show that the two methods are in good agreement. The inversion starts to become apparent at roughly 8:00 pm LT and remains trapped below 30 m until midnight where the largest gradient is observed in the first 20 m. It then rises in altitude reaching a maximum of 90 m, its gradient losing in intensity. Finally the inversion dies out as the sun warms the surface and equilibrates the surface layer at around 2 pm.

2.3.3 Discussion and conclusion

Wind speeds at Dome C are extraordinarily low, particularly in view of the fact that it is the highest point for several hundred kilometers. Both peak and average wind speeds are less than half that at most other sites, delivering a major advantage to both telescope designers and astronomers. For a substantial fraction of time the wind speed at Dome C is zero; in 1990, for example there was no wind at all for 6% of the darkest hours of the year. (An even larger fraction of zero-wind time occurs in 1984; however this appears to be an anomaly.)
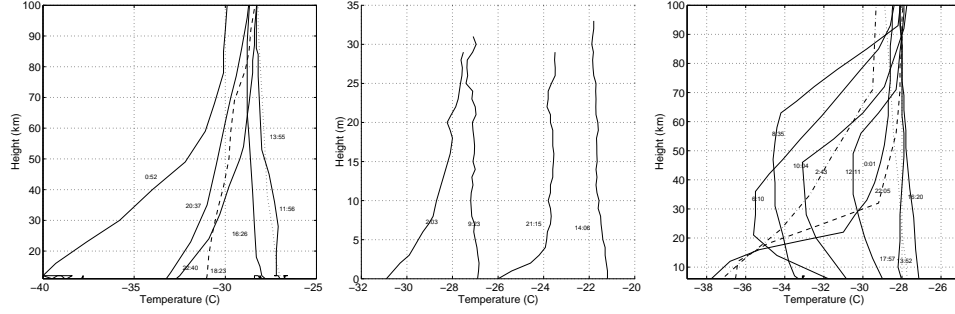
Figure 2.15: Left: temperature profiles taken at regular intervals on the 25/01/03; Center: temperature profiles representative of the indicated hour measured using a pulley; Right: temperature profiles taken at regular intervals on the 24/01/04.

It is, however, the combination of a low boundary layer and a remarkably stable free atmosphere that makes Dome C such a strong candidate for future large observatories. The mid-infrared sky brightness at Dome C one or two orders of magnitude lower than observed at typical mid-latitude sites (Walden et al. (2005)) and the sub-millimeter opacity is significantly lower than at mid latitude sites and comparable to the South Pole (Calisse et al. (2004)). A thorough study of the turbulence profile is necessary to determine the performance that can be obtained with and without adaptive optics.

Preliminary turbulence information can be inferred from the meteorological data. The computation of the Richardson number throughout the atmosphere is a good indicator of the generation of optical turbulence and of its location. The following criterion is usually stated as a condition of formation of turbulence:

$$R_i = \frac{g}{\theta} \frac{(d\theta/dz)}{(dU/dz)^2)} < \frac{1}{4} \qquad (2.2)$$

where the Richardson number is R_i, g is the gravitational constant and $d\theta/dz$ and dU/dz are the potential temperature and wind speed gradients with respect to altitude. The potential temperature is defined as:

$$\theta = T \, (\frac{1000}{P})^{0.286} \qquad (2.3)$$

and its vertical gradient is an indicator of layer stability if non-negative.

Wind speed gradient is

$$\frac{dU}{dz} = \sqrt{\left(\frac{dU_x}{dz}\right)^2 + \left(\frac{dU_y}{dz}\right)^2} \qquad (2.4)$$

with U_x and U_y the two components of the wind speed vector. Gradients are computed as follows: altitudes are sampled with 100 m interval in which a linear interpolation of $\theta(z)$, $U_x(z)$ and $U_y(z)$ is performed. Calculated slopes are taken as the gradients. In Fig 2.16 we have plotted two typical gradients profiles as well as the inverse of the Richardson number. The vertical line (at 4) indicates the limit beyond which turbulence can be generated. It was found that turbulence was almost systematically present in the boundary layer during periods of inversion due to the sharp temperature gradient. In the free atmosphere, however, conditions of turbulence generation are few and spatially thin. The only peak found commonly in the free atmosphere is usually found between 5 and 7 km corresponding to the top of the tropopause. These results also show that some turbulence is generated in the boundary layer. This is expected as the measurements are taken in daytime where the boundary layer is usually convective. In winter the boundary layer turbulence will be different and it will necessary to determine intensity and the spatial extent of the boundary layer turbulence.

The inescapable conclusion is that Dome C offers a remarkable opportunity for the construction of large and novel telescopes. If the results of these initial investigations are confirmed, Dome C could be an ideal site for the next generation of Extremely Large Telescopes (Lardiere et al. (in press); Angel et al. (2004)). By making a direct comparison between the South Pole and Dome C we can really understand the impact that the extra altitude and flatter surface had on the meteorological conditions. As we will discover in the following chapters the effect of the katabatic flow is the main factor of loss of resolution at the Pole. We can therefore expect that the best observing conditions will be found at Dome A, the highest point of the plateau.
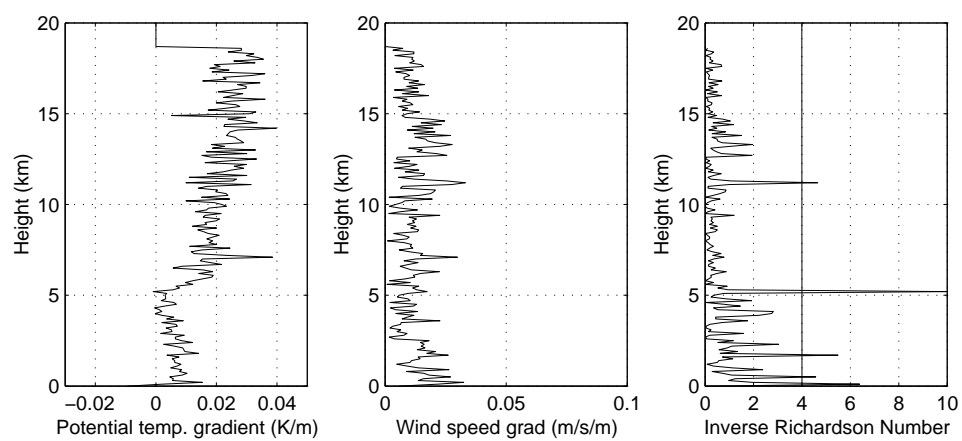
Figure 2.16: Temperature gradient, wind speed gradient and Richardson number profile for a typical data set.

Chapter 3

Theory of Turbulence

In this chapter we will review the main features of the theory of turbulence. Commonly defined as random velocity fluctuations appearing on different scales, turbulence is created at the boundary of two laminar flows or between a laminar flow and a hard surface. While turbulence in simple systems can be described by fluid dynamics, it requires a statistical approach in the atmosphere. After briefly introducing the conditions under which turbulence is generated, we will look into the models that help us quantify the effect of the atmosphere on our telescope image. A complete review and derivation of turbulence theory and of its applications in astronomy can be found in Roddier (1981). Before applying this to turbulence, we first need to define two functions:

1. the structure function that can be interpreted as the mean square difference in the value of some parameter between two points of separation r:

$$D(r) = \langle (f(x) - f(x+r))^2 \rangle = \int_{-\infty}^{\infty} dx \ (f(x) - f(x+r))^2. \quad (3.1)$$

2. the covariance function, which is also called auto-correlation function:

$$B(r) = \langle f(x)f(x+r) \rangle = \int_{-\infty}^{\infty} dx \ f(x)f(x+r). \quad (3.2)$$

These two functions are extensively used when dealing with the propagation of a wave through a turbulent medium and can be related to each

other by simply developing the square in the structure function:

$$D(r) = 2[B(0) - B(r)]. \tag{3.3}$$

3.1   Formation of Optical Turbulence

Optical turbulence in the atmosphere requires the conjunction of two phenomena: dynamical turbulence (which is described in the next section) and an inhomogeneous refractive index (Vernin (2002)). The latter point implies that optical turbulence requires the mix of air parcels at different temperature, pressure or chemical makeup. In a non-isothermal fluid, such as the atmosphere, the generation of turbulence is ruled by the Richardson number R_i. It is defined as the ratio of the gravitational potential energy to the kinetic energy. The potential energy of a fluid element of size Δh per unit mass (also called buoyancy) is given by:

$$E_p = g\Delta\rho\Delta h \tag{3.4}$$

where $\Delta\rho$ is the variation of density. The kinetic energy of the same fluid parcel is given by:

$$E_k = \rho\Delta V^2 \tag{3.5}$$

where ΔV is the wind speed of the parcel. Taking the ratio of these two energies the Richardson number can be written:

$$R_i = \frac{\frac{g}{\rho}\frac{\Delta\rho}{\Delta h}}{(\frac{\Delta V}{\Delta h})^2}. \tag{3.6}$$

Consider now a situation where an element of air of potential temperature θ is moved adiabatically through some vertical distance through the atmosphere. We can write:

$$R_i = \frac{\frac{g}{T}\frac{\Delta\theta}{\Delta h}}{(\frac{\Delta V}{\Delta h})^2}. \tag{3.7}$$

Using this number, there are three states that can be taken by this element:

- Stable: when $\frac{\Delta\theta}{\Delta h} > 0$, the adiabatically moved air parcel will be colder than the surrounding air and will therefore sink back to a stable po-

sition. In this situation, corresponding to $R_i > 1$, no turbulence is generated (the buoyancy term is greater than the kinetic term). However, if the wind shear is sufficiently large to induce the mixing of the stratified fluid, turbulence can be generated. This is considered for $0 < R_i < 1/4$.

- Neutral: in the idealized case where $\frac{\Delta\theta}{\Delta h} = 0$, there are no vertical thermal transfers and the turbulence is dynamically generated by the wind shear ($R_i = 0$).

- Unstable: this time $\frac{\Delta\theta}{\Delta h} < 0$. Each air parcel will be warmer than the surrounding air and will continue to rise. Not only will turbulence will be induced dynamically but the added thermal motion will create convection ($R_i < 0$).

The Richardson number is a good indicator of the formation of turbulence in the atmosphere. Basic measurements of temperature and wind speed in the atmosphere can provide an indication of whether turbulence may form in a particular layer. Unfortunately, R_i does not quantify the strength of the turbulence.

3.2 Kolmogorov's Statistical Theory of Turbulence

3.2.1 Defining optical turbulence through energy cascade

The theory that enables us to usefully quantify the effect of turbulence was introduced by Kolmogorov (1941). Turbulence can be seen as the break up of a fluid flow into flows of smaller size. This way, the kinetic energy of a system of size L and velocity V is transferred down to smaller scales, which finally become small enough to dissipate the energy in heat and friction. Assuming that the rate of energy production ε_0 is equal to the rate of dissipation, a dimensional analysis yields the following relationship:

$$V \propto \varepsilon_0^{1/3} L^{1/3} \tag{3.8}$$

or expressed in spatial frequency space:

$$V \propto \varepsilon_0^{1/3} \kappa^{-1/3}. \tag{3.9}$$

The kinetic energy field $E(\kappa)$ which is proportional to V^2 can then be integrated over $d\kappa$ and gives:

$$E(\kappa) \propto \kappa^{-5/3} \tag{3.10}$$

The velocity field therefore follows a power law (also called Kolmogorov power spectrum). The energy is generated at a scale L_0, called the outer-scale, and cascades down until it is dissipated at the inner-scale l_0. Kolmogorov's power spectrum therefore only applies between L_0 and l_0 (the sub-inertial range). In the atmosphere, the outer-scale depends on the size of the flow at the origin of the turbulence and is typically between a few tens of meters and a kilometer. Its value is important in astronomy as some large telescope apertures or interferometer baselines may exceed it. The value of the inner-scale, which is less than a centimetre, does not however affect our instruments (see Fig. 3.1). Following the same dimensional analysis technique used to derive the power spectrum, Kolmogorov also introduced the structure function in order to describe the fluctuation of the velocity field as a function distance r. More properly described in Tatarski (1961), the velocity structure function:

$$D_V(r) = \langle (V(x) - V(x + r))^2 \rangle \tag{3.11}$$

Within the sub-inertial range, a power law exists which can be written as:

$$D_V(r) = C_V^2 r^{2/3} \tag{3.12}$$

where the velocity structure constant C_V^2 depends on the kinetic energy of the process. In order to apply this power spectrum to the behavior of light as it travels through turbulence, an assumption was made by Obukhov (1949) and Yaglom (1949). If a passive and conservative parameter is added to the turbulent flow, its concentration will obey the same power law as the turbulence. By passive, we mean that the parameter does not affect the flow. The same parameter is also conservative if it does not change when it moves with the fluid flow. In the case of optical turbulence, the parameter of interest is the refractive index of light. Following Cauchy's formula, we can express the refractive index of air n as a function of atmospheric parameters:

$$n - 1 = \frac{77.6 \times 10^{-6}}{T}(1 + 7.52 \times 10^{-3}\lambda^{-2})(P + 4810\frac{\upsilon}{T}) \tag{3.13}$$
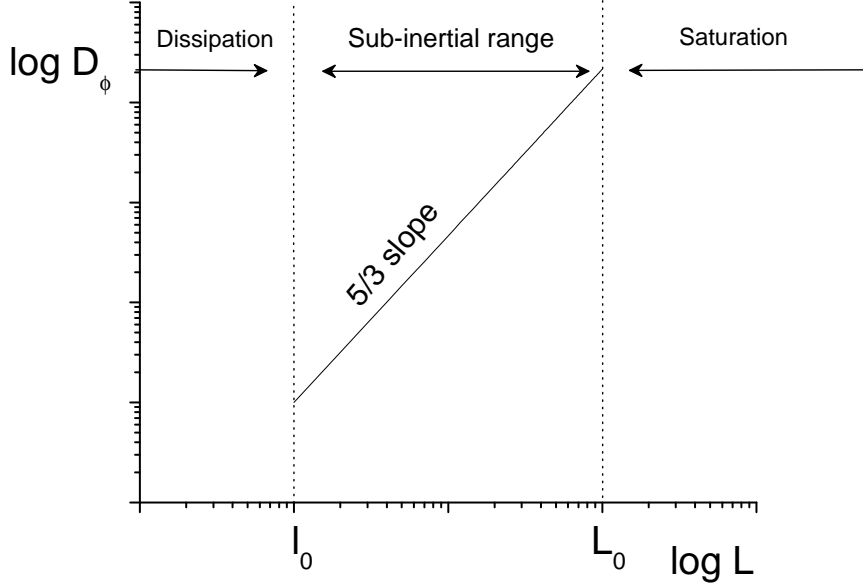
Figure 3.1: Illustration of the range of validity of the Kolmogorov theory.

where λ is the wavelength of light, P the atmospheric pressure in mB, T the temperature (K) and υ the water vapour pressure (mB). Since the humidity fluctuations are usually small, the last term of this equation is neglected. The refractive index at a particular wavelength and altitude therefore only depends on the temperature and pressure. Under the assumption that temperature is indeed a passive and conservative additive, we can express the temperature structure function:

$$D_T = C_T^2 r^{2/3} \tag{3.14}$$

where the temperature fluctuation constant C_T^2 determines the strength of the temperature variations. Since the variation of temperature induces the change of refractive index, we can write the structure function of the refractive index:

$$D_N = C_N^2 r^{2/3}. \tag{3.15}$$

The refractive index fluctuation constant C_N^2 represents the strength of the optical turbulence at a point in space. It can be shown that by differentiating

equation 3.13 and using:

$$C_N = \frac{\partial(n-1)}{\partial T} \tag{3.16}$$

we obtain the relation:

$$C_N^2 = (77.6 \times 10^{-6} \frac{P}{T^2})^2 C_T^2 \tag{3.17}$$

It can be seen here that C_N^2 is not only dependent on the fluctuation of temperature but also on the pressure. This shows that for a given fluctuation of temperature, the effect on the optical path will be smaller as altitude increases. The behavior of C_N^2 in time and its distribution in the atmosphere will be discussed at the end of this chapter.

Similarly to the structure function, one can derive that the three dimensional power spectrum of the refractive index can be expressed as:

$$\Phi_N(\kappa) = 0.033 C_N^2 \kappa^{-11/3} \tag{3.18}$$

3.2.2 Wave propagation through the atmosphere

Now that we have defined the behavior of optical turbulence in the atmosphere we can derive its effect on a light wave travelling through it. As the wavefront $\psi(x) = exp(i\phi(x))$ propagates vertically through a turbulent layer of thickness δh, its phase $\phi(x)$ will be shifted by the refractive index such that:

$$\phi(x) = k \int_h^{h+\delta h} n(x,z)dz \tag{3.19}$$

where $k = \frac{2\pi}{\lambda}$. Normally, the calculation of the phase structure function as it arrives to the telescope after passing through each individual layer of turbulence would be a tremendous task. However, we can use our knowledge of the refractive index function as it is simply quantified at each altitude by the parameter $C_N^2(h)$. Before calculating the phase structure function, we need to introduce its covariance:

$$
\begin{aligned}
B_\phi(r) &= \langle \phi(x)\phi(x+r)\rangle & (3.20)\\
&= k^2 \int_h^{h+\delta h} \int_h^{h+\delta h} dz'dz'' \langle n(x,z')n(x+r,z'')\rangle & (3.21)\\
&= k^2 \int_h^{h+\delta h} dz' \int_{h-z'}^{h+\delta h-z'} d(z''-z')\, B_N(r,z). & (3.22)
\end{aligned}
$$

Assuming that δh is much larger than the correlation scale of turbulence and carrying out the first integral we find:

$$B_\phi(r) = k^2\delta h \int_{-\infty}^{\infty} dz \; B_N(r,z) \tag{3.23}$$

where $z = z'' - z$. It is now convenient to work with the phase structure function and using equation 3.3:

$$
\begin{aligned}
D_\phi(r) &= 2[B_\phi(0) - B_\phi(r)] &(3.24)\\
&= 2k^2\delta h \int_{-\infty}^{\infty} \delta z \; [B_N(0,z) - B_N(r,z)] &(3.25)\\
&= 2k^2\delta h \int_{-\infty}^{\infty} \delta z \; [(B_N(0,0) - B_N(r,z)) &(3.26)\\
&\quad -(B_N(0,0) - B_N(0,z))] &(3.27)\\
&= 2k^2\delta h \int_{-\infty}^{\infty} \delta z \; [D_N(r,z) - D_N(0,z)]. &(3.28)
\end{aligned}
$$

Finally, using equation 3.15 and integrating (the integration is not trivial and will not be elaborated here):

$$D_\phi(r) = 2.914k^2\delta h \; C_N^2 r^{5/3} \tag{3.29}$$

This equation is fundamental as it describes the behaviour of the phase of light as it travels through the atmosphere, by measuring the turbulence intensity C_N^2 of each layer of thickness δh. This function is the starting point of many figures of merit used to describe the effect of the atmosphere of a telescope and its instruments.

3.3 Figures of Merit

3.3.1 The Fried parameter r_0

There are several figures commonly used in astronomy to describe the effect of the atmosphere on the performance of a telescope. The most commonly used is the Fried parameter r_0. Theoretically, in the absence of turbulence, the resolution of a telescope is limited by the size of its mirror and the wavelength of light. If we follow the simplified case of a telescope being a simple circular aperture of size D, the Rayleigh criterion states the minimum

angular distance between two discernable point sources is given by:

$$\varepsilon = 1.22\frac{\lambda}{D} \tag{3.30}$$

If two point objects separated by an angular distance ε are imaged through such an aperture the first maximum of the diffraction pattern of the first object will coincide with the first minimum of the second. ε is therefore the minimum separation for two images to be discernable.

In order to generalize for any aperture function we need to introduce the resolving power R_{tel} which is defined as:

$$R_{tel} = \int df \ B(\kappa)T(\kappa), \tag{3.31}$$

where $B(\kappa) = exp(-1/2D_\phi(\kappa))$ is the wavefront coherence function and $T(\kappa)$ is the transfer function of the telescope. $T(\kappa) = 1$ everywhere within the aperture and zero elsewhere. For a flat wavefront $B(\kappa) = 1$ and again assuming a circular aperture the resolving power of the telescope is:

$$R_{tel} = \int df \ T(\kappa) = \frac{\pi}{4}(\frac{D}{\lambda})^2. \tag{3.32}$$

In this situation the telescope is considered to be diffraction limited. The minimum resolvable size is only related to the size of the telescope and the wavelength. For ground based telescopes, however, the phase covariance function is not equal to one but is dependant on the turbulence structure. Using equation 3.25 and 3.29, we find that:

$$B(r) = exp[-\frac{1}{2}(2.914k^2C_N^2\delta h \ r^{5/3})] \tag{3.33}$$

Integrating this function over the whole atmosphere and introducing the effect of the zenith angle z:

$$B(r) = exp[-\frac{1}{2}(2.914k^2(sec \ z)r^{5/3}\int dhC_N^2(h))] \tag{3.34}$$

We can now use this expression in equation 3.31 to calculate the new resolving power of a telescope under realistic atmospheric conditions. Now

assuming $T(f) = 1$ and substituting $r = \lambda f$, the resolving power becomes:

$$
\begin{align}
R_{tel} &= \int df \, exp[-\frac{1}{2}(2.914k^2(sec\ z)(\lambda f)^{5/3}\int dh C_N^2(h))] \quad &(3.35) \\
&= \frac{\pi}{4}(\frac{[0.423k^2(sec\ z)\int dh C_N^2(h)]^{-3/5}}{\lambda})^2 \quad &(3.36) \\
&= \frac{\pi}{4}(\frac{r_0}{\lambda})^2. \quad &(3.37)
\end{align}
$$

The last substitution which introduces the Fried parameter r_0 was made by analogy with the theoretical power of resolution of a telescope. This time the size of the mirror D is replaced by:

$$
r_0 = [0.423k^2(sec\ z)\int dh\ C_N^2(h)]^{-3/5}. \quad (3.38)
$$

This parameter can be interpreted as being the size of a telescope that would be diffraction limited in an atmosphere of integrated turbulence $\int dh\ C_N^2(h)$. Coincidentally, it can be shown that over an aperture of size r_0 the mean-square phase variance is equal to 1 rad^2. Unfortunately, even the best known sites have an average Fried parameter that does not exceed 30 cm in the visible. For telescopes larger than this size, the resolution is said to be turbulence or "seeing" limited and an increase of mirror size does not affect the resolution. The seeing quality of a site is therefore defined by the average value of r_0, although at any given site this value can vary greatly as a function of time or even season.

Another figure commonly used to define the seeing is the full width half maximum (FWHM) of a point source image. Expressed in arc seconds, the FWHM is a more intuitive unit used by the community to describe the resolution capability of an observatory. The relationship between the seeing FWHM and r_0 is rather straight forward:

$$
\varepsilon_{FWHM} = 0.98\frac{\lambda}{r_0} \quad (3.39)
$$

In diffraction limit conditions the FWHM is given by the same expression using D instead of r_0. In this thesis we will express the seeing using the FWHM. It is also important to note the wavelength dependence of the seeing ($\varepsilon_{FWHM} \propto \lambda^{-1/5}$); at larger wavelengths the effect of the atmosphere decreases. Even for large observatories this relationship means that the tele-

scope becomes diffraction limited in the mid-infrared. Fig 3.2 summarizes the wavelength dependence of the resolution of a telescope in both turbulence and diffraction limit conditions. We can see that when the turbulence dominates, the resolution increases with wavelength. However, when the point of diffraction limit is reached then the resolution decreases with increasing wavelength.
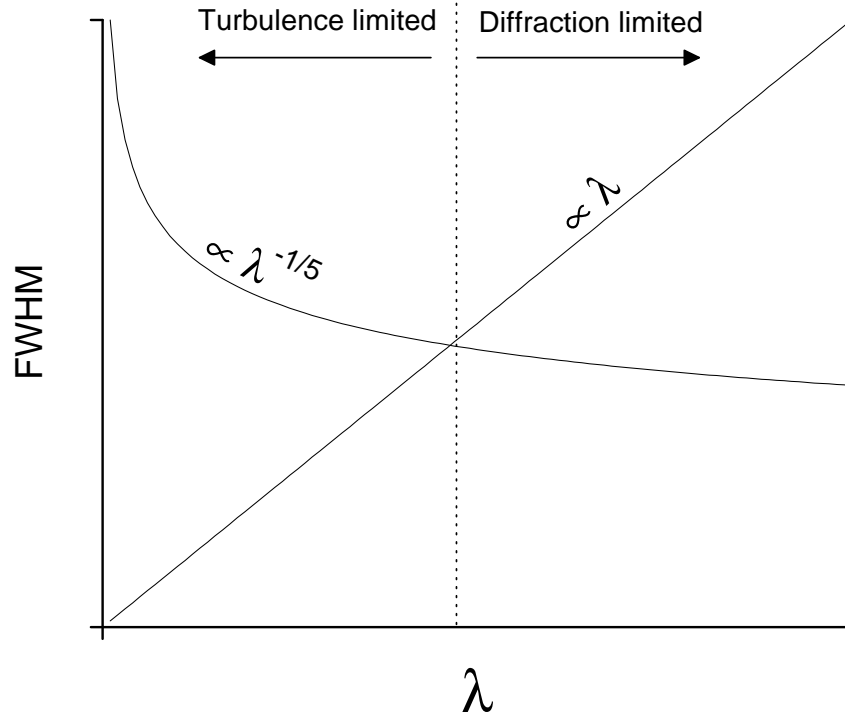
Figure 3.2: Wavelength dependance of a telescope resolution.

For a given mirror size the resolution limit can only be lowered by going to a site where the integrated turbulence will be lower. The seeing is therefore one of the most important parameters to be measured in site testing.

3.3.2   The isoplanatic angle θ_0

The aberration of the wavefront created by the atmospheric turbulence can be partially compensated with adaptive optics (AO). The method uses a

wavefront sensor that determines the shape of the wavefront. This shape is then fed into a deformable mirror that will flatten out the wavefront. One of the limitations of this technique is that the wavefront sensing is done in a particular line of sight. For deviations from this line the turbulence structure changes and the correction no longer applies. This effect is called anisoplanatism. We have seen earlier that r_0 is the diameter within which the mean phase variance is 1 rad^2. AO correction will therefore be valid in a field size where the phase is constant. In other words, it is necessary to determine the maximum angular separation between two stars that an AO system will correct to the same degree.

This angular separation θ is related to their separation at the pupil r such that $r = \theta h sec\ z$, where h is the height and z the zenith angle. We use this expression and integrate equation 3.29 to calculate the phase variance:

$$\sigma_\theta^2 \ =\ 2.914 k^2 (sec\ z) \int dh\ C_N^2(h) \theta h\ (sec\ z)^{5/3} \tag{3.40}$$

$$=\ 2.914 k^2\ (sec\ z)^{8/3} \theta^{5/3} \int dh\ C_N^2(h) h^{5/3} \tag{3.41}$$

$$=\ (\frac{\theta}{\theta_0})^{5/3}. \tag{3.42}$$

By analogy with the definition of r_0 we have introduced a new quantity, the isoplanatic angle, which is the maximum angular separation in the sky where the turbulence structure is constant and can be compensated with AO. In the expression:

$$\theta_0 = [2.914 k^2\ (sec\ z)^{8/3} \int dh\ C_N^2(h)\ h^{5/3}]^{-3/5} \tag{3.43}$$

we see the dependence of the isoplanatic angle with the vertical distribution of the turbulence. As illustrated in Fig 3.3, the isoplanatic angle is much wider if the majority of the turbulence is located near the ground. This characteristic is very important to this thesis as we will show that in Antarctica the high altitude turbulence is very small.

The isoplanatic angle is often expressed as a function of r_0 and the effective turbulence height, $\langle H \rangle$;

$$\langle H \rangle = (\frac{\int dh\ C_N^2(h) h^{5/3}}{\int dh\ C_N^2(h)})^{3/5}. \tag{3.44}$$
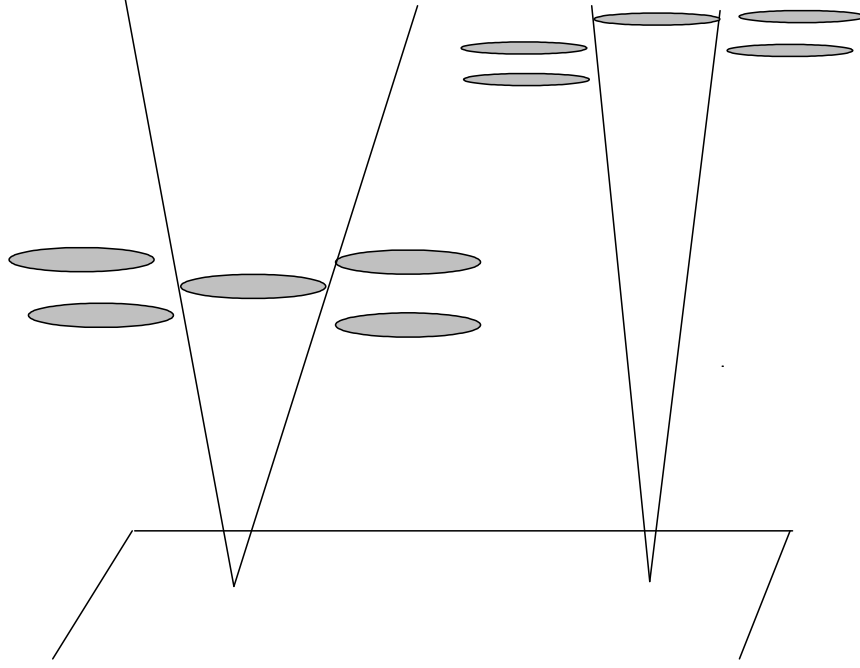
Figure 3.3: The altitude of the main turbulence layer strongly affects the angle of correction of AO systems. Lower altitude turbulence gives wider angles.

This new quantity can be interpreted as the turbulence-weighted centre of mass of the atmosphere. Using $\langle H \rangle$ we can more easily relate the isoplanatic angle to the seeing and its vertical distribution and write:

$$\theta_0 = 0.314 \ (cos \ z) \frac{r_0}{\langle H \rangle}. \tag{3.45}$$

3.3.3   The coherence time τ_0

Now that we have defined the horizontal and vertical structure of atmospheric turbulence, it is critical to define its temporal structure. Indeed, the lifetime of a particular turbulence structure will determine the speed of the fluctuations of the wavefront. The quantity that defines this speed is called the coherence time. To derive the coherence time we must use the Taylor hypothesis of frozen turbulence. This hypothesis states that the turbulence

cells do not evolve in short time scales but are simply carried across the field by the wind velocity v (see Fig 3.4). In the simplified situation of a single turbulence layer this would mean that the coherence time τ_0 is given by:

$$\tau_0 = r_0/v. \tag{3.46}$$

For a realistic atmosphere τ_0 can be derived similarly to the isoplanatic angle and expressed as function of the effective wind speed $\langle V \rangle$ where:

$$\tau_0 = 0.314 \ (cos \ z)\frac{r_0}{\langle V \rangle} \tag{3.47}$$

and

$$\langle V \rangle = (\frac{\int dh \ C_N^2(h)v^{5/3}}{\int dh \ C_N^2(h)})^{3/5}. \tag{3.48}$$

The basic significance of τ_0 is that for integration times $t > \tau_0$, the image of a star will be blurred over the seeing angle ε_{FWHM}. For smaller integration times, the image will be composed of speckles spread over the seeing angle but of individual size as low as the diffraction limit from which some spatial information can be retrieved (speckle astronomy). The coherence time is also crucial in adaptive optics and interferometry. For these two applications, the Greenwood frequency $f_g = 0.135/\tau_0$ is used to define the bandwidth of the control loop. In the case of interferometry, it is the fringe pattern which needs to be tracked and in AO, it is the phase. A good site must have a large coherence time in order to lower the demand on the control system. A site with a low integrated wind speed is therefore preferred for future observatories.

3.3.4   The index of scintillation σ_I^2

Finally a mention must be made of the index of scintillation. Scintillation, which is defined as the observed temporal variance of a star intensity, is a problem in several areas of astronomy requiring high precision photometry such as astro-seismology and exoplanet searches. Scintillation, unlike seeing, is not only caused by the variation of phase in the atmosphere but also by the interference of refracted rays. This phenomenon, which is highly chromatic, is mainly caused by the turbulence contribution of the higher parts of the atmosphere. Although it only applies to very small apertures ($< 3 \ cm$), the
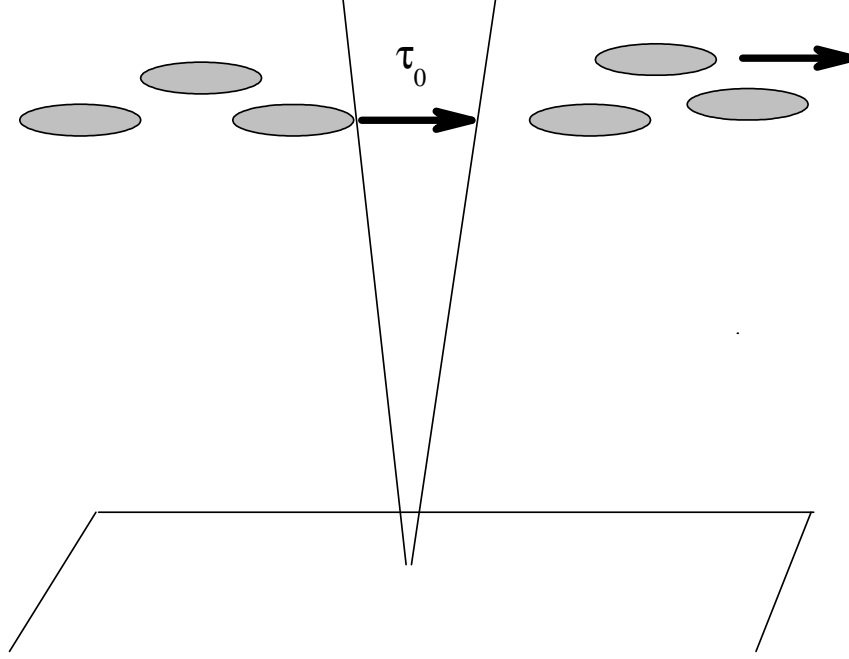
Figure 3.4: Assuming "frozen" turbulence, the wind carries a turbulence cell across r_0 in a time equal to τ_0.

index of scintillation is often expressed as (Roddier (1981)):

$$\sigma_I^2 = 2.24k^{7/6} \ (sec \ z)^{11/6} \int dh \ C_N^2(h) \ h^{5/6} \qquad (3.49)$$

and is of the order of 10% at a good site. This expression shows that similarly to the isoplanatic angle, the index of scintillation is dependent on the vertical distribution of the turbulence profile. Also, one must note the even larger dependance on the zenith angle. For larger apertures the vertical dependence also increases as the low altitude and higher frequency contribution is filtered out by the aperture. The new relation becomes:

$$\sigma_I^2 \propto D^{-7/3} \ (sec \ z)^3 \int dh \ C_N^2(h) \ h^2 \qquad (3.50)$$

where D is the telescope aperture diameter.

3.4 Turbulence Distribution

Now that we have explained the process of formation of optical turbulence and its formulation, it is important to examine its distribution in the atmosphere. C_N^2 can take a wide range of values from $10^{-14} m^{-2/3}$ near the ground to $10^{-19} m^{-2/3}$ at the top of the troposphere. The fast drop can be explained by the P^2 dependance of optical turbulence. Atmospheric pressure falls exponentially with height. At sea level the pressure is around 1000 millibars but it is only 10 millibars at an altitude of 30 km. Beyond this altitude the effect of turbulence is negligible. Beside the influence of pressure, the thermal activity and wind shear determine the turbulence strength of a particular part of the atmosphere. Typically the atmosphere is divided up into several parts defined by different behavior of the turbulence.

1. **Dome Turbulence:** The first source of optical turbulence is the telescope itself. Often referred to as "Dome seeing" temperature differences between the mirror and structure of the telescope and the ambient air can contribute to a non negligible source of resolution loss. The same thing can also be said about structures surrounding the telescope dome. For this reason additional buildings are usually built down-wind from the telescope. Caused by the diurnal cycles, the night telescope heat exchange can be minimized by careful ventilation. At modern sites, the dome is refrigerated during the day to match the nighttime temperature conditions.

2. **Surface layer:** Producing the most turbulence per unit length, the surface layer extends up a few tens of metres. During the day, the Sun irradiates the ground creating a convection layer a few hundred meters thick. This layer is obviously extremely turbulent. At night, the convection stops and the surface layer decreases. Turbulence is then caused by the cooling of the ground in a manner similar to Dome seeing. This process is usually increased by topographic and climatic conditions. In this region C_N^2 can take values ranging from $10^{-14} m^{-2/3}$ to $10^{-16} m^{-2/3}$.

3. **Boundary layer:** Sometime considered as an extension of the surface layer, the boundary layer (also called "planetary boundary layer") can extend from a few hundred metres up to 2 km. Turbulence in the boundary layer is influenced by the large scale conditions of a site but also by the ground heat flux. It is usually composed of two peaks of turbulence, the first at the top of the temperature inversion layer and a second at the boundary with the free atmosphere laminar flow. In high island sites the boundary layer is located below the observatory. These sites therefore have very low seeing contributions from this part of the atmosphere. Depending on the nature of the site, the boundary layer can be differentiated from the surface layer and the turbulence takes values between $10^{-15}m^{-2/3}$ and $10^{-17}m^{-2/3}$.

4. **Free atmosphere:** The free atmosphere corresponds to the part of the atmosphere where the thermal interaction with the ground becomes negligible. It therefore begins just above the boundary layer. Turbulence drops with altitude and is neglected above 25 km where it has become as low as $10^{-19}m^{-2/3}$. In the free atmosphere, thin layers of turbulence can be formed by wind shear. At temperate sites the jet stream is one of the major cause of high altitude turbulence. Formed by the mix of cold air coming from the poles and the warm air coming from the equator, the jet stream can give peaks of turbulence of the order of $10^{-15}m^{-2/3}$.

High spatial resolution profiles have shown that turbulence is composed of very thin peaks whose intensity is several orders of magnitude higher than the background. In the boundary layer these peaks can be up to 200 m thick. In the free atmosphere, however, they never exceed a few tens of metres and are usually found in pairs. This characteristic has been explained by Coulman et al. (1995) and revisited by Vernin (2002). When two laminar flows meet, air mixes in a boundary of a few hundred of metres in thickness. Within this boundary, dynamical turbulence is intense (high wind shear). However, in the middle of this layer the temperature equilibrates rapidly and no optical turbulence is formed. At the lower and upper edge of this boundary the thermal gradient is large enough and, coupled with the wind shear, creates peaks of turbulence.

3.5   Beyond Kolmogorov

While Kolmogorov theory is commonly accepted and used across the literature, we must stress the limitation of this theory. Indeed, Kolmogorov's power law is only applicable to scales smaller than the outer-scale L_0. In this theory, propagation of light follows negative power laws whose integrals diverge at the boundary L_0. An alternative model has therefore been proposed by Von Karman (conveniently expounded in Lutomirski and Yura (1971)). In this model the Kolmogorov refractive index power spectrum given in equation 3.18 is replaced by:

$$\Phi_N(\kappa) = 0.033 C_N^2 (\kappa^2 + \frac{1}{L_0^2})^{-11/3}. \qquad (3.51)$$

This model gives a more accurate representation of turbulence in the low frequency range by including the effect of the outer-scale itself (see Fig 3.5). Since the outer-scale can be as low as a few metres, its effects are crucial to the development of large telescopes and interferometers. For a given r_0, the size of L_0 will influence the scale at which the turbulence energy saturates. Kolmogorov theory essentially assumes that $L_0 = \infty$ and therefore overestimates the effect of turbulence. As site testing targets larger and larger telescopes, measuring the value of the outer-scale becomes more important. Since L_0 is a physical quantity which takes different values through the atmosphere, it is convenient to define an integrated outer-scale (Borgnino (1990)):

$$\mathcal{L}^{-1/3} = \frac{\int_0^\infty dh\, L_0(h)^{-1/3} C_N^2(h)}{\int_0^\infty dh\, C_N^2(h)}. \qquad (3.52)$$

As an example, the equation for the variance of the angle of arrival can be adapted to the Von Karman model and uses the expression of $\mathcal{L}$:

$$\sigma^2 = 0.0114 \pi \lambda^2 r_0^{-5/3} \mathcal{L}^{-1/3}. \qquad (3.53)$$

From this expression it can be seen that the outer-scale also influences seeing measurements. However, due to the difficulty in measuring $\mathcal{L}$ and in order to obtain data comparable to other studies, the work presented in this thesis will use the less accurate Kolmogorov power law and neglects the effect of the outer-scale. A complete quantitative study of the influence of the outer-scale can be found in Ziad (1993). In their work, the level of error introduced

by the use of the Kolmogorov theory is evaluated.
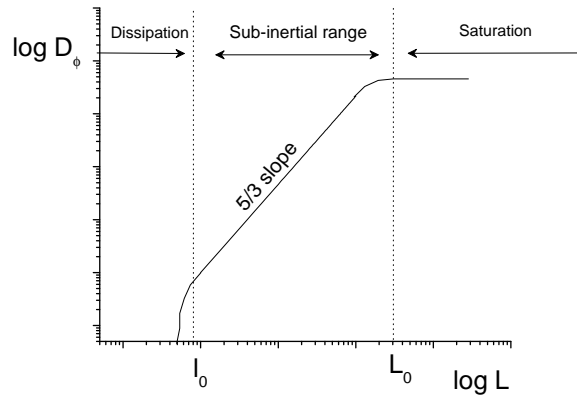
Figure 3.5: Illustration of the Von Karman spectrum. Unlike Kolmogorov turbulence, the Von Karman model includes the effect of the outer-scale length.

Chapter 4

Turbulence Profiling : a Review

The aim of this chapter is to present and compare several methods used to measure the optical turbulence profile and determine the figures of merit used to assess the quality of a site. The list of instruments we compare is by no mean exhaustive. We summarize the characteristics of several optical techniques (DIMM, GSM, SCIDAR, MASS and SLODAR), an acoustic instrument (SODAR) and an *in situ* method. We have excluded instruments such as LIDARs (LIght Detection And Ranging), which have the potential to make the measurements but which have not yet been properly exploited in astronomy. A summary of each instrument is presented in table 4.1.

4.1 Optical Seeing Monitors

4.1.1 DIMM

Probably the most commonly used instrument for measuring the integrated seeing over the entire atmosphere is the Differential Image Motion Monitor (DIMM). While not a true profiler, the DIMM is one the only instrument that measures the contribution of all the turbulence between its aperture and the star it is pointing to, including dome turbulence. Although its origin is often attributed to Stock and Keller (1960), it was actually introduced by Hosfeld (1954). The idea behind the DIMM is that the seeing can be measured using the change in the angle of arrival of light coming from a star.

These two quantities are related by the following equation (Fried (1975)):

$$\sigma_m^2 = (3.44/\pi^2)\lambda^2 D^{-1/3} r_0^{-5/3} \tag{4.1}$$

where σ_m^2 is the variance of the angle of arrival, D the diameter of the aperture, λ the wavelength of light and r_0 the Fried parameter. In principle it is therefore possible to determine the integrated turbulence by measuring the motion of a star using any telescope aperture. However, this motion will also be affected by shaking of the telescopes due to wind and ground vibration, as well as by tracking errors, all of which are independent of the motions due to turbulence. The DIMM avoids this problem by measuring the differential motion of the starlight using two or more sub-apertures of the telescope. Any vibration of the telescope will be equally felt by the sub-apertures and will therefore not appear in the measurement of the differential motion. The DIMM theory is taken from Martin (1987) and Sarazin and Roddier (1990):

For an incoming wavefront with phase function $\phi(x, y)$, the angle of arrival (which is perpendicular to this wavefront at the point of observation) can be written as:

$$\alpha = -\frac{\lambda}{2\pi}\frac{\partial \phi(x, y)}{\partial x} \tag{4.2}$$

$$\beta = -\frac{\lambda}{2\pi}\frac{\partial \phi(x, y)}{\partial y} \tag{4.3}$$

Where α and β are the x and y components of the angle of arrival. The expression of the covariance of the angle of arrival B_α can be written as:

$$B_\alpha(x_0, y_0) = <\alpha(x, y)\alpha(x + x_0, y + y_0)> \tag{4.4}$$

This expression can be related to the phase covariance C_ϕ using the properties of the second derivative of a function (Beckmann (1967)):

$$B_\alpha(x_0, y_0) = -\frac{\lambda^2}{4\pi^2}\frac{\partial^2}{\partial x_0^2}B_\phi(x_0, y_0) \tag{4.5}$$

Introducing the phase structure function

$$D_\phi(x_0, y_0) = 2[B_\phi(0, 0) - B_\phi(x_0, y_0)] \tag{4.6}$$

and substituting it into equation 4.5, leads to:

$$B_\alpha(x_0, y_0) = \frac{\lambda^2}{8\pi^2} \frac{\partial^2}{\partial x_0^2} D_\phi(x_0, y_0) \tag{4.7}$$

Assuming a Kolmogorov turbulence, the phase structure function obeys the following power law:

$$D_\phi(x_0, y_0) = 6.88(\frac{\sqrt{x_0^2 + y_0^2}}{r_0})^{5/3} \tag{4.8}$$

Where r_0 is the Fried parameter. Substituting equation 4.8 into 4.7 and having $(x_0 = d, y_0 = 0)$ for longitudinal covariance along the direction of separation d between two points or $(x_0 = 0, y_0 = d)$ for the transverse covariance in the direction perpendicular to the separation leads to:

$$B_\alpha(d, 0) = 0.097(\frac{\lambda}{r_0})^{5/3}(\frac{\lambda}{d})^{1/3} \tag{4.9}$$

$$B_\alpha(0, d) = 0.145(\frac{\lambda}{r_0})^{5/3}(\frac{\lambda}{d})^{1/3} \tag{4.10}$$

The variance $B_\alpha(0, 0)$, however, cannot be calculated using the same technique as the above expressions diverge at the origin and are limited by aperture averaging. Instead, we use the expression derived by Fried (1965), Fried (1975) and Tatarski (1961) compensated for one dimensional motion, which is summarised in Roddier (1981):

$$B_\alpha(0, 0) = 0.179(\frac{\lambda}{r_0})^{5/3}(\frac{\lambda}{D})^{1/3} \tag{4.11}$$

where D is the aperture size measuring the variance. This expression does not affect the calculation for the covariance for $d > 2D$. We can now express the variance of differential motion between two points separated by a distance d:

$$\sigma_l^2 = 2[B_\alpha(0, 0) - B_\alpha(d, 0)] \tag{4.12}$$

$$\sigma_t^2 = 2[B_\alpha(0, 0) - B_\alpha(0, d)] \tag{4.13}$$

respectively the variance along the direction of separation d (longitudinal) and in the direction perpendicular to it (transverse). Substituting equa-

tion 4.9 and 4.11 into 4.12 and 4.10 and 4.11 into 4.13 yields:

$$\sigma_l^2 = 2\lambda^2 r_0^{-5/3}[0.179D^{-1/3} - 0.097d^{-1/3})] \tag{4.14}$$

$$\sigma_t^2 = 2\lambda^2 r_0^{-5/3}[0.179D^{-1/3} - 0.145d^{-1/3})] \tag{4.15}$$

The two variances allow one to calculate two estimates of r_0 by measuring their values coming from two DIMM sub-apertures of size D and separated by a distance $d > 2D$.

Simple implementations of this instrument (e.g. Vernin and Munoz-Tunon (1995)) consist of a commercial 8" to 12" Cassegrain telescope and a CCD camera with a fast read-out time, making the DIMM a cheap and technologically accessible method to measure the seeing. The speed of the CCD is important because a large statistical sample of images is necessary for the calculation of the variances σ_l^2 and σ_t^2. Also, a short exposure is required to avoid temporal blurring of the image. Typical exposure times of 5 to 20 ms are used and are usually extrapolated to a theoretical 0 ms seeing using interlaced series of two different exposure times (Sarazin (1997)). The main difference between currently existing DIMMs is the method used to separate the beam in two or more sub-apertures. The simplest technique consists in using a two-aperture mask at the entrance of the telescope pupil (e.g. Vernin and Munoz-Tunon (1995)). One of the apertures is fitted with a wedge that will shift its image on the CCD by a value proportional to the angle of the wedge. The advantage of this technique, beside its simplicity, is that the mask can be easily replaced by another aimed at measuring other parameters (see next paragraph). Other methods usually re-image the pupil plane and split the aperture into sub-apertures using a mask and a beam splitter (Sarazin and Roddier (1990)) or a microlens array (Dopita et al. (1996)). A variation of this technique consists of simply using a mask and observing the separated images slightly outside the focal plane (Bally et al. (1996)); the key advantage of this technique is that it can be used on any small telescope without the addition of extra pieces of optics. For the last two techniques mentioned, more than two sub-apertures can be used. For n apertures, there are $n(n-1)$ baselines that can be used to determine the seeing, thereby strongly improving the statistics of the measurements. Recommendations on the measurement and treatment of experimental errors can be found in Tokovinin (2002) and Sarazin and Roddier (1990).

The practical aspect of the DIMM and the agreement of its seeing measurements with the FWHM of images taken with large telescopes has made this instrument widely popular in the astronomical community. DIMMs are now a permanent feature of some of the major observatories such as Cerro Paranal or Mauna Kea. However, it is less commonly known that the DIMM can also be used to determine the isoplanatic angle. By doing so, the DIMM becomes a first order turbulence profiler. The turbulence weighted mean altitude $\langle H \rangle$, which can be thought of as the turbulence centre of mass, is given by:

$$\langle H \rangle^{-3/5} = 3.23\theta/r_0 \qquad (4.16)$$

where θ is the isoplanatic angle. The DIMM can indirectly measure the isoplanatic angle by measuring the scintillation index σ_I^2. It has been found by Loos and Hogge (1979) and further investigated by Krause-Polstorff et al. (1993) that for a 10 cm aperture with a central obstruction of 4 cm there is a direct relation between the isoplanatic angle and the scintillation index:

$$\theta_0^{-5/3} = K\sigma_I^2 \qquad (4.17)$$

where K is a wavelength dependent constant. It is therefore easy to construct a DIMM mask with two small apertures for seeing measurement and a third aperture fitting the above requirement to determine the index of scintillation and the isoplanatic angle. Such measurements were taken in alternation by Aristidi et al. (2004) by changing the mask at the entrance pupil.

Overall, the DIMM is a practical and accessible instrument that is capable of measuring several of the parameters interesting to astronomy. While it cannot provide a detailed structure of the turbulence through the atmosphere, it is one of the few instruments that measures the entire turbulence along the line of sight.

4.1.2   GSM

As described above, the advantage of the DIMM is its ability to measure some atmospheric properties that would be deduced from the C_N^2 profile. The GSM (Generalized Seeing Monitor) expands on this idea to measure all the turbulence parameters essential to astronomy. In its first implementation (Martin et al. (1994)), then called Grating Scale Monitor, the GSM was

capable of measuring r_0, the outer scale $\mathcal{L}$ and the coherence time τ_0. It was then updated to its current form (Ziad et al. (2000)) to measure the isoplanatic angle via scintillation measurements as described in the previous section.

The first strength of the GSM over the DIMM comes from the technique used to measure the angle of arrival. Instead of finding the star centre of mass on a CCD detector, a method limited to the detector's speed, the GSM uses a technique used in interferometry to determine the phase of an incoming wavefront (Creath (1988)). At the focal plane of the GSM is placed a Ronchi grating over which the star image is scanned over at 200 Hz. Four times per grating period the flux is measured by a photomultiplier. In the absence of turbulence, the flux should describe a perfect sinusoidal function related to the phase Φ by the expression:

$$\Phi = \frac{1}{2\pi}tan^{-1}(\frac{D-B}{A-C})$$ (4.18)

where A, B, C and D are successive measurements of the flux within a grating period, p. The angle of arrival is finally given by $\alpha = p\Phi$. The high speed of this technique along with the sturdy build of the instrument makes remaining vibrations of the telescope negligible or removable by fitting.
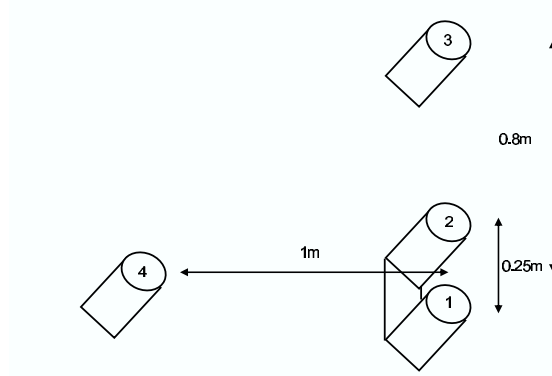
Figure 4.1: Arrangement of the GSM apertures.

The second strength of the GSM, which makes the measurement of $\mathcal{L}$ and τ_0 possible, is the addition of two extra sub-apertures. Each aperture consists of a 10 cm telescope. The first two telescopes use the same mount and are placed 25 cm apart. They are used similarly to a DIMM to measure r_0 differentially. The two other telescopes are placed perpendicularly at a

distance of about 1 m from the first pair (see Fig 4.1). The different base-lines formed by this arrangement measure the turbulence power spectrum at spatial frequencies (f). It is in the determination of $\mathcal{L}$ that these base-lines are important(Agabi et al. (1995)). Being model dependent, the GSM calculates the value of the outer scale using the more accurate Von-Karman spectrum:

$$W_\phi(f) = 0.0229 r_0^{-5/3} (f^2 + \frac{1}{\mathcal{L}_{VK}^2})^{-11/6} \qquad (4.19)$$

It is important to note that the estimation of ($\mathcal{L}$), using another model can be easily accessed through a simple calculation not involving the raw GSM measurements. For example, the value of $\mathcal{L}_{GT}$ issued from the Greenwood-Tarazano model is found from the Von-Karman $\mathcal{L}_{VK}$ (Ziad et al. (2000)):

$$\mathcal{L}_{GT} = -5.544 + 1.588\mathcal{L}_{VK} + 0.0037\mathcal{L}_{VK}^2 \qquad (4.20)$$

For the measurement of the wavefront speed, the GSM looks at the temporal cross correlation of the angle of arrival between two telescopes i and j separated by a distance d:

$$C_{ij}(d, \tau) = \langle \alpha_i(r, t)\alpha(r + d, t + \tau) \rangle \qquad (4.21)$$

where τ is the time taken by the turbulence moving at a speed $\langle v \rangle$ to traverse the distance d. This correlation function peaks at time τ and from the corresponding $\langle v \rangle$ is calculated τ_0.

The GSM is a definite improvement over the DIMM as it measures the ensemble of the atmospheric characteristics necessary for site characteriza-tion. However, the GSM is more complex, less transportable and requires a more stable mount than the DIMM since it relies on single aperture measure-ments. Unlike the DIMM, which can be conveniently installed permanently at an observatory, the GSM requirements make it limited to short campaign at sites where personnel can be present. So far the GSM has characterized several sites such as the Observatoire de la Cote D'Azur (Agabi et al. (1995), La Silla (Tokovinin et al. (1998)), Cerro Paranal (Martin et al. (2000)), Mt. Maidanak (Kornilov and Tokovinin (2001)) and Oukaimeden (Ziad et al. (2001)).

4.2 SCIDAR

The optical sensors detailed above are perfectly suited to the determination of the atmospheric parameters important to site testing and AO performance calculations. However, more elaborate AO system such as Multi Conjugate Adaptive Optics (MCAO) or Wide Field Adaptive Optics (WFAO), which rely on the correction of specific layers of the atmosphere, require a more specific knowledge of the turbulence distribution.

One of the most commonly used turbulence profilers using an optical method is the SCIDAR (Scintillation Detection And Ranging). Its concept, first introduced by Vernin and Roddier (1973) and Rocca et al. (1974), is based on the measurement of the spatial autocorrelation of the speckle or scintillation patterns formed by a star in the pupil plane. The technique uses a binary star of angular separation ρ. The path difference of the light coming from the two stars induced by the atmospheric turbulence will cause the two scintillation patterns to be shifted by a distance d. If we consider the case of a single turbulence layer at altitude h, it is easy to see that the scintillation shift is simply $d = \rho h$. d is found by computing the average spatial autocorrelation function of short exposure images:

$$C^{**}(r) = \int_0^\infty C_N^2(h)\{aC(r,h) + b[C(r-d,h) + C(r+d,h)]\}dh \quad (4.22)$$

where the factors a and b are given by:

$$a = \frac{1+\alpha^2}{(1+\alpha)^2}, b = \frac{\alpha}{(1+\alpha)^2}, \alpha = 10^{-0.4\Delta m} \quad (4.23)$$

and Δm is the magnitude difference between the two stars. This function contains a central peak and two smaller first order peaks. The intensity of the turbulence layer is related to the strength of these peak while d is simply given by the distance between the central and lateral peaks. For a real atmosphere, containing multiple peaks, the C_N^2 profile is obtained by matrix inversion:

$$A(r) = C_N^2 \times T(r,h) \quad (4.24)$$

where A(r) is the one dimensional slice through the autocorrelation function and T(r,h) a 2D matrix of the system geometry. A more thorough description of the theory and image processing can be found in Vernin and Azouit

(1983) and Vernin and Azouit (1983b). The major drawback found with the first implementation of the SCIDAR was its minimum range. The SCIDAR relies on the measurement of scintillation. As we know, the scintillation is proportional to $h^{5/6}$, so the instrument is insensitive to perturbation created near the ground. It restricted the measurement to a minimum height of a few hundred of meters up to 2 km, depending on the star brightness. In order to correct this weakness, a second implementation called "generalized SCIDAR" was introduced a few years later (Fuchs et al. (1998) and Avila et al. (2001)). The idea, which was verified experimentally, was that if the instrument is conjugated to a specific altitude, it will be insensitive to the scintillation created at this altitude but will still be sensitive to all the other layers. This is also true if the conjugated altitude is negative which means that if the SCIDAR is, let's say, blind to the first kilometer, this problem can be fixed by conjugating its detector to an altitude of h_c = -1 km. It will therefore measure all the turbulence from the ground including the dome seeing. This improvement is very valuable scientifically and does not affect the technology of the SCIDAR. The theory of operation is not complicated either, as the autocorrelation function needs to be simply calculated for a new altitude $H = h - h_c$. A second major improvement introduced by Avila
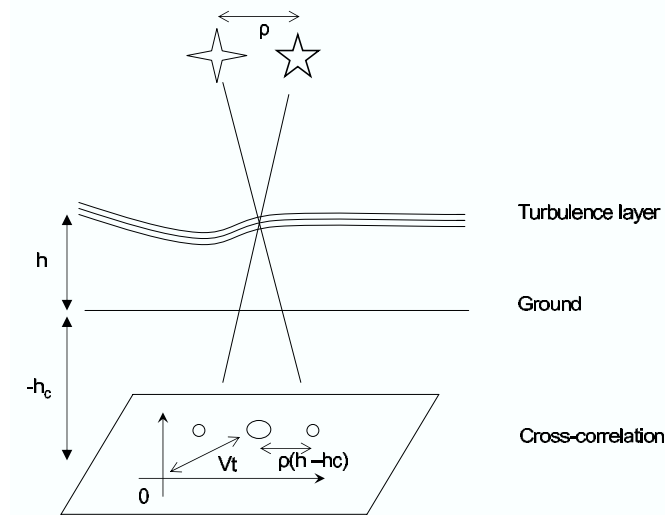
Figure 4.2: In order to calculate the turbulence and wind speed profile, the Generalised SCIDAR looks at the cross-correlation and autocorrelation functions of the scintillation pattern on a CCD conjugated to a negative altitude.

et al. (1997) and developed by Klueckers et al. (1998) was the measurement of the wavefront speed profile. The wind speed profile is not only important to the calculation of the coherence time of the atmosphere. It is also a crucial quantity in the verification of atmospheric turbulence models (Masciadri et al. (2002)). This is achieved by the SCIDAR by looking at the temporal cross-correlation of images separated by a time Δt. Similarly to the auto-correlation function, the cross-correlation function will have the same peaks giving the turbulence intensity and altitude but this time, the central peak will be shifted from the origin by a distance $r = V\Delta t$ (see Fig 4.2).

In its original design, the SCIDAR was already capable of measuring almost real-time C_N^2 profiles by using between 1000 and 2000 exposures of 1 to 2 ms depending on the star magnitude. The excellent temporal resolution even exceeds that of the DIMM and is very important for studies of the structure of turbulent cells (Masciadri et al. (2002) and Kern et al. (2000)). With the inclusion of the wind speed measurements, the temporal resolution is decreased since the cross-correlations are calculated over a time of 20 to 40 ms and this gives out a set of profiles around every minute. The vertical resolution of the SCIDAR is, however, not as sharp as some other techniques described in this chapter. The vertical resolution is given by (Vernin and Azouit (1983)):

$$\Delta H = \frac{0.5}{\rho}\sqrt{\lambda(h - h_c)} \tag{4.25}$$

which is typically of the order of a few hundred meters at the ground. This resolution is, however, sufficient for most applications in astronomy. The SCIDAR has been used in many campaigns around several sites such as: La Palma (Vernin and Munoz-Tunon (1992) and Vernin and Munoz-Tunon (1994)), Mauna Kea (Racine and Ellerbroek (1995)), San Petro Mártir (Avila et al. (1998)), Cerro Pachon (Avila et al. (2000)), Cerro Paranal (Masciadri et al. (2002)) and Pic du Midi (Prieur et al. (2001)). While, the SCIDAR is an ideal instrument for the turbulence characterization at an already existing observatory, it is impractical for the testing of remote sites where no facility is already in place. This restriction is caused by the minimum size of the telescope used by the SCIDAR which has to be larger than 1 m in typical conditions in order to encompass the first Fresnel zone necessary to the measurements. Such a telescope size is clearly too large for

the testing of new sites and the SCIDAR may only become useful to carry out a more thorough study of the atmospheric turbulence once an observatory is operational and when a complex AO system is being considered. It also means that no long-term monitoring of a site can be done with the SCIDAR unless a large telescope is dedicated to this purpose.

4.3 MASS

The idea of using optical methods to measure the atmospheric turbulence profile, as the SCIDAR does, is compelling to astronomers. However, the complexity and practicability of this instrument are restrictive. For this reason, another method capable of working on small and transportable telescopes was proposed by Tokovinin (1998). Using the same fundamental theory used by the "scintillometer" (Ochs et al. (1976)), the Multi Aperture Scintillation Sensor (MASS) relies on the measurement of the scintillation index:

$$\sigma_I^2 = \int_0^\infty C_N^2(h)W(h)dh \qquad (4.26)$$

where the weighting function W is dependent on the height and on the telescope aperture function. It was also found that by measuring the differential scintillation between two annular apertures given by:

$$\sigma_d^2 = \langle (ln\frac{I_1}{I_2})^2 \rangle - \langle ln\frac{I_1}{I_2} \rangle^2 \rangle \qquad (4.27)$$

produces another weighting function also dependent on height. A detailed analysis can be found in Tokovinin (2002b).

The MASS consists of 4 concentric circular apertures of 2, 3.7, 7 and 13 cm. The light coming from each aperture is reflected to individual photomultipliers and the scintillation is computed every second using a series of 1 ms exposures and averaged over a minute. The 4 apertures each give a measurement of σ_I^2 and a total of 6 σ_d^2 (one for each combination). The 10 scintillation measurements along with their weighting functions are then used to model a turbulence profile with 6 fixed layers or 3 floating layers using the least squares method with an approximate vertical resolution $\Delta h/h \approx 0.5$ (Tokovinin et al. (2003)). A full description of the instrument and data analysis is given in Kornilov et al. (2003). As the MASS uses scintillation it is insensitive to low altitude turbulence (the weighting function

drops to zero). While the conjugation of the instrument to a negative altitude as it is used by the generalized SCIDAR is theoretically possible, it is only possible for large apertures. For small apertures, diffraction and tracking errors become problematic and therefore not currently applicable to the MASS. Under this circumstance, the MASS is restricted to measurements of the free atmosphere above 0.5 km.

In the case of the MASS the limitation of the minimum altitude is not really a problem. As it is designed to work with a small telescope, the MASS can be combined with a DIMM module. As the DIMM measures the the seeing integrated over the whole atmosphere. The difference of seeing measured by the two instruments will therefore give the contribution of the boundary and ground layers ($< 500\ m$). A combined MASS-DIMM instrument has in fact already been manufactured (Tokovinin (2004)). Using a single module, the light from a small commercial telescope is split between the two instruments. This combination makes a small and practical turbulence profiler ideal for the testing of remote site. It can be added that while the vertical resolution of the turbulence profile obtained by the MASS-DIMM is modest, it has been shown in Tokovinin (2004b) that it is sufficient for wide-field adaptive optics simulations.

With the turbulence profiling capability of the MASS, the only remaining parameter to be determined is the coherence time. Usually requiring the knowledge of the wind speed profiles, the MASS uses an alternative method to measure this parameter. Using two exposure times τ_1 and τ_2 a new differential exposure scintillation index is calculated:

$$\sigma_{de}^2 = \langle [ln\frac{I(\tau_1)}{I(\tau_2)} - \langle ln\frac{I(\tau_1)}{I(\tau_2)}\rangle]^2\rangle. \tag{4.28}$$

From this index and a new weighting function computed numerically, one can calculate a time constant τ_{de} responsible for the temporal variation of the scintillation. It is shown in Tokovinin (2002b) that this constant is in good agreement the coherence time calculated from direct C_N^2 and wind speed measurements. The MASS is therefore capable of measuring all the atmospheric parameters relevant to astronomy.

Due to their similar approach it is reasonable to make direct comparisons between the MASS and the SCIDAR. The MASS was designed to obtain C_N^2 profiles with a small, practical and robust instrument that could be

easily used to test sites in remote locations. For this purpose, the cost of decreased resolution does not come into consideration as the resolution is good enough for most purposes. However, for the physical study of distribution and motion of turbulence in the atmosphere as well as model verifications, the SCIDAR is a more suitable instrument. A limited, yet direct comparison between the two instruments is presented in Kornilov et al. (2003). The MASS has been used continuously for three months at Cerro Tololo (Tokovinin et al. (2003) and is currently involved in the site testing of the Thirty Meter Telescope (TMT) project as well as of Dome C, Antarctica.

4.4   SLODAR

Also following ideas used by the SCIDAR, the SLODAR (SLOpe Detection And Ranging) is an instrument recently proposed by Wilson (2002) that measures the C_N^2 profile using a Shack-Hartmann wavefront sensor.

The strength and altitude of turbulence layers can be calculated from the autocorrelation of the aberration caused by the same layers. The SCIDAR makes this measurement using the speckle pattern observed at the pupil plane. The SLODAR uses the same basic idea, but does it by measuring the local slope of the wavefront instead of the scintillation. This difference is obviously driven by the existence of the Shark-Hartmann sensor that already makes this measurement for certain adaptive optics systems. Once the slope s is calculated over an array of sub-apertures (i,j), the auto and cross-correlation functions, respectively:

$$A(\Delta i, \Delta j) = \langle \sum_{i,j} s_{i,j} s_{i+\Delta i, j+\Delta j} / O(\Delta i, \Delta j) \rangle \qquad (4.29)$$

$$C(\Delta i, \Delta j) = \langle \sum_{i,j} s_{i,j} s'_{i+\Delta i, j+\Delta j} / O(\Delta i, \Delta j) \rangle \qquad (4.30)$$

where $O(\Delta i, \Delta j)$ is the number of sub-apertures of similar $(\Delta i, \Delta j)$ are computed over a large number of short exposure frames. From these function, a C_N^2 can be obtained in real time. A wavefront sensor with a grid of $n \times n$ sub-apertures will produce enough free parameters to calculate a profile with n discrete layers. The vertical resolution and maximum altitude

of the instrument are respectively:

$$\Delta h = (D/n)/\theta \tag{4.31}$$

and

$$H_{max} = n\Delta H \tag{4.32}$$

where D is the telescope diameter and θ the angular separation of the binary star. In the case of the 4.2 m William Herschel Telescope, where the SLODAR prototype is being tested, the SLODAR can reach a maximum altitude of 17 km with a resolution of 850 m using a binary star separation of 50 arc seconds (results quoted from Wilson (2002)). It is possible to optimize the SLODAR for lower layers by choosing wider apart binaries: (Wilson (2004)) successfully tested a transportable version based on a $16''$ telescope aiming at 260 m resolution over the first 2 km with a $40''$ separation binary. This level of performance is indeed very promising and competitive with respect to the SCIDAR. Another strong point of the SLODAR is its more relaxed demand for photons when compared to the SCIDAR. As it simply needs enough flux to adequately make the centroid calculation, the SLODAR can make use of the larger number of fainter binary stars available near zenith.

The qualities of the SLODAR make it the perfect profiler for telescopes using a Shack-Hartmann wavefront sensor and transportable versions using low noise level cameras are not out of reach. While the actual performance of the instrument needs to be further demonstrated, the initial comparison between C_N^2 profiles taken with the SLODAR and the SCIDAR shows a very good agreement.

4.5   Microthermal Sensors and other *in situ* methods

The most direct method to measure the turbulence profile in the atmosphere is done *insitu* using microthermal sensors. Sometime referred to as "thin wires", microthermal sensors are made of an exposed filament made of platinium whose resistance varies with temperature. Fast sampling of the temperatures measured by two carefully calibrated sensors separated by a distance ρ allows us calculate the temperature fluctuation function:

$$C_T^2 = \langle (T(r) - T(r + \rho))^2 \rangle \rho^{-2/3}. \tag{4.33}$$

The cold wires can detect air temperature variations of a few millidegrees with a response time of a few milliseconds. The guidelines for the choice of the wire dimensions can be found in Paranthoen (1985). The temperature variation is calculated from the resistance variation which depends on the metal temperature coefficient α according to:

$$R = R_0(1 + \alpha(T - T_0)) \tag{4.34}$$

where R_0 is the resistance at temperature T_0. Furthermore the static sensitivity (Volt·Kelvin^{-1}) is given by:

$$S = \frac{\alpha l I}{\sum \sigma} \tag{4.35}$$

where Σ and l are the wire section and length, I is the current intensity and σ is the electrical conductivity of the metal. Here I must been chosen small enough to keep the wire from heating and therefore the resistance becoming wind speed dependent. However the thermal inertia remains an important characteristic and is expressed by the thermal time constant M defined as:

$$M = \frac{d^2 \rho c}{4Nu\lambda_g} \tag{4.36}$$

where d is the wire diameter, ρ and c are the wire volumetric mass and heat capacity per unit mass respectively, Nu is the Nusselt number which characterise the heat transfer between the fluid flow and the wire and λ_g is the thermal conductivity of the fluid.

Typically, the sensors are placed a few tens of centimeters apart in order to remain within the sub-inertial range of turbulence and simultaneous measurements of absolute temperature and pressure are made to calculate C_N^2 using:

$$C_N^2 = (8 \times 10^{-5} \frac{P}{T^2})^2 C_T^2 \tag{4.37}$$

The sensors are used in two different ways. For the measurement of the surface layer turbulence, pairs of sensors are placed on a mast at several different heights. The turbulence profile within the altitude range of the

sensors is then interpolated using a power law (Pant et al. (1999)). To measure the profile above the surface layer, the microthermals are launched on a helium filled balloon of the same kind used for standard weather sondes. These balloons reach an altitude between 15 and 25 km before exploding in the atmosphere. In order to avoid the turbulence created by the wake of the balloon, the sensors are attached to the balloons by a thin rope at least 50 m long. An attempt to study the effect of the wake on the measurements is presented in Jumper and Murphy (2002). With typical ascent speeds of 2 to 5 m/s, the microthermals can measure the C_N^2 profile with an exceptionally good vertical resolution of around 5 m. This resolution is well beyond the reach of the optical methods mentioned earlier, so the data obtained by balloon borne sensors can be ideally used in AO simulations or to get a precise idea of the shape of the turbulent layers. Since the balloons can also carry a standard weather sonde measuring temperature, pressure, humidity and wind speed, all the critical parameters used in astronomy can be obtained on a single launch (see Fig 4.3). A good analysis of microthermal measurements using combined mast and balloon borne data can be found in Marks et al. (1996) and Marks et al. (1999). Data obtained *in situ* is widely accepted by the community and other methods of turbulence measurements are often compared with microthermal data (e.g. Bufton (1973), Abahamid et al. (2004), Borgnino et al. (1979) and Sánchez et al. (2003)).
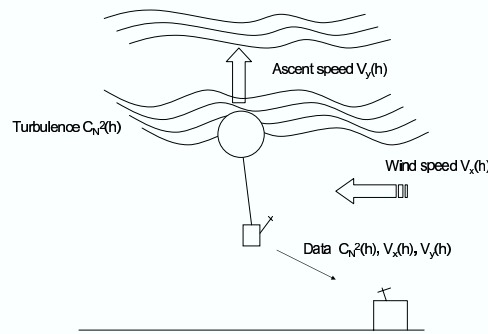
Figure 4.3: A balloon borne microthermal sonde sends the turbulence and wind profiles to a receiving station as it travels through the atmosphere.

The major drawback of this method is the impossibility of making continuous measurements of the free atmosphere turbulence. While mast based sensors can continuously monitor the turbulence, the balloon borne sensors

are limited to one profile every balloon launch, typically one per three hours. This, plus the high cost of an individual launch restricts this technique to special applications. The second disadvantage of the balloon borne measurements is the fact that the balloon is obviously carried by the wind, so the measured turbulence profiles does not correspond to the turbulence vertically above the site. This is particularly true in sites of high wind speeds although we must mention that at high altitudes, the turbulence is completely decoupled from the ground topography and heat flux and is therefore unlikely to vary significantly over the distance crossed by the balloon.

The most advantageous use of microthermal sensors is therefore in the surface layer, where a continuous, high resolution profile can be obtained. The type of sensors can also be varied to suit the conditions of the measurements. Thermocouples or sonic anenometers (Oncley (1989)) can for example be used instead of the fragile thin wires. The surface layer measurements are very important as they contain the most intense turbulence. Heat flux or dynamic turbulence created by the topography can also change fairly readily. Constant monitoring of this layer is therefore very valuable to the characterization of a site. In the free atmosphere, microthermal sensors have been used in a more restricted manner but are still used in the testing of several sites (e.g. Stalin et al. (2001) and Marks et al. (1999)).

4.6 SODAR

Specialised for the measurement of the boundary layer turbulence, the SODAR (SOund Detection And Ranging) is becoming increasingly popular in astronomical site testing. A SODAR is the acoustic equivalent of the RADAR. The instrument sends a series a acoustic pulses in the atmosphere which reflect off temperature inhomogeneities of scale similar to the wavelength of the sound wave (see Fig 5). In order to be applicable to the Kolmogorov model the wavelength of emission is therefore chosen to lie within the sub-inertial range. The backscattered signal is then collected either by the same point of emission (monostatic) or by a separate receiver (bi-static), where it is amplified. The time series of the received signal is then divided into several bins, each corresponding to a particular layer of the atmosphere (known as "range gating").

SODARs are already one of the most widely used instruments to char-
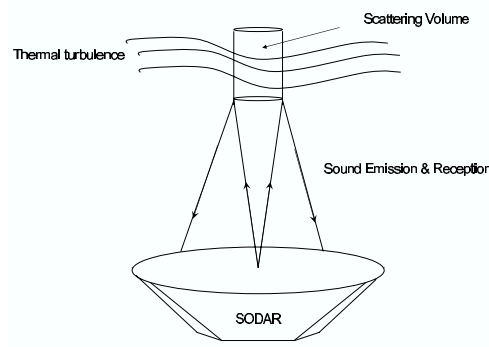
Figure 4.4: The SODAR uses the information contained in a backscattered sound wave to determine the thermal turbulence as function of altitude.

acterize atmospheric parameters in the low stratosphere (e.g. Capanni and Gualtieri (1999) and Pettré and Argentini (2001)). A full review of the different kinds and performances of SODARs can be found in Crescenti (1997). The remote nature of their sensing, together with the non-invasive nature of the measurement, makes them specially suitable for determining parameters such as mean wind speed (e.g. Neff (1988)), mixing height (e.g. Beyrich (1995)), gravity waves (e.g. Ralph et al. (1993)), low-level jets (e.g. Kotroni et al. (1994)), and the temperature structure parameter C_T^2 (e.g. Travouillon et al. (2003b)).

The basic theory of operation was derived by Little (1969). It was found that the scattered power per unit volume per unit incident flux per unit solid angle in dry air is given by:

$$\sigma_S = 0.03 k^{1/3} cos^2 \theta_S \left(\frac{C_V^2}{V_S^2} cos^2 \frac{\theta_S}{2} + 0.13 \frac{C_T^2}{T^2} \right) \left(sin \frac{\theta_S}{2} \right)^{-11/3}. \qquad (4.38)$$

In this equation, k is the acoustic wavenumber, θ_S is the scattering angle, V_S is the speed of sound and T the temperature. C_T^2 and C_V^2 are respectively the temperature and wind velocity structure constants introduced earlier. For a monostatic SODAR, C_T^2 is obtained from the relationship (Little (1969)):

$$C_T^2 = \frac{\sigma_{180} T^2}{4 \times 10^{-3} k^{-1/3}} \qquad (4.39)$$

where σ_{180} is the effective backscattering cross section per unit scattering volume per solid angle, T is the absolute temperature of air and k is the

wave number of the sound wave. The difficulty in obtaining a calibrated value of C_T^2 resides in the complexity of accurately obtaining the scattering cross section:

$$\sigma_{180} = \frac{P_r}{P_t E_t E_r} \frac{r^2}{c\tau/2} \frac{1}{S_{ant} \; exp(-2\alpha \; r)} \qquad (4.40)$$

where P_t and E_t are the electrical power applied to the transducer and efficiency of conversion to radiated acoustic power respectively. P_r and E_r are the measured electrical power and efficiency of conversion from received power. c is the speed of sound, τ is the pulse duration, r is the distance to the scattering volume, S_{ant} is the effective area of SODAR antenna and α is the atmospheric attenuation coefficient. The last two parameters make the quantitative measurement of C_T^2 difficult. Indeed α is a function of sound wave frequency, temperature and relative humidity. Values and variations of α have been experimentally studied by Harris (1966) and showed that for frequencies between 1000 and 4000 Hz (typically used by SODARs) the value of α can take values between 0 and $0.03 m^{-1}$, with the largest variations occurring between 0 and $30°C$ and relative humidities between 0 and 50%. These conditions being typical of temperate astronomical sites, SODAR calibration will be greatly affected by the meteorological conditions. Fortunately, the meteorological conditions on the Antarctic plateau simplify this problem considerably. As shown on Fig. 7 of Harris (1966) the attenuation coefficient becomes almost constant for temperatures below -10$°C$ and relative humidities above 60%. In this range we can therefore assume that the calibration would be independent of temperature and humidity.

SODARs are also capable of measuring the three dimensional wind speed profile. As the acoustic signal reflects off a parcel of air moving at speed V, its frequency f will be Doppler shifted such that:

$$V = -\frac{V_s}{2}(\frac{f_s}{f} - 1) \qquad (4.41)$$

where V_s is the speed of sound and f_s the frequency of the scattered wave. If the SODAR emits the signal vertically then only the vertical component of the wind speed will be known. In order to obtain the three dimensional wind speed vector one can use three emitters oriented in three different directions. However, the more common method is to use a "phased array" SODAR. Instead of using a single transducer, an array of smaller transducers

can be used. By appropriately phasing the emitted signal across the array the signal can be directed in a specific direction. Therefore if we consider one of the tilted beams, say pointing North, we can extract the horizontal component u_N from the frequency shift:

$$\delta f = -2\frac{u_N}{V_S}f \; sin(45) - 2\frac{w}{V_S}f \; cos(45). \qquad (4.42)$$

The combination of the three beams will therefore give us the three dimensional wind speed vector (u_N, u_W, w).

The SODAR is a robust instrument and can easily be automated to make continuous measurements. Unlike the other techniques described in this chapter it does not have a single moving part. As our experience has shown the instrument can be operated for months without a single technical failure. This robustness also means that unmanned usage is greatly simplified and instrument setup can be carried out quickly. Since we rely on acoustic waves instead of light, it is also the only instrument that can measure the evolution of boundary layer turbulence during daytime, a critical element to understand the physical processes of turbulence formation at a given site.

One of the drawback of the SODAR is the integration time of the instrument in order to reach an acceptable signal to noise ratio. The time temporal resolution of the SODAR is therefore coarser than the methods previously discussed. The range and spatial resolution is also highly variable depending on the type of SODAR as they depend on the combination of emitted power and pulse length. A large SODAR, for example, will be able to measure the turbulence up to an altitude of around 2 km with a minimum height of 50 m and a spatial resolution of a few tens of meters. A smaller SODAR, on the other end will only reach a few hundreds of meters be will be sensitive from an altitude of 10 m with a resolution as low as 5 m. In both cases, the spatial resolution is better than most other turbulence profilers. It is important to note the dependence of the SODAR performance as a function of background noise. Indeed, the SODAR data can be polluted by other sources of noise (Crescenti (1997b)) and affected by the presence of structures located near the SODAR that can reflect parts of the signal. In site testing, noise pollution is rarely a problem as they are located in remote areas.

In astronomy, the use of the SODAR is mainly aimed at observing the

Table 4.1: Instruments characteristics.

	Transportability	Cost	Vertical resolution	temporal resolution	Range	# of figures of Merit $(r_0, \theta_0, \tau_0, \sigma_I^2, L_0)$
DIMM	high	low	N/A	high	∞	3
GSM	medium	medium	N/A	high	∞	5
SCIDAR	low	high	medium	high	high	4
SLODAR	medium	medium	medium	high	high	4
MASS	high	low	low	high	high	4
Microthermal	high	medium	high	low	high	4
SODAR	high	medium	high	low	low	0

variation of the boundary layer over daily or seasonal cycles (e.g. Mastrantonio et al. (1999), Gur'yanov et al. (1992) and Forbes (1989)). The instrument range, however, limits the application of the SODAR to a local part of the atmosphere. It cannot alone measure the total seeing. It is therefore better used in conjunction with another instrument (like the MASS) to access the full turbulence profile in the atmosphere.

4.7 The Antarctic Campaign

For the Antarctic site testing campaign, the choice of instruments used to determine the turbulence conditions was made progressively and based on previously acquired knowledge. Taking place at the South Pole, the first seeing measurements were taken by a DIMM using the 60 cm infrared telescope SPIREX (Bally et al. (1996) and Loewenstein et al. (1998)). The same year, a set of microthermal sensors were installed on a mast to measure the surface layer turbulence (Marks et al. (1996)). The following year these data were completed by a series of 15 successful turbulence profiles of the entire atmosphere using balloon borne sensors (Marks et al. (1999)). The seeing results obtained from both methods gave similar results. The DIMM, placed 12 m above the ground, found an average seeing of $1.7''$ over a period of several months. The microthermals results were only marginally higher at $1.86''$. The difference can be explained either by the difference of statistical coverage between the two instruments and by the first 12 m of the atmosphere that were not sampled by the DIMM.

From those first measurements two conclusions could already be drawn. First, the seeing at the South Pole can be considered relatively poor when

compared to the leading sites where the average seeing is below an arc-second (see table 2 in Marks et al. (1999)). Secondly, it was realized from the turbulence profiles that the majority of the seeing is generated within the boundary layer. In Antarctica the boundary layer is constantly the subject of katabatic winds. The intensity of this wind and its effect on the turbulence is very dependent on the location. At the South Pole, the boundary layer is responsible for $1.78''$ of seeing within the first 220m. This is a promising result as the vertical distribution of the turbulence is very important to applications such as adaptive optics. It also means that we can rapidly improve the seeing simply by placing our telescopes higher above the ground.

The initial results taken at the South Pole deserved to be further investigated. Indeed the DIMM results were limited in time. Only 274 seeing measurements were made between the months of May and September as the SPIREX telescope was not exclusively dedicated to seeing measurements. Another DIMM was therefore built to make dedicated measurements of the seeing at the South Pole (Dopita et al. (1996)). The results, presented in this thesis, will not only help us confirm the value of the seeing previously found but will also tell us of its temporal variation in the short or long term. The results obtained by the microthermal sensors also led us to make continuous measurements of the boundary layer turbulence. As we know it contains most of the optical turbulence, the first kilometre of the atmosphere is very important and was continuously sampled by a SODAR for 9 months. The profiles taken by the SODAR will not only help us confirm the data of the few balloon borne microthermals, it will also enable us to see the evolution of this layer in time. The South Pole can therefore claim to be one of the best characterised sites when it comes to quantification of turbulence conditions. It has been sampled by two different DIMMs, microthermal sensors and a SODAR.

At Dome C, the measurement of the turbulence took a different turn. First the site testing, which is still under way, was done in collaboration with the University of Nice (as were the microthermal measurements at the South Pole). Their role is to make measurements of the integrated turbulence using a DIMM while UNSW is concentrating on the profiling of the turbulence. So far, only day time data have been taken with the DIMM (Aristidi et al. (2003)). These results, which can be considered as

preliminary, will be mentioned in a later chapter. Also, the SODAR used at the South Pole was brought to Dome C in order to make comparable measurements. As most of the turbulence at the South Pole was accessible to the SODAR, the boundary layer of the two sites is the part of the atmosphere that requires the most attention. We are therefore presenting in this thesis the state of the boundary layer turbulence at the South Pole and Dome C. We will also explain the results and the difference between the two sites using meteorological arguments. Finally, in order to complete the profile measurements at Dome C, a MASS was installed in the AASTINO. Using a small telescope located inside the AASTINO structure, this is the first version of the MASS working indoors, looking at the sky through a glass window. The data obtained by the MASS and the SODAR give us a full profile of the atmosphere with the exception of the lower 30 m.

Chapter 5

Boundary Layer Turbulence

The results in this Chapter have been published in Travouillon et al. (2003b) and Travouillon et al. (2003).

5.1   Our Instrument

The SODAR used for this experiment is a monostatic SODAR model PA1 manufactured by Remtech. Its antenna, placed on top of the AASTO, emits a series of pulses at 5 different frequencies centered at 2.25 KHz and each 0.20 second long. The antenna then switches itself to receiving mode and records the echo pattern. This routine is repeated for an averaging period of 20 minutes that also includes sequences without emission that are used to calculate the background noise. After the averaging, the SODAR returns the echo strength which is proportional to C_T^2. The wind speed is given by the Doppler shift and the horizontal wind speed and direction are derived from two acoustic beams slanted at 45° from the vertical. As previous studies have shown that the majority of the turbulence was concentrated in the lowest 300 m of the atmosphere, we configured the SODAR to make measurements from 20 m to 890 m with 30 m increments. In order to verify the accuracy of the SODAR, wind data was compared to simultaneous balloon launched meteorology measurements. These data showed good agreement over the whole altitude range covered by the SODAR.

Data were accumulated almost continuously every half-hour from the 13th of February 2000 to the 11th of November 2000. After elimination of poor signal-to-noise data, there are a total of 8,644 sets of measurements.

As the SODAR is not able to calculate the temperature and atmospheric pressure as function of height, the data from daily weather balloon launches were used to convert C_T^2 to C_N^2. A linear interpolation was used for altitudes where temperature and pressure data were not available. We also made the assumption that the temperature and pressure temporal fluctuations are small over a period of 24 hours because of the continuous night time.

5.2   Calibration

In this section I describe how the SODAR was calibrated against measurements made by microthermal sensors.

SODARs rely on the backscattering of acoustic waves by thermal inhomogeneities that can be described by the parameter by C_T^2. After a pulse is transmitted into the atmosphere by the SODAR, it is backscattered to the SODAR's receiver which amplifies the signal and digitises it before analysing it to obtain all the desired wind parameters.

Direct and absolute calibration of Doppler SODARs C_T^2 is difficult. Beyond the temperature and humidity dependence described in the previous chapter, a direct calibration would require the knowledge of emission and reception efficiencies of the instrument (also temperature dependent) as well as the altitude (or pressure) dependance of the attenuation coefficient. Since such information is not available in the literature and beyond the experimental scope of this thesis we have chosen to carry out a relative calibration using microthermal sensors.

The type of calibration must take into account two properties of the instrument: its range and its integration time. The range is limited by the finite acoustic power of the instrument and the ambient noise conditions. SODARs therefore have a detection threshold which should be constant under stable noise conditions. The integration time of a SODAR affects the spatial resolution of the instrument, rendering a cross-calibration difficult.

5.2.1   Integration time

In order to obtain a satisfactory signal to noise ratio, SODARs must integrate pulses over a time varying from a few minutes to an hour. This integration time depends on the amount of signal backscattered by the turbulence that is necessary for the machine to compute the wind parameters

(manufacturer dependant). A SODAR C_T^2 profile is therefore an average profile over the time of integration of the instrument.

The microthermal sensors that we use for the calibration give, in contrast to the SODAR, a profile of instantaneous C_T^2 values. During the time of integration, the turbulence profile is likely to change and move. To avoid situations where the thermal turbulence is changing rapidly during the integration, the calibration can be done during the night. The effect of horizontal motion of the turbulence can be minimised by performing the calibration during low wind speed and timing the launch of the balloon to coincide with the beginning of an integration. The more significant change however is the vertical motion of the turbulence. During the integration time, the turbulent cells will travel within the boundary layer. This effect therefore spreads and shifts the turbulent laminae for the period of the integration. To address this issue, instead of calibrating the SODAR using individual data points, we integrate the whole C_T^2 profile of the SODAR and of the microthermal sensors:

$$\int C_T^2(sodar) = k \times \int C_T^2(microthermal) \qquad (5.1)$$

where k is the dimensionless calibration coefficient and both integrals are taking over the SODAR profiling range. This technique assumes only that the vertical motion of the turbulence stays within the integrated region during the SODAR measurement. This assumption was justified during our calibration, as the SODAR range always extended well beyond the boundary layer and no turbulent peak was found close to or above the integrated region. This effect will be illustrated in the data presented in the next chapter.

5.2.2 Range

Two external parameters affect the range of a SODAR. First is the ambient noise. The noisier the site, the lower the signal to noise ratio and therefore the lower will be the maximum range that the SODAR can measure. Sources of noise and their remedy have been reviewed by Crescenti (1997b). In a constant noise environment, the only other variable that can determine the range of a SODAR is the intensity of the turbulence itself. A given SODAR will require a certain minimum signal strength which means that there must

be a minimum turbulence level necessary to backscatter enough signal to the instrument's receiver. This effect was observed by Crescenti (1998) who found that longer ranges were achieved in unstable atmospherical conditions.

Following the same logic as the previous section, the minimum C_T^2 measurable by the SODAR can not be calculated using individual points. Instead, we aim to determine the minimum level of turbulence measurable by the SODAR at a particular background noise level by using balloon borne microthermal sensors and averaging their turbulence background. For each individual balloon flight, we select the places in space where the turbulence is below the SODAR threshold and we integrate the C_T^2 of the microthermal sensors at the corresponding altitudes:

$$\int C_T^2(\star) = \int_{b.ground} C_T^2(microthermal) \tag{5.2}$$

where $C_T^2(\star)$ is the detection threshold of the SODAR. The knowledge of this value can help us determine the maximum level of turbulence potentially present at a particular altitude when the backscattered signal is too weak for the SODAR.

Equations 5.1 and 5.2 together define the two coefficients of the linear relationship of the calibration of the SODAR using the microthermal sensor C_T^2 profile:

$$C_T^2(microthermal) = k \times [C_T^2(sodar) + C_T^2(\star)] \tag{5.3}$$

The details of the actual calibration run are described below.

5.2.3   Experimental setup

Our SODAR is a monostatic mini-SODAR, model PA1, manufactured by Remtech. It uses an array of 52 transducers and an acoustic power of 1 W at a central frequency of 2.25 kHz. The quoted system maximum range is 900 m at 35 dB ambient noise, 700 m at 40 dB and 450 m at 50 dB. This instrument was chosen for its low power consumption (25 W) and the small size of its antenna (0.65 m × 0.65 m), two important constraints for our use of the instrument. The SODAR was calibrated against microthermal sensors developed by the University of Nice that are widely used in the determination of turbulence profiles above major astronomical sites (e.g.,

Azouit et al. (1980) and Marks et al. (1999)).

The calibration took place at the Observatoire de Haute-Provence (OHP) in the south of France, at an elevation of 650 m. A total of 5 nights were used between July 20 and July 25 2002. Each night, three balloons were launched. Beside the microthermal sensors, the balloons carried standard VAISALA weather sondes capable of measuring temperature, pressure and wind velocity profiles. The balloons were helium filled from the OHP interferometry laboratory in order to set up the sensors under cover from the wind. They were then launched from the OHP main entry road that is oriented parallel to the prevailing wind in order to avoid the collision of the sensors with trees during strong winds. The first flight was launched immediately after dusk. Each flight typically took two hours to reach an average height of 20 km and then back, sending back the weather and turbulence data at a spatial resolution of roughly 5 m. Three sondes were launched every night using this method for a total of 15 flights for the 5 nights.

The SODAR was positioned between the interferometry laboratory and the road, at about 30 m from the launching point. This position was chosen because of the reasonable distance to any building or trees that could interfere with the sounding, the flatness of the surface and the length of the power cord (30 m) that stretched from the interferometry laboratory. The SODAR was left running continuously all night and monitored from the SODAR control computer installed in the laboratory where the sondes were prepared. We set the SODAR sampling range from 30 m to 900 m with 30 m increments and an integration time of 20 minutes. Each balloon launch was timed to coincide with the beginning of an integration. The microthermal sensors having a better spatial resolution than the SODAR, their data were convolved to fit the resolution of the SODAR.

Out of the 15 microthermal and SODAR data sets obtained simultaneously, only 7 were selected using the following criteria:

1. The ambient noise must be 35 $dB\pm2.5$ to guarantee a constant natural range of 800 m. This ensures that the only cause for an absence of data below this height is that the magnitude of turbulence is too low for the SODAR to detect.

2. The signal to noise must be above 70 (as measured by the Remtech SODAR). This criterion was always met, and it ensured that the data
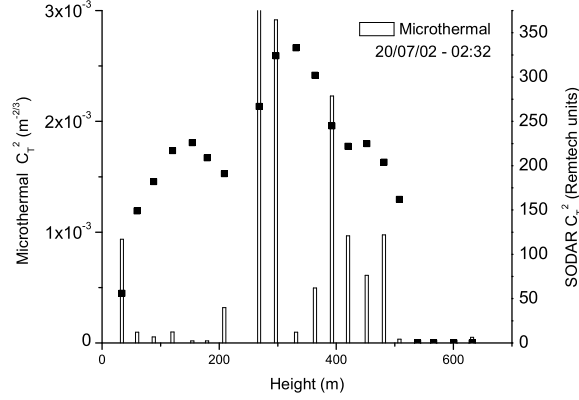
Figure 5.1: Microthermal (line) and SODAR (dots) turbulence profiles of the 20/07/02 at 2:32UT

did not suffer from electrical or vibrational noise.

3. The microthermal profile must not show any turbulence peaks between the end of the SODAR range and 1,200 m. This minimises the chance that extra turbulent energy will move in and out of the SODAR range during the integration as explained in the previous section.

Figure 5.1 to 5.7 illustrate each of the seven pairs of profiles fulfilling these three criteria.

5.2.4   The wind speed measurements

In 2000, the SODAR was run semi-continuously at the geographic South Pole for a period of 8 months. While the purpose of this experiment was to obtain turbulence measurements of the boundary layer (Travouillon et al. (2003b)), the wind speeds were also recorded. The SODAR's antenna was installed on the roof the the AASTO (Automated Astrophysical Site Testing Observatory)(Storey et al. (1996)). While the outside temperature regularly reached $-60°C$, the base of the antenna was heated from the inside of the building and kept above freezing point. All the electronics were kept inside at ambient temperature. The AASTO was well isolated from other buildings and the average background noise was around 35 dB.

During that season the South Pole meteorological team launched weather balloons on a daily basis. These balloons carrying VAISALA sondes similar
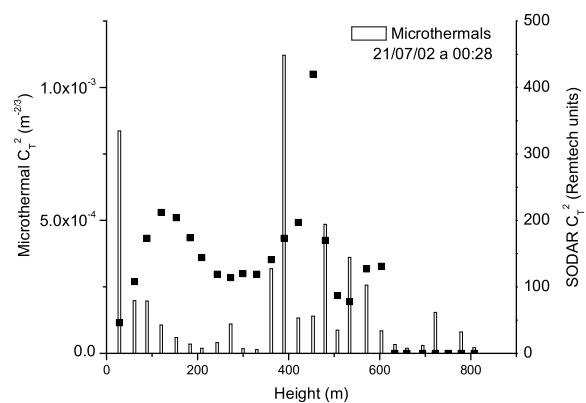
Figure 5.2: 21/07/02 at 00:28UT
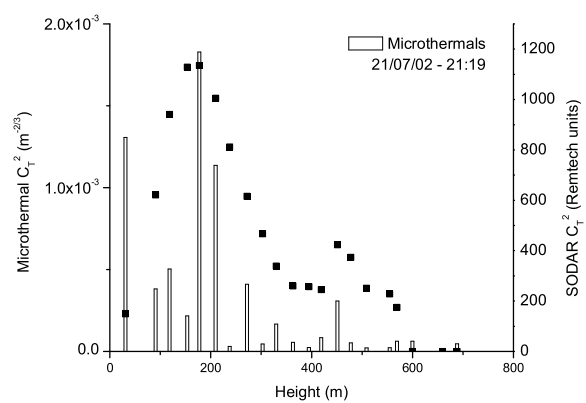
Figure 5.3: 21/07/02 at 21:19UT
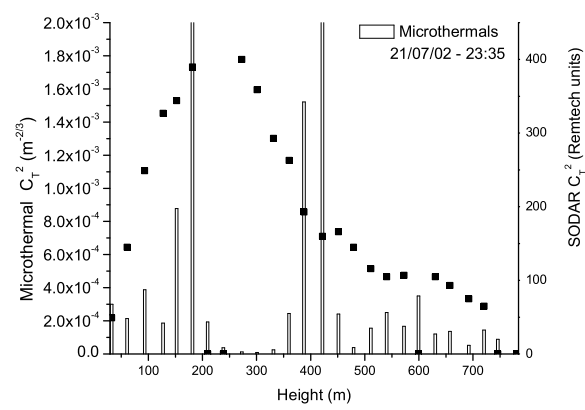
Figure 5.4: 21/07/02 at 23:35UT
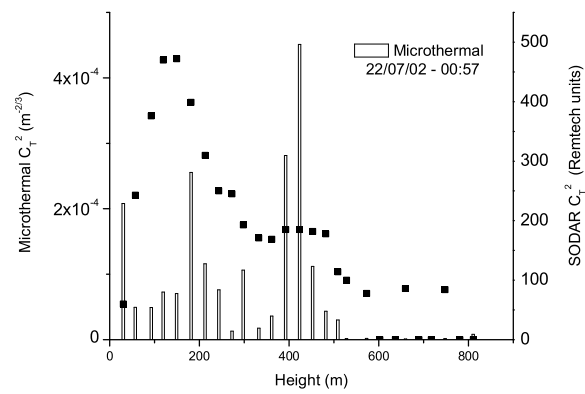
Figure 5.5: 22/07/02 at 00:57UT
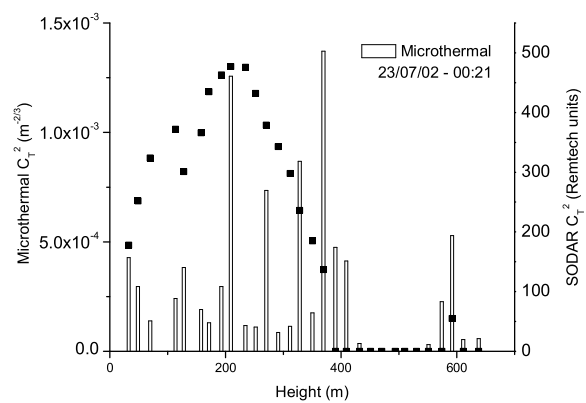
Figure 5.6: 23/07/02 at 00:21UT
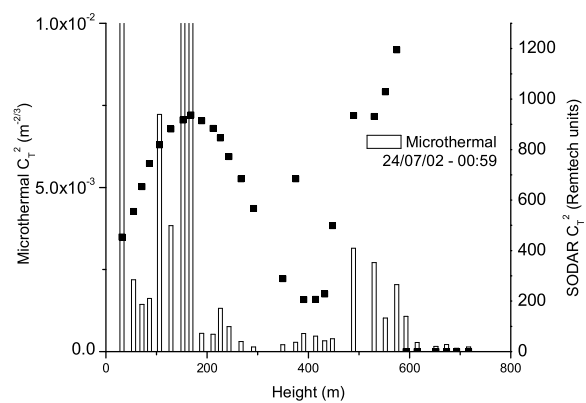
Figure 5.7: 24/07/02 at 00:59UT

to the one used at the OHP were capable of measuring the wind speed and direction by GPS tracking. During this whole season, 60 of these flights took place within a SODAR integration. It is important to note that the launching site of the balloons was 1km away from the AASTO as its isolation was important for several experiments carried by the observatory. However, no building or elevated terrain lies between the two sites and so it is expected that the wind conditions would not greatly differ.

We are analysing the results of the 60 balloons flights and the corresponding SODAR profiles. The wind speeds will be compared at an altitude of 50 m, 300 m, and 700 m.

5.2.5 Calibration coefficient of proportionality

Each of the seven pairs of turbulence profiles shows a good correlation between the two instruments. The broadening of the SODAR peaks which results from the time averaging can be associated with one or several turbulence layers present in the microthermal profile at similar altitude. Fig 5.4 is the best example, showing two individual peaks on the two instruments at the same altitudes. The presence of multiple peaks, as in Fig 5.6, broadens the SODAR profile even further making the association of the corresponding peaks difficult (justifying the need to integrate each profile for the calibration). It is interesting to note that in several profiles (Figs. 5.2, 5.3, 5.5 and 5.7), the surface layer makes an appearance above 30 m where the first SODAR point is plotted. Surface layers of turbulence are mechanically created by the terrain and are usually spatially stable. We therefore do not believe they will have a significant contribution to the SODAR profile as they will stay within the near field of the instrument.

The results of the calibration are summarised in Table 5.1. The calibration coefficient and the minimum detectable signal of the SODAR where derived respectively from Eq 5.1 and Eq 5.2. The calculation of the coefficient of proportionality k shows a very good agreement between the two instruments. Fig 5.8 illustrates integrated turbulence as measured by the two instruments. The correlation of 95% confirms the validity of the method. The use of this coefficient will allow the SODAR to measure absolute values of C_T^2 without the further need for *in situ* measurements.

Table 5.1: Summary of the calibration parameters of the SODAR PA1.

Parameter	Mean ($\times 10^{-6}$)	Error ($\times 10^{-6}$)	Correlation (%)
k	1.62	0.09	95
$C_T^2(\star)$	5.4	1	-

5.2.6 Detection threshold

Fig 5.9 shows in a similar way the result of the calculation of the SODAR's detection threshold. This time, however, we consider the maximum value as being the representative one. It is the case because any C_T^2 value below that maximum would be even lower than this undetected turbulence. The first flight on Fig 5.9 shows the maximum undetected turbulence level, and therefore is the one we use as our detection threshold (values reported in Table 5.1). It is important to note that the calculation of $C_T^2(\star)$ is only valid in a background noise range of 35 $dB \pm 2.5$ dB as described earlier and further experimentation in a wide range of noise conditions would be necessary to extend this calibration to other noise levels. We are confident that a similar noise background will be easy to find at other observatories as they are located at remote sites and therefore do not usually suffer from primary sources of noise such as roads, wildlife and machine activity.

In order to assess the capability of this type of SODAR to measure turbulence in stable atmosphere conditions, we have calculated the seeing parameter (Fried (1966)) at zenith:

$$\varepsilon_{FWHM} = 5.25\lambda^{-1/5}(\int_0^\infty C_N^2(h)dh)^{3/5} \qquad (5.4)$$

The seeing is a function of wavelength of that light (λ) and of the integral of C_N^2 over the part of atmosphere of interest. By comparing the minimum seeing value that would be measurable by the SODAR and comparing it with typical values recorded at astronomical sites, we can determine wether the instrument sensitivity is suitable for turbulence measurements in a stable atmosphere. We therefore calculated the minimum seeing measurable by the SODAR by combining typical pressure and temperature profiles with our minimum C_T^2 value. We found that for the commonly used wavelength of 500 nm the minimum seeing measurable by the SODAR within the first 900 m of the atmosphere was $\varepsilon_{FWHM} = 0.05''$. This result is about an order of magnitude lower that the boundary layer component of the seeing
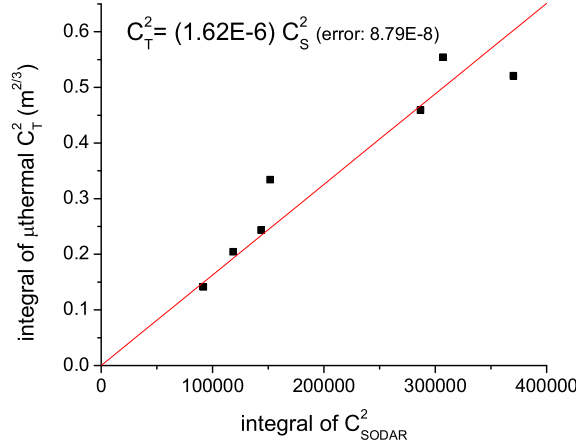
Figure 5.8: Result of the calculation of the coefficient of proportionality between the two instruments' total turbulence. Each point corresponds to one of the seven valid pairs of profiles.

in the sites listed in Table 2 of Marks et al. (1999). This shows that the SODAR's minimum detection is well below the typical level of turbulence in sites already famous for their stable atmosphere. It can be noted that the SODAR detectivity should be altitude dependent because of the absorption of sound waves during their propagation trough the atmosphere. However, our attempt to make such dependence a part of the calibration was unsuccessful as the variations of C_T^2 in time were larger than the effect of altitude difference.

5.2.7   Wind speed comparison

The results of the wind speed comparison are shown in Fig 5.10. Similarly to the calibration, the measurements are expected to suffer from the SODAR's integration time. While the balloons sensors measure instantaneous values of the wind vectors, the SODAR results must be considered as averages over a 20 minute period. As such, Fig 5.10 shows that the measurements taken at 50 m and 300 m by the two instruments are in good agreement as in each case, only one point is out by more than a factor of two. It is also interesting to note that the lower wind speeds, that are closer to the average wind speed of the site (5.8 m/s) compare better than higher speeds which are very likely to be short gusts. The data at 700 m on the
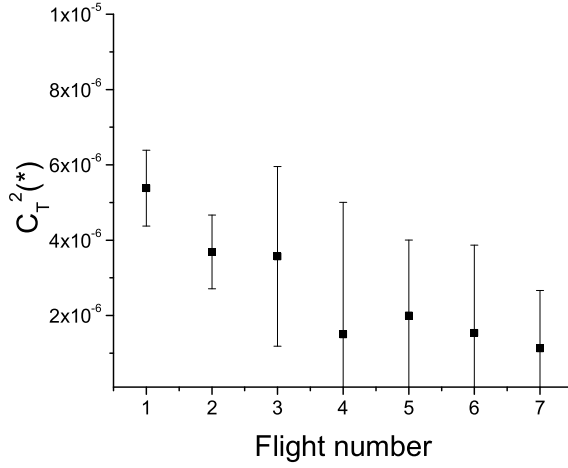
Figure 5.9: Result of the calculation of the SODAR's detection threshold for each of the seven profiles.
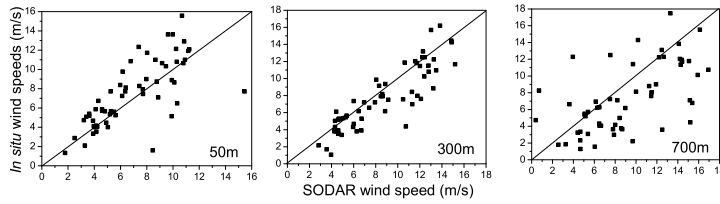
Figure 5.10: Comparison of the SODAR's wind speed measurements with the weather balloons at an altitude of 50 m, 300 m and 700 m

other hand have more discrepancies. At this altitude, the SODAR data is frequently overestimating the wind speed and the spread in the results is much larger than for the two lower altitudes. We believe that the poor reliability of the wind speed measurements at this altitude is caused by the limited amount of signal returned so close to the instrument range. At this altitude the turbulence is weak and therefore the S/N required for the wind speed measurements barely adequate. Microthermal measurements done at the South Pole by Marks et al. (1999) have shown that C_T^2 drops by more than two orders of magnitude within the first 400 m of the atmosphere. The wind speed estimates are therefore accurate only with the zone of strong turbulence

The calibration method we present gave satisfactory results. It allows us to calibrate the SODAR in terms of absolute values of C_T^2 and also gives an order of magnitude estimate of its detection threshold. We also obtained a good wind profile comparison that validates the usefulness of the SODAR to make average wind speed and direction measurements within the turbulent boundary layer. The comparison was, however, unreliable close to the range limit of the instrument.

5.3   South Pole Campaign 2001-2002

5.3.1   Turbulence and boundary layer evolution

From here on, we define the boundary layer altitude as being the height above which the turbulence amplitude is below the SODAR threshold of detection. Calibration has shown that this threshold is two orders of magnitude lower that the average turbulence.

The turbulence measurements taken from the 8,600 sets of data are displayed in Fig. 5.11. The boundary layer altitude is of primary importance when studying a potential telescope site in Antarctica. During the period of our measurements, the turbulence is concentrated on average below 270 m. It is notable that this is higher than the 220 m estimate by Marks et al. (1999)), who accumulated data from late June to mid August, the time of year giving the best seeing conditions of the site. This is in the peak of winter (June and July), when there is the largest temperature gradient and the most concentrated boundary layer, including a long period of stable atmosphere (9 days of July have derived seeing below 0.2″). Early and late winter conditions are, however, much more unstable. Periods of low altitude boundary layer are mixed with periods of extended boundary layer and periods having dual layers. Figure 5.12 shows the frequency of occurrence of boundary layer altitudes.

The boundary layer height often falls into one of the three bins. The first bin includes the first 30 metres of the atmosphere. It corresponds to a virtually turbulence-free atmosphere, which is mainly present between mid June and the beginning of August. Through out the year, these periods of stable atmosphere correspond to 18% of the time sampled. The second bin, centred at 260 m, represents the most common boundary layer altitude with an occurrence of 21%. This kind of boundary layer is evenly distributed
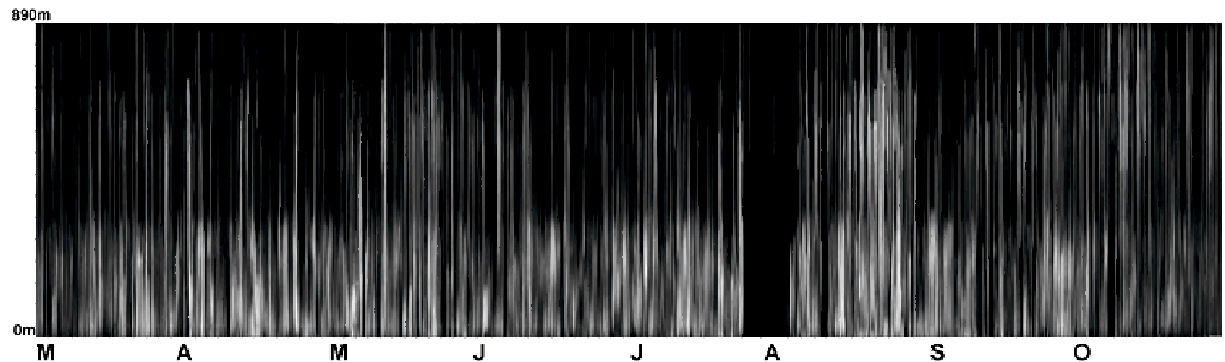
Figure 5.11: "Facsimile" plot of the turbulence profile between March and November 2000 (the letters on the x-axis mark the beginning of the month). The y-axis shows altitude from 0 to 890 m while the brightness intensity shows the turbulence intensity. The turbulence intensity drops sharply between 200 and 400 m, defining the boundary layer height.

with time and is a good indication of the expected boundary layer altitude. The third and last bin occurs at 690 m (present in 17% of the data). It corresponds to a secondary, usually less intense, drop of the turbulence level. This type of boundary layer is more frequent in the weeks surrounding the sunset and the sunrise and is absent from the peak of winter. These 3 types of turbulence behaviour will be further examined in conjunction with meteorological parameters in the next section.

The evolution of the boundary layer height during the year shows a seasonal trend. It drops continuously month after month and reaches a minimum in July, the peak of winter. It then rises again closer to summer and sunrise (See figure 5.13). This effect is due to strengthening of the temperature inversion in winter because of the lack of radiative heating. The total amount of turbulence does not, however, follow a similar pattern. While the turbulence is still minimum in July, there is not a direct correlation between the height of the boundary layer and the total amount of turbulence in the atmosphere.

5.3.2 Meteorological parameters

The boundary layer evolution throughout the year is dependent on two parameters. The first one is the temperature gradient, around which Kol-
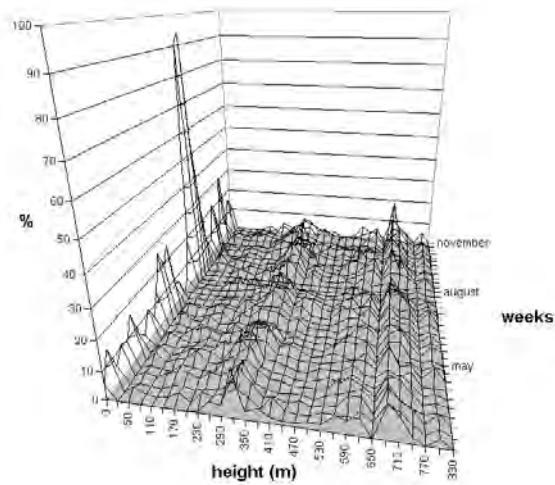
Figure 5.12: Frequency of boundary layer height. The data are binned into weekly average (first horizontal axis) as a function of height (second horizontal axis) and the result expressed in relative percentage (vertical axis).

mogorov's theory of turbulence is built. The second parameter is the wind speed. The katabatic winds generated on the high plateau of Antarctica gain speed as they descend across the topographic contours of the continent. The South Pole station is at a relatively high altitude (2,835 m) and the wind speed is much weaker than it is near the coast. It is however strong enough, with ground speeds of 20 m/s regularly recorded, to induce turbulence. Figure 5.14 and 5.15 show the close relation between C_T^2 and the horizontal wind speed at corresponding altitudes. The correlation between wind speed and turbulence level has previously been recorded in the coastal regions of Antarctica (Yague et al. (2001)) and is confirmed to be present on the plateau by our measurements. The majority of the turbulence is located below the altitude of 300 m with a secondary and lesser peak at 600 m. The wind profile follows a similar pattern. In fact, the correlation coefficient between C_T^2 and wind speed, using the averages over the whole data as a function of altitude, is a high 91%, suggesting that wind speed measurements alone could give a good representation of the turbulence profile.

The vertical component of the wind velocity can be further related to turbulence and wind behaviour. Figure 5.16 shows the average vertical wind speed as a function of height. The boundary layer is characterised by a layer of upward wind 240 m thick and corresponding to the altitude range of high
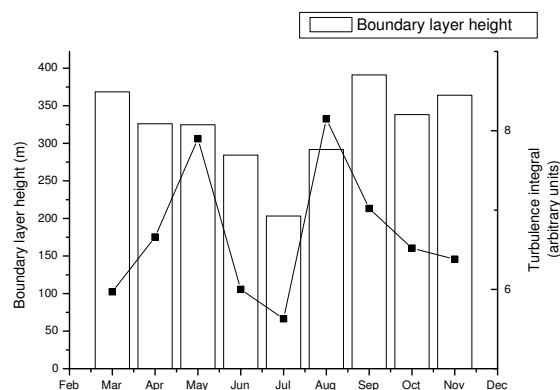
Figure 5.13: Monthly distribution of the boundary layer height (columns) and of the total turbulence (line). The boundary layer height evolves according to the seasons, decreasing in altitude towards the peak of winter and increasing again towards sunrise. The total amount of turbulence, on the other hand, does not follow a similar trend.
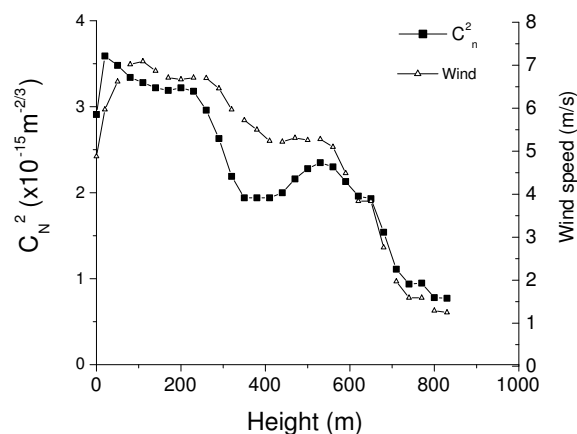
Figure 5.14: Turbulence (empty square dots) and horizontal wind speed (averaged over the whole data set). Both curves display drops at 300 m and 600 m, representing the two most common boundary layer altitudes.
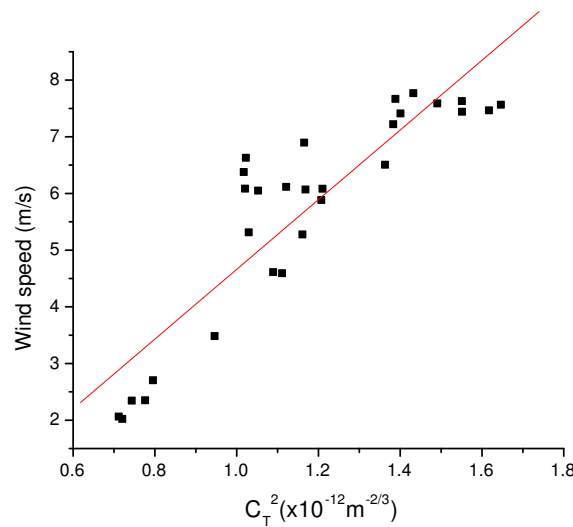
Figure 5.15: Correlation between average horizontal wind speed and temperature fluctuation constant. Each point represents an average at a particular height (similar to fig 5.14). Also displayed is the line of best fit that is constrained to pass through the origin.

turbulence. Once again, a correlation analysis shows that the height of the boundary layer and the height of the wind inversion strongly matched, with a correlation coefficient of 92%.

As previously noted, each turbulence profile can be assigned to one of three categories which account for 56% of the data observed. The remaining 44% corresponding to states of transitions between the three states. The first type of turbulence profile (type 1) that is encountered in 18% of the data is characterised by a thin, ground level, turbulence layer followed by a perfectly stable atmosphere above 100 m. The most common type of profile (type 2) occurs 21% of the time and corresponds to a thick boundary layer occupying the lower 300 m of the atmosphere. The last type of profile (type 3) is a more extended boundary layer showing a secondary and lower peak of turbulence at around 600 m and is visible in 17% of the data. Figures 5.17, 5.18 and 5.19 show an example of the three types of turbulence and wind profiles recorded by the SODAR as well as the temperature gradient measured on the same day.

The relationship between turbulence and horizontal wind speed described
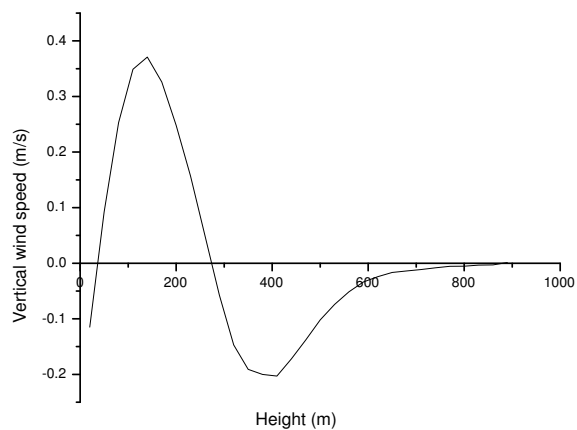
Figure 5.16: Average vertical component of the wind speed expressed as a function of altitude. Positive values are upward. They are located over an altitude range similar to the peak turbulence layer.
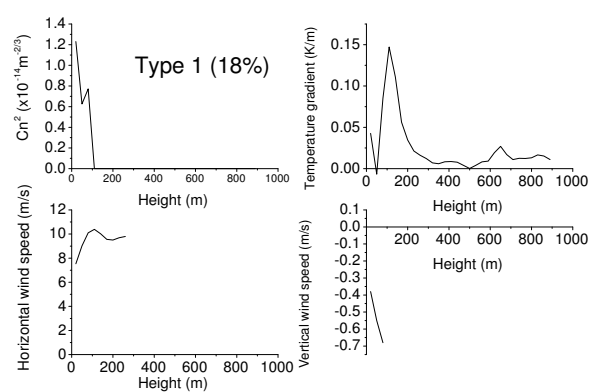
Figure 5.17: Typical profiles of type 1 turbulence: Semi-stable atmosphere, ground level turbulence. The plot was truncated when the turbulence became too small to be measured.
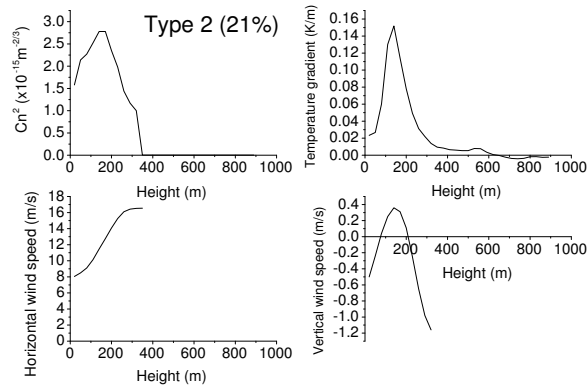
Figure 5.18: Type 2 turbulence: Concentrated boundary layer.
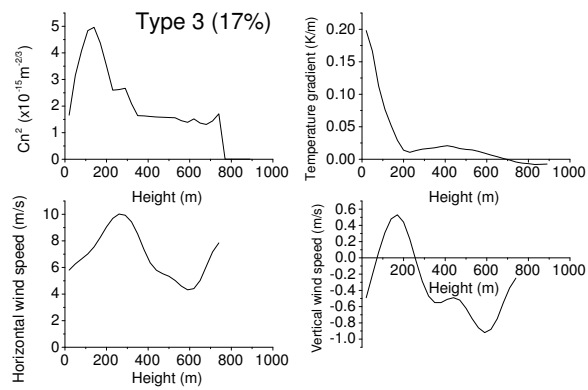
Figure 5.19: Type 3 turbulence: Extended, 2 component boundary layer.

earlier is independent of the type of profile taken by the turbulence. When the turbulence is located in a concentrated altitude boundary, the winds also reach large velocities in a similar pattern. For an extended turbulence like type 3, the wind profile also becomes more complex. The correspondence between upward winds and turbulence works very well for turbulence of type 2 and 3 where the peak turbulence corresponds to the peak wind speed. For a type 1 turbulence however, the vertical wind remains negative. The ground level turbulence is therefore not associated with change of wind direction, as it is the case with higher altitude turbulence. This observation implies that the turbulence is generated at ground level (< 100 m) when the winds blow uniformly downward but can be "carried" to higher altitudes as the wind changes direction.

5.3.3 Seeing

Having described the turbulence profile under 1000 m, we can now assess the seeing quality of the site. Since the seeing depends on the integration of C_N^2 over the whole atmosphere, it is necessary to estimate of the amount of turbulence above the measurable range. Because of the latitude of the site and its flat topography, there is no reason to expect major turbulence above the boundary layer. To confirm this assumption, we computed the Richardson number as a function of altitude for every day of observation. As described in Marks et al (1999), the criteria for turbulence is:

$$R_i = \frac{g}{\theta} \frac{(\partial \theta / \partial h)}{(\partial v / \partial h)^2} < \frac{1}{4} \, , \tag{5.5}$$

where g is the gravitational constant, v the horizontal wind speed and θ the temperature. v and θ were obtained from balloon measurements. Using this description, 91% of the time, no turbulence is present above 890 m. The evaluation of the seeing and other relevant atmospheric parameters is therefore an estimate applicable to these 91% of the data. The statistics are summarised in Table 5.2 and in figure 6.3. The values there are in close agreement with seeing measurements taken at the South Pole (Marks et al. (1999) and Loewenstein et al. (1998)). The seeing contribution arising above 300 m is also displayed in order to emphasise the influence of the boundary layer. In fact, the average seeing could be decreased from $1.73''$ to $0.37''$ by observing at this altitude.

Table 5.2: Summary of the seeing measurements averaged over the whole data set.

Measurement	Mean	Std. Dev.	Median	Best 25%
Total Seeing ($''$)	1.73	1.07	1.59	1.17
Seeing above 300 m	0.61	-	0.37	Below detection range
Boundary layer height	267	280	204	70
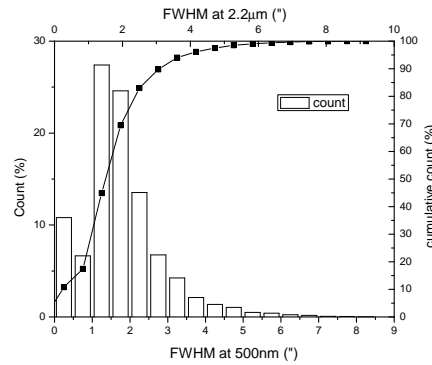
Figure 5.20: Seeing cumulative distribution and distribution (expressed as percentages) for the ensemble of the data taken between March and November 2000.

5.3.4   A telescope on a tower

Simulating the evolution of the seeing during the year as a function of height of a telescope by integrating equation 3.38 from an altitude h to the top of the atmosphere, it is readily seen how it drops to an undetectable range quickly after the boundary layer. Figure 5.21 shows this evolution calculated from monthly averages. The overall behaviour of these profiles is similar at all times, but the months of winter show sharper drops with altitude as well as lower median values. It is important to note that the lower limit of the seeing reached in all the profiles is fairly qualitative as they usually attain the limit of measurability of the SODAR. The overall seeing distribution is described by figure 6.3 and is in good agreement with seeing measurements made with microthermal sensors and previously discussed by Marks et al (1996).
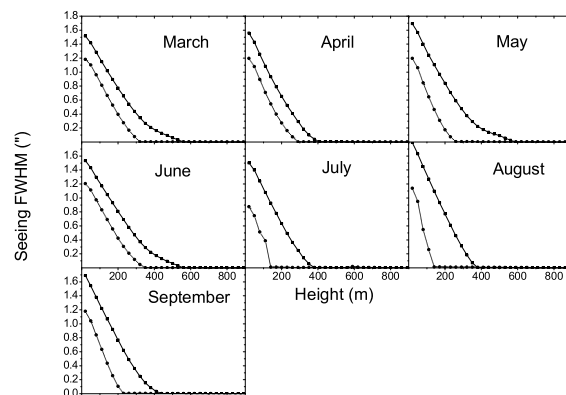
Figure 5.21: Monthly representation of the seeing as a function of telescope altitude above the ground. The mean is represented by the full lines and the median values by the dotted lines.

5.3.5 Other astronomical parameters

While the ground level seeing conditions of the South Pole do not match those offered by the best Chilean and Hawaiian sites (Fuchs (1995) and Roddier et al. (1990)), the unique turbulence profile typical of Antarctica is ideal for image correction schemes such as adaptive optics. As given by equations 3.43 and 3.47, the two parameters ruling the conditions of correction are the isoplanatic angle and the coherence time.

The isoplanatic angle can be seen as the part of the sky inside which all parts of the image distort with the same phase. Adaptive optics relies on a guide star in order to compensate for the image variation. This reference star must belong to the same turbulence field in order to correct the seeing properly (Fusco et al. (2000)). The larger the isoplanatic angle, the larger the chance is of finding a bright star in phase with the observed object. The isoplanatic patch depends critically on the altitude distribution of the turbulence. The lower the turbulent cell, the larger the angle it will occupy in the sky. In Antarctica, the light passes through only one layer of turbulence concentrated at low altitude, and conditions for adaptive optics correction are therefore considerably superior to other sites.

The coherence time is the time equivalent of the isoplanatic patch. The amount of time in which a cell of turbulence remains in the field of view

Table 5.3: Summary and comparison of the South Pole correction parameters at 500 nm with two temperate sites. Data for Cerro Paranal and La Palma are courtesy of Fuchs (1995) and Vernin and Munoz-Tunon (1994) respectively.

Site	$\theta_{AO}('')$	$\theta_{SI}('')$	τ_{AO}(ms)	τ_{SI}(ms)
South Pole (total)	3.3	2.8	2.9	13
South Pole (B.L correction)	63	193	3	35.5
Cerro Paranal	1.45	1.88	-	-
La Palma	1.3	2.2	7	13

will determine the length of time over which the correction is accurate. Since turbulent cells are moved around by the wind, it is the wind speed distribution that will dictate the time of coherence. Again, the South Pole wind conditions are ideal as they are only substantial within the boundary layer. Table 5.3 summarises the values for these parameters and compares them with the sites of Cerro Paranal, in Chile and La Palma, in the Canary Island. The figures of the South Pole exceed the other two sites by up to a factor of fifty. Temperate sites suffer from a very high altitude turbulence coming from the jet stream. The convection that the jet stream gives birth to multiple layers of turbulence, all of them located at high altitude.

Two other parameters, that are not the subject of this paper, but potentially derivable from the SODAR measurement, benefit from the South Pole turbulence distribution. Interferometry suffers from phase error that is again dependent on the altitude of the turbulence. The mean square error for an astrometric measurement with a dual-beam, differential interferometer is as described in Lloyd et al. (2002):

$$\sigma_\delta^2 = 5.25 B^{-4/3} \theta^2 \int h^2 C_N^2(h)(Vt)^{-1} dh \qquad (5.6)$$

where B is the baseline of the interferometer, θ is the angular separation of the celestial objects, V is the wind speed as a function of height and t is the total integration time. The h^2 factor in this equation shows the advantage that a low altitude turbulence can have on astrometric measurements. In Lloyd et al. (2002), a turbulence model adapted from existing data compares the mean square error of South Pole with Mauna Kea. The results show that the South Pole mean square error is a factor of 15 better than in Hawaii

where the turbulence is mainly located a few thousand metres from the ground. The construction of an interferometer in Antarctica could therefore make use of such unique atmospheric conditions.

Flux variation measurements also take advantage of the low altitude turbulence of Antarctica. Observations of variable stars and solar pulsations (Fossat et al. (1981)) are limited by the change of flux created by our own atmosphere. These changes are expressed by the scintillation index:

$$\sigma_I^2 = 19.12\lambda^{-7/6} \int h^{5/6} C_N^2(h) dh \qquad (5.7)$$

and correspond to the variation of the intensity of the studied object. The altitude dependence of the scintillation is not as important as it is on the astrometric error. It is however important enough to make the scintillation at the South Pole smaller than at Cerro Paranal by a factor of 2, based on the microthermal data of Marks et al. (1999).

The relations built between wind speeds and direct measurement of turbulence which are summarised in table 5.4, help us understand the evolution of the turbulence profile throughout the year. During winter period the most well defined boundary layer is observed. Closer to day time, the more the turbulence diffuses out to higher altitude. In winter, the ice cools faster than the transparent atmosphere. We therefore observe a large temperature gradient close to the ground and its associated turbulence. In summer the sun heats the air closer to the ground. It has the effect of lowering the temperature gradient of the low atmosphere and in consequence also lowering the intensity of the turbulence in this area.

Figure 5.22 shows the high correlation between the size of this wind inversion and the altitude of the mixing height (altitude at which the temperature starts decreasing). The second effect of the radiative heating is the extension of the warmer layer of air close to the ground to higher altitudes. The elevation of the mixing height therefore also raises the size of the boundary layer (Neff (1981)). Often, this elevation gives birth to a secondary peak near the mixing height. While this effect is unexpected it has been observed before at the coastal base of Halley (Rees and Mobbs (1988)). While this secondary peak limits the efficiency of using a tower to increase the seeing quality, the low occurrence of this extended turbulence justifies elevating the telescope. As every ten metres has a large impact on the improvement
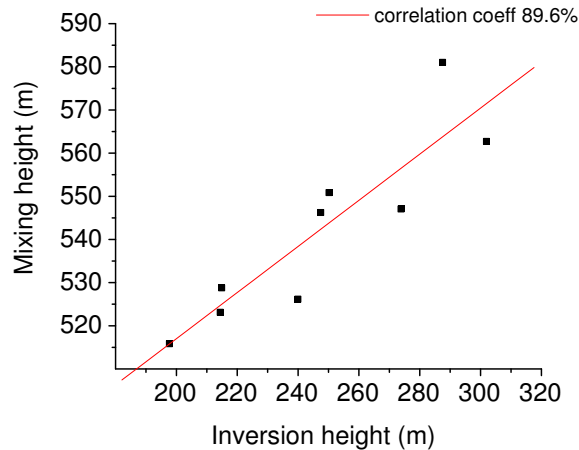
Figure 5.22: Plot of the mixing height (altitude at which the temperature starts decreasing) as a function of the wind inversion height. Each point corresponds to a monthly average.

of the seeing, the maximum seeing limitations of an adaptive optics system will dictate the altitude at which telescopes must be built.

5.4   Dome C Campaign 2003-2004

In this section we present the low altitude turbulence measurements taken at Dome C using the same SODAR used previously at the South Pole. In order to obtain perfectly comparable results, we have kept the same hardware and software configuration. The SODAR antenna was installed on the roof of the AASTINO in thermal contact with the interior of the building. The SODAR was stopped between 23:00 and 3:00 while the building was ventilated. The SODAR worked almost continuously between February 9 and June 30 of the 2003 campaign. The next summer the SODAR was restarted at the beginning of the season and ran between November 18 and November 30 before being sent back to the factory for maintenance. The following season it ran between February 1 and May 3 2004. All together we gathered a total of 226 days of data. Preliminary results using only the 2003 data can be found in Travouillon et al. (2003).

Table 5.4: Summary of the turbulence and wind correlations.

Relationship (y,x)	R	Regression line y=ax+b	
		a	b
Horizontal wind speed and turbulence. [1]	0.91 $(m^{5/3}/s)$	6.15 (m/s)	-148
Positive, vertical wind speed range and turbulence range [2]	0.92	1.14	56 (m)
Mixing height and wind inversion size. [3]	0.89	0.53	410 (m)

R is the correlation coefficient between the two parameters. A and B are the linear regression terms. In (1), The average turbulence and average wind speed were used. The correlation was calculated using points of same altitudes and is shown in figure 5. In (2), the height of the boundary layer was compared to the size of the positive vertical speed range for individual set of data. In (3), monthly averages of the mixing height and wind inversion size were compared and shown in figure 12.

5.4.1 Long and short scale temporal variations

The behaviour of the boundary layer turbulence at Dome C is significantly different from the South Pole. Dome C is at a latitude of 75° and unlike the South Pole is subject to diurnal variations. On a 24 hour time scale the change in the sun elevation at the South Pole is negligible and no noticeable change in the turbulence profiles was found on this time scale. At Dome C the sun elevation varies enough to affect the behaviour of the boundary layer turbulence. While daytime turbulence is of no interest to stellar astronomers it remains important to understand and quantify the level of turbulence present near the ground for days with partial nights. Similarly to temperate sites where the nighttime thermal cooling of the ground creates a significant amount of surface layer turbulence, Dome C is subject to thermal cycles until the sun has completely set in April. The SODAR results confirm this trend. Fig 5.23 shows the evolution of the boundary turbulence between February 9 and 18, 2003. The daily cycle is clearly visible and follows accurately the variations of the sun zenith angle. In the middle of the day and the sun is high the turbulence extends up to 200 m in height and becomes convective. When the sun elevation decreases, the surface heat flux also decreases and

the boundary layer lowers accordingly. This behaviour is common to all sites apart from the Poles where no 24 hour cycle exists.
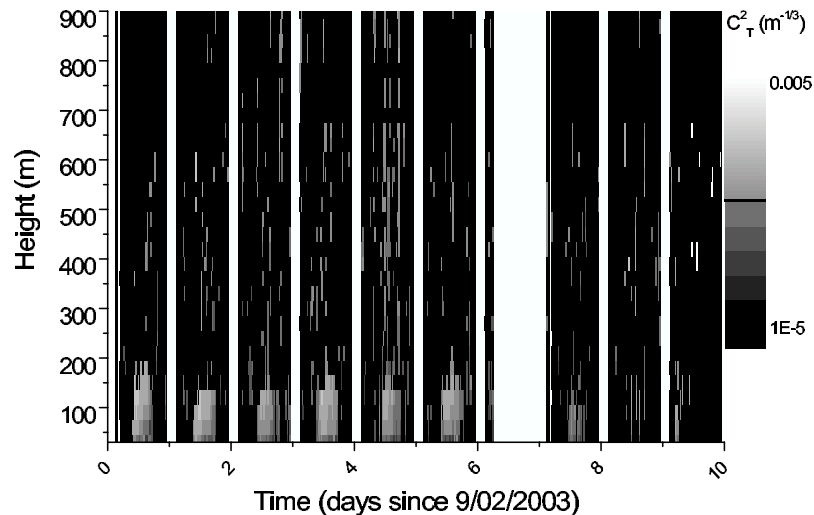
Figure 5.23: Grey-scale intensity diagram of the turbulence at Dome C for a period of 10 days still subject to diurnal cycles. The grey-scale level indicates the intensity of the turbulence. The y-axis indicates the altitude above the ground.

When the sun elevation is low enough, the boundary layer drops below the SODAR range of 30 m. This characteristic is advantageous to astronomy as the contribution of this part of the atmosphere can be neglected for large observatories. Other SODAR measurements taken at Dome C by Mastrantonio et al. (1999) confirm our results. Using a mini-SODAR sensitive down to 10 m they were able to observe the turbulence layer drop between 20 and 30 m in January 1997. Above 30 m, no turbulence layer is systematically present and a majority of profiles fall below the detection threshold. Random turbulence patches still appear on the data but none remain visible long enough to be qualified of "layer". This general behaviour is representative of the winter period as it is shown in Fig 5.24. While the absence of turbulence layer between 30 and 890 m is advantageous to astronomy, it becomes difficult for the SODAR to give quantitative results. As the detection threshold is often reached, only an upper value of the seeing contribution from this part of the atmosphere can be calculated. In 2003 and 2004 daytime cycles disappeared completely by the middle of February.

By then, the sun elevation never exceeded 27° and consequently the surface heat flux was not enough to create convection in the boundary layer. While no data is available at sunrise, the data taken between November 19 and 30, 2003 shows the 24 hour convection cycles returning. By this date the sun elevation reaches 34° and a boundary layer was visible in the middle of the day similar to the data obtained in February.
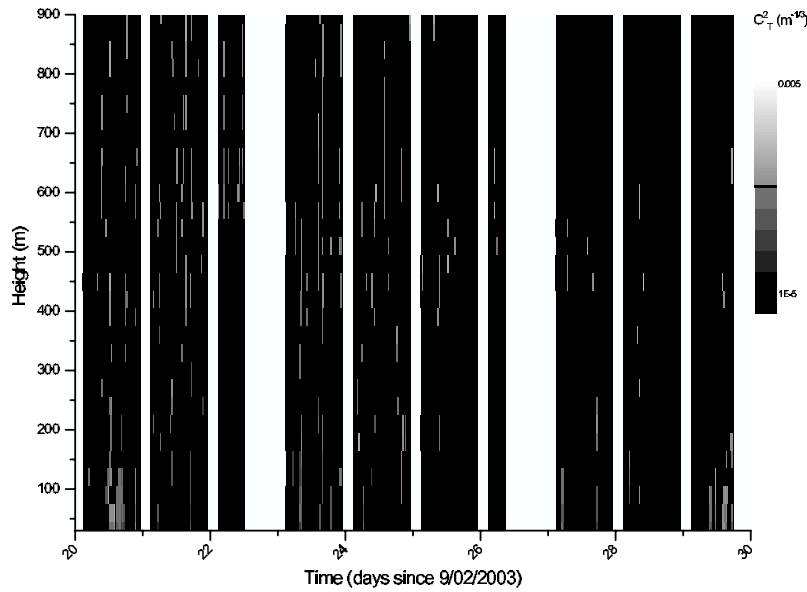
Figure 5.24: Characteristic intensity diagram of the turbulence in winter at Dome C.

The variation of the vertical distribution of the turbulence in the boundary layer of Dome C can also be witnessed in temperature profiles obtained in summer 2004 using the weather sondes. In order to carefully measure the evolution of the temperature profile in a 24 hour cycle, a series of 12 balloons were launched at 2 hour intervals. Since turbulence requires a temperature gradient to form, the data would provide a confirmation of the SODAR data. Indeed, the temperature profiles shown in Fig 5.25 give a good representation of the surface layer behaviour. During the day the temperature at the ground is higher than the air straight above it and convection is produced. As the sun elevation decreases the ground temperature cools and an inversion settles in the first 30 m of the atmosphere. This inversion is characterised by a large temperature gradient yet the SODAR is unable to

measure it because of the range limitation. Then the sun elevation rises and the inversion is shifted to a higher altitude as the ground temperature increases. When this happens turbulence becomes visible to the SODAR and remains so when the temperature inversion has fully disappeared and convection occurs.

At nighttime, the SODAR results suggest that the turbulence conditions in the boundary layer are similar to the one in the evening of the daytime period. Fig 5.25 shows that the inversion is fully developed between 8 and 10 pm and most closely resembles the wintertime conditions when the inversion is continuously present. It is therefore not surprising to find that the winter SODAR lacks a stable layer of turbulence similarly to the summer evening data. It must be stressed that while the turbulence between 30 and 900 m is very low we must still expect an active layer below this range where the temperature inversion is present.
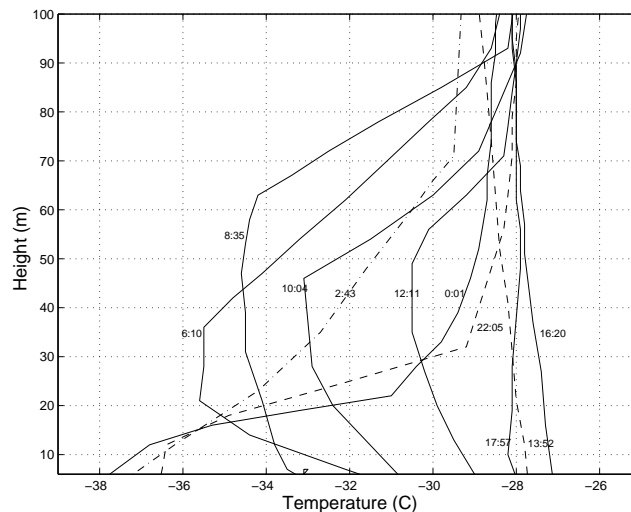
Figure 5.25: Temperature profiles of the first 100 m of the atmosphere taken at 2 hour intervals. No data was successfully recorded in this range by the sondes launched at 4:00 and 20:00 (Aristidi et al. (2005)).

5.4.2   Boundary layer seeing

Similarly to the South Pole we can calculate the boundary layer contribution to the seeing using the SODAR data. As the turbulence intensity falls below the detection threshold of the SODAR for a majority of the data,

the seeing must be taken as an upper value. Also we must differentiate the nighttime seeing since it is the only period of interest to astronomy. As it is the case at any site, in the daytime, the convection produces turbulence in the boundary layer that is not present at night. In order to make a proper comparison of the Dome C boundary layer with other sites we must therefore restrict our analysis to the nighttime. The results of this analysis which use the nighttime data of both 2003 and 2004 are summarised in table 5.5 and compared with the South Pole. The difference between the two sites boundary layer turbulence is striking. With a median seeing 40 times lower than the South Pole, Dome C low altitude atmosphere is extremely stable and its contribution to the overall seeing minimum. This fundamental difference between the two sites is solely due to their respective locations. As illustrated in Fig 5.26, the temperature inversion which causes the katabatic wind on the Antarctic plateau increases in size as the slope of the ice increases. Dome C, located on a local maximum of the plateau, is therefore expected to have the smallest inversion layer in Antarctica with the exception of Dome A which is the highest point on the plateau. Above this inversion the temperature profile is very stable and little turbulence activity is measured by the SODAR.

Table 5.5: Summary of the boundary layer contribution to the seeing.

	Mean	Med.	25%	75%	Min	Max
Dome C	0.071	0.049	0.048	0.142	0.033	0.490
South Pole	1.73	1.59	1.17	2.17	0.033	8.38

The issue of the inversion which cannot be sensed by the SODAR still needs to be resolved since it may contain a significant amount of turbulence and therefore affect astronomical projects of small structural size. In the following chapter we will discuss the surface layer turbulence of Dome C and estimate its contribution using other instruments available to us in 2004. At the South Pole, the surface layer turbulence is well known as it was the subject of a study by Marks et al. (1996).
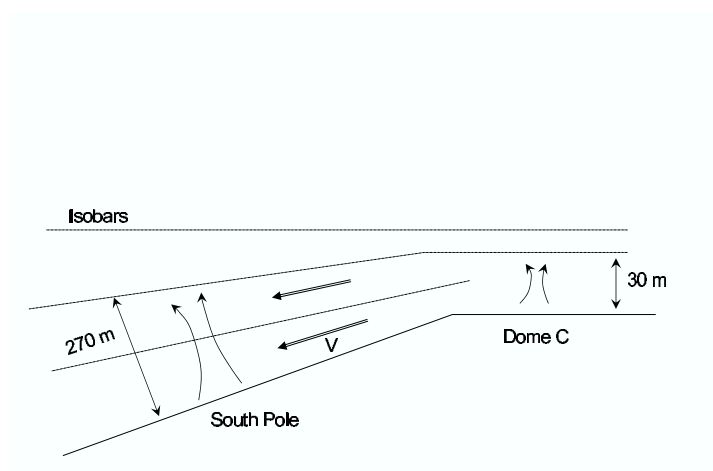
Figure 5.26: Schematic of the boundary layer evolution as a function of slope.

Chapter 6

Integrated Seeing

6.1 South Pole Campaign 2001-2002

The results in this section have been published in Travouillon et al. (2003a).

As part of a site testing campaign in Antarctica, the Joint Australian Centre for Astrophysical Research in Antarctica (JACARA) has deployed a seeing monitor at the South Pole station. While the median seeing of the site has already been determined using C_N^2 profiles (Marks et al. (1999), Marks et al. (1996) and Travouillon et al. (2003b)), a direct measurement of the seeing had previously only been carried out for a limited period of time in 1996 using a DIMM (Bally et al. (1996) and Loewenstein et al. (1998)). It was found that the South Pole has a poor average seeing ($1.7''$). On the other hand, the turbulence distribution of the site is very advantageous. The entire turbulence is located within a low altitude boundary layer about 300 m high and the jet stream is totally absent. For this reason, the South Pole has the best recorded isoplanatic angle and coherence time (Travouillon et al. (2003b)).

In order to extend our knowledge of the statistical behaviour of the seeing condition at the South Pole during the whole winter season, the A-DIMM (Automated Differential Image Motion Monitor) was especially engineered to work totally unmanned in the cold Antarctic conditions, measuring the seeing in a semi-continuous manner through out a whole winter. The A-DIMM is a Shack-Hartmann wavefront sensor which uses a microlens array to split the light entering the telescope and form a series of images spanning the whole aperture. This technique is very commonly used in adaptive optics

to assess the wavefront abberation and feed it to the deformable mirror. For our site testing purposes, the A-DIMM acts as an improved DIMM that uses an array of 24 sub-apertures instead of the standard double apertures and therefore obtains multiple measurements of the same seeing.

6.1.1   System description

Like all of the other AASTO site testing experiments, the A-DIMM was designed and built with three essential requirements: The telescope must be able to endure temperatures as low as $-80°C$ and must sustain large temperature changes without losing its optical properties. It must also run in a complete autonomous to compensate for the lack of personnel in the Antarctic sites and allow for remote operation via satellite.

The A-DIMM (Dopita et al. (1996)) was built around the optics of a Celestron C14 ($\sim$35 cm). The tube of the telescope was replaced by an Invar structure in order to match the coefficient of expansion of the Pyrex mirrors. This allowed the A-DIMM to retain its focus between the commissioning in Australia at $+20°C$ and the installation at the South Pole at $-30°C$. All corners are flattened to prevent ice build up and the telescope can regularly park itself into heated cups to melt the ice that could have formed on the lens.

The automated Cassegrain instrument is capable of centering a star by reflecting the light with a pierced mirror to a finder CCD camera. The information on the star position is used to offset the telescope in order to let the light through the pierced hole of the mirror onto the Shack-Hartmann optics. This technique is used to automatically centre the chosen star taken from a pre-selected catalogue. The catalogue consists of 48 stars with luminosity brighter than 3 and evenly distributed across the sky. The script used for the data analysed in this paper runs for 10 hours. It starts observing the first star on the catalogue and will continue for 30 minutes unless the star cannot be found (because of a cloud for example). In either case, it will then move on to the second star in the script and will continue this operation until the script time is up. This allows us to maximise the observation time in case of scattered cloud obstructing parts of the sky without help of a human intervention. Once the star is detected and centered, the light is collimated to form a pupil on the surface of a microlens array. Each square lens (0.188 mm in sides), forms a separate image of the target star on the CCD detector
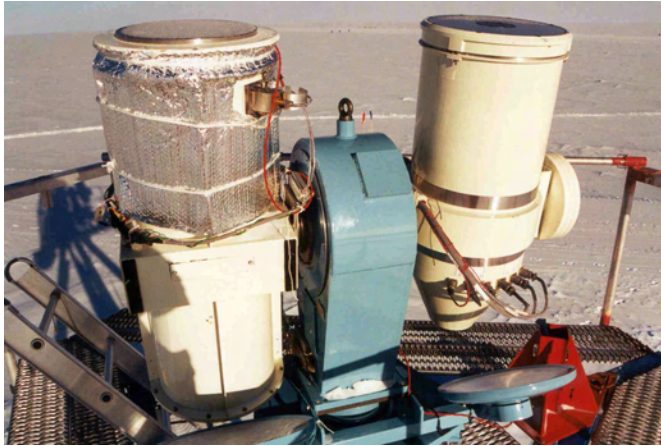
Figure 6.1: A-DIMM (right) installed at the South Pole on the G-mount.

corresponding to an effective 64 mm square onto the sky which was chosen to be much smaller than the expected Fried parameter (Travouillon et al. (2003b) and Marks et al. (1999)) in the spectral range of the telescope. The A-DIMM freezes the seeing with exposure times of 10 ms on a CCD detector with a scale of 1.09(H) x 1.26(V) arc sec/pixel. With this technique, the A-DIMM obtains 24 images coming from the corresponding sub-apertures, making a total of 215 separate baselines satisfying the condition $(d > 2D)$ described in the theory. Sub-pixel centroiding is then used on each individual image in order to determine their respective distances. The accuracy of this method will be discussed in the next section. Once the information of the coordinates and amplitude of each image is compressed and stored, the DIMM discards the image and repeat the observation at a rate of one image every five seconds. While the frequency of the measurements is low compared to other DIMMs, the large number of baselines strongly improves the statistics.

The A-DIMM was installed at the South Pole station in the summer 1999. The telescope is driven by the G-Mount, an Alt/AZ mount supporting two telescopes. The G-mount can be programmed to schedule the observation of the two telescopes installed. In 2000, the A-DIMM was installed beside the AFOS (Automated Fibre Optic Spectrometer), but technical problems with the AFOS allowed 100% of the observation time to be spent with the A-DIMM during that year. The overall assembly is showed in figure 6.2. Finally, the G-mount was installed on top on a 7.5m high hexa-
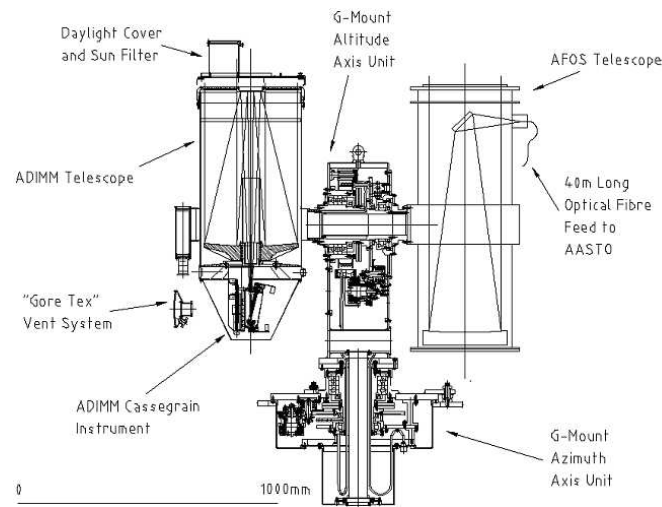
Figure 6.2: Cross section through the G-mount assembly with the A-DIMM and AFOS telescopes.

pod tower which retains its parallelism with the ground under any wind situation.

6.1.2   Data processing

The data is preliminarily processed by the A-DIMM itself as the bandwidth available to send the data outside the Antarctic is limited. The DIMM's software calculates the centre of mass of each of the 24 sub-aperture images that forms within a 9 pixel square. The centroid coordinates and fluxes are recorded and compressed before the image is discarded. Every 5 seconds such an image is taken and the resulting information (using 322 bytes of disk space) is appended to the daily file.

The differential image motion is calculated by measuring the variance of the distance between two sub-aperture images. As seen in section 2, each baseline gives 2 estimates of the seeing. Every 5 seconds, the 215 baselines therefore measure 430 separate distances. The variance is then calculated over 25 successive measurements. This number was chosen to be as large as possible yet within the time range where the atmosphere retains its statistical properties. The error analysis and the statistical treatment of the data are now reviewed in detail.

Instrumental noise

The differential nature of DIMM means that the measurements are unaffected by vibrations of the telescope and tracking errors. This characteristic is an advantage as it removes most sources of errors. However, as described in Sarazin and Roddier (1990) and Tokovinin (2002), subtle effects must be taken in account to remove potential bias in the measurement of the seeing.

The first source of bias is the accuracy of the centroiding. Under a zero turbulence condition, the centroid position will vary due to photon noise and aberation error. This instrumental noise will appear as a variance σ_{inst}^2 which will be assumed to be systematic and isotropic. The instrumental variance must be subtracted out from the total measured variance in order to obtain the turbulence generated variance:

$$\sigma_{tur}^2 = \sigma_{meas}^2 - \sigma_{inst}^2 \tag{6.1}$$

The instrumental noise was evaluated with the observation of the binary star system Alpha Centauri. Since the seeing has been taken out by the short exposure, the change of distance between the two stars within a sub-aperture can only be due to the instrumental noise. The distance between the two stars within each sub-aperture was calculated using the same algorithm as used for the centroiding. The variance of this distance was then computed and averaged using all 24 apertures. Under these conditions, we found that:

$$\sigma_{inst} = 0.074'' \pm 0.0008 \tag{6.2}$$

This value is expected to remain the same as all the observed stars have been chosen with an acceptable photon noise level. In poor seeing conditions, the apparition of speckles and scintillation can increase the centroiding noise. This effect will however be small compared to the standard deviation derived from the seeing measurements from all the baselines.

Statistical errors

For a standard, single baseline DIMM, the variance obtained from N images includes a statistical error as described by Sarazin and Roddier (1990):

$$\frac{\delta\sigma^2}{\sigma^2} = \sqrt{\frac{2}{N-1}} \tag{6.3}$$

In a case of multiple baseline measurements, the statistical error is simply represented by the standard deviation coming from the independent calculation of the seeing by each individual baseline. The use of this technique also implies that each seeing measurement will carry an individual error instead of a constant percentage error for the single baseline DIMMs. This error is particularly noticeable for large seeing values ($> 2''$) where the formation of speckles renders the centroiding less accurate and overestimates the seeing. The average error found with the A-DIMM at the South Pole is 17%, a value larger than the typical single aperture DIMM ($\approx 10\%$). This can be explained by the larger seeing values measured at the South Pole station as it will be shown in the next section.

6.1.3   Results

Table 6.1: Statistical results of the South Pole seeing as measured by the A-DIMM in 2001 at 500 nm. It is compared to other seeing measurements from the South Pole. All figures are in arcseconds.

Instrument	♯ days	Mean	Std. Dev.	Med.	25%	Best	Worst
A-DIMM	101	1.90	0.60	1.82	1.43	0.46	3.72
SODAR	269	1.73	1.07	1.59	1.17	-	8.11
Microthermals	16	1.86	0.75	1.6	1.0	0.8	3.1
H-DIMM	28	1.53	-	1.64	-	0.6	6.2

The data presented here provides extensive coverage of the seeing conditions at the South Pole station. Spanning the major part of the winter night, between the 28/05/2001 to the 6/09/2001, 588 individual measurements have been made. The statical summary of the results is presented in table 6.1 and is compared to other existing datafrom the site.

The A-DIMM measurements confirm the known seeing behaviour of the site. While the turbulence is known to be concentrated in an advantageous boundary layer, the resulting ground seeing is of poor quality. The $1.9''$ FWHM average at 500 nm is unsatisfactory for most visible and infra-red observations. The seeing drops below $1''$ for only 10% of the time and never for an extended period of time. It can be noted that the A-DIMM shows more pessimistic values than the H-DIMM or the microthermals. This can

be explained by the autonomous nature of its operation. The H-DIMM and microthermals data were taken manually and therefore do not include more extreme conditions. In such conditions (strong wind, hazy sky) the A-DIMM continues to take data although they are likely representative of bad seeing. Figure 6.3 shows the seeing distribution.
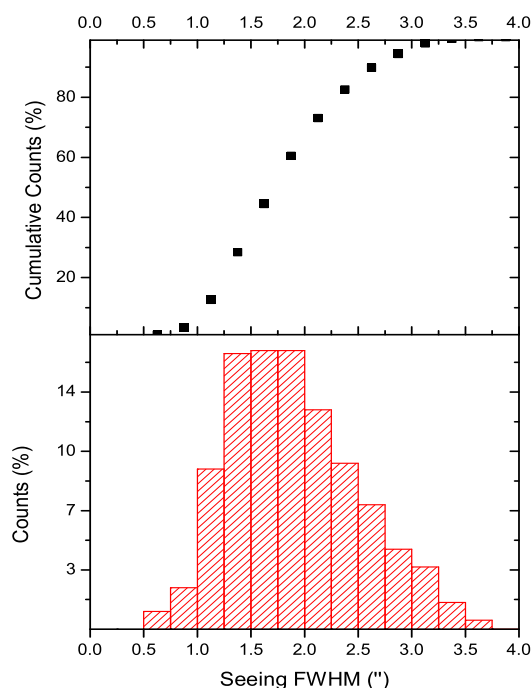
Figure 6.3: Simple and cumulative seeing distribution at 500 nm.

The statistical distribution of the A-DIMM is in excellent agreement with the H-DIMM (Loewenstein et al. (1998)) seeing probability. The only noticeable difference between the two data sets comes from the worst seeing measured. The A-DIMM worst seeing is $3.72''$ while the H-DIMM recorded seeing as bad as $6.2''$. We believe that this difference comes from the lower sampling speed of the A-DIMM. Extremely high seeing values last for a very short period of time and can therefore be missed by the A-DIMM.

6.1.4 Temporal variations

Looking at the long-term fluctuations of the seeing (Figure 6.4), no conclusion can be made about a seasonal evolution of the seeing. The month of

July is the most stable as was also noticed the year before (200) in the SO-DAR measurements. The daily average seeing oscillates between $1.5''$ and $2''$ during this period while in June and August there are variations of up to $2''$ in a few days.
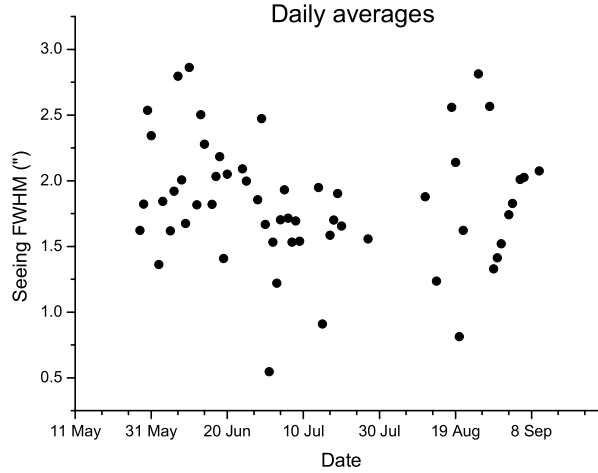
Figure 6.4: Entire data sample summarised in daily averages.

The short term temporal behaviour, which is illustrated by three typical days of observation, figure 6.5, figure 6.6 and figure 6.7, has never been studied at the South Pole. In fact, it has only been to our knowledge, the subject of two other papers. Vernin and Muñoz-Tuñón (1998) and Racine (1996) studied this characteristic respectively at the observatory of the Roque de los Muchachos and at Mauna Kea. The scientific motivation behind this information is the management of of the observatory schedules. Many observatories now offer a queue scheduling which prioritises certain science projects for windows of particularly good seeing. The size of these windows and the level of variations are therefore other figures of merit that can be associated to a site.

To allow direct comparison, we have followed the technique developed by Racine (1996). We introduce the temporal structure function which measures the fractional change of the seeing over a time period Δt:

$$f(\Delta t) = \frac{|\varepsilon(t + \Delta t) - \varepsilon(t)|}{\varepsilon(t + \Delta t) + \varepsilon(t)} \tag{6.4}$$

This expression is related to the seeing ratio over an interval time t by:

$$X(\Delta t) = [\frac{\varepsilon(t + \Delta t)}{\varepsilon(t)}]^{sign(\varepsilon(t+\Delta t)-\varepsilon(t))} = \frac{1 + f(\Delta t)}{1 - f(\Delta t)} \qquad (6.5)$$

Provided that the seeing distribution is log-normal, this expression should saturate at $< f(\infty) >$ within a characteristic time τ and at a growth rate γ. The temporal structure function can be represented by the relation:

$$< f(\Delta t) >=< f(\infty) > \cdot [1 - exp(-\Delta t/\tau)\gamma] \qquad (6.6)$$
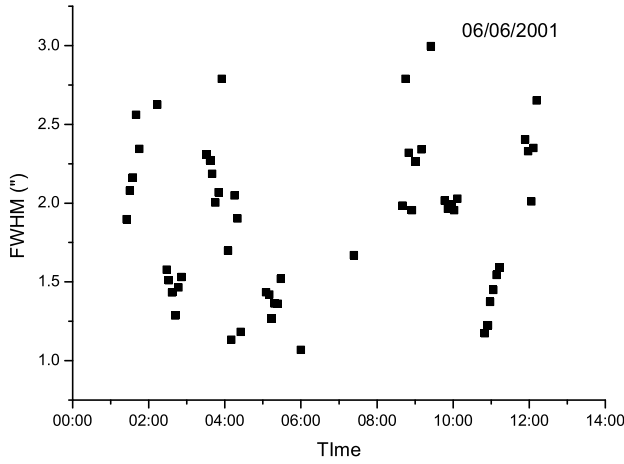
Figure 6.5: Seeing data from the 6th of June 2001.

We have chosen to estimate the average temporal structure function using the data of 5 days where the seeing was available continuously for 4 hours at intervals of 5 ± 1 minutes. Each string was analysed in a manner similar to Racine (1996) and then averaged. The data was finally fitted with Eq. 6.6 with χ^2 minimisation. The fitting (see Fig 6.8) yields:

$$\begin{cases} < f(\infty) >= 0.33 \pm 0.03; \\ \tau = 130 \pm 52 \text{ minutes}; \\ \gamma = 0.70 \pm 0.08. \end{cases}$$

These results show that the seeing dispersion saturates within between one and three hours to a seeing ratio $X(< f(\infty) >) = 1.96$. Racine (1996) observed a ratio of 1.56 in a characteristic time of 17 minutes at Mauna Kea. The South Pole seeing therefore varies more slowly but with larger
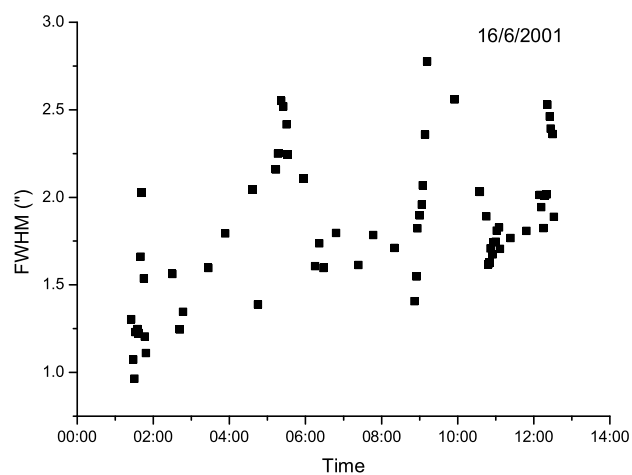
Figure 6.6: Seeing data of from the 16th of June 2001.
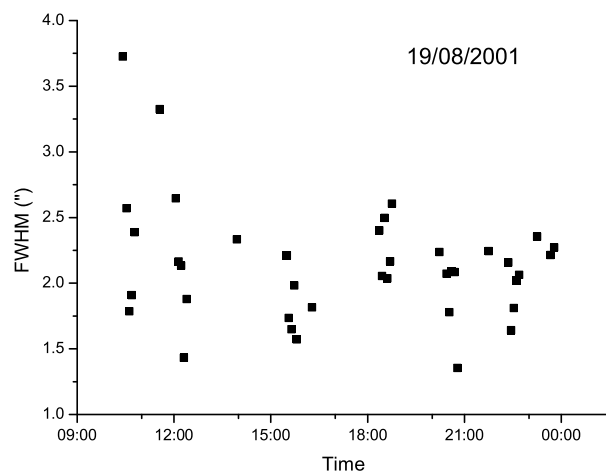
Figure 6.7: Seeing data from the 19th of August 2001.

amplitude. In fact the dispersion time at the South Pole is comparable to that observed by Vernin and Muñoz-Tuñón (1998) and analysed using a different mathematical approach at Roque de los Muchachos (1.2 hours), although the average seeing is of much better quality.

Fig. 6.8 shows a large noise of periodicity due to the small amount of data averaged. This residual appears to show periodicity, also present in the data of Racine (1996) and Vernin and Muñoz-Tuñón (1998) has been previously associated with gravity waves, as the period of their observations matches the period of seeing dispersion. As described previously, the South Pole seeing is produced by a boundary layer turbulence located 300 m high. The low level of high altitude turbulence is not sufficient to explain the periodic variations of the seeing at this site although they are still observed.
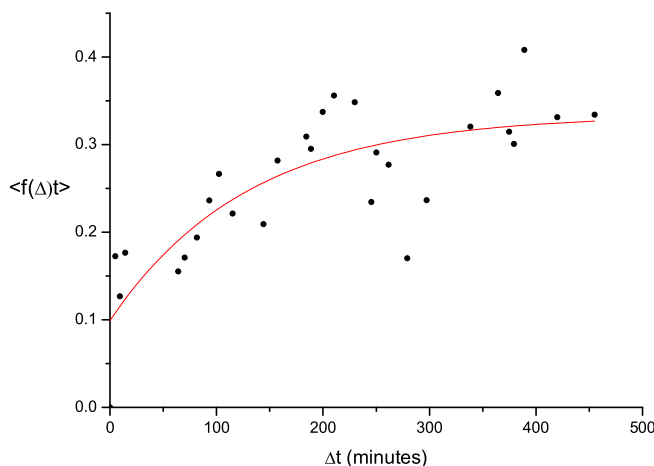
Figure 6.8: Average seeing dispersion as a function of time. The line follows Eq. 6.6, minimising χ^2

6.2 Dome C Campaign 2003-2004

6.2.1 Daytime DIMM results

The results in this section have been published in Aristidi et al. (2004) and Lawrence et al. (2004a). The author participated to these publication to the level of data acquisition and analysis as presented below.

During the Antarctic summer 2003-2004, DIMM measurements were made in a campaign led by the University of Nice. The instrument, designed around a Celestron 11 telescope uses a conventional two sub-aperture (6 cm diameter, 20 cm separation) format similar to the example described in Vernin and Munoz-Tunon (1995). The instrument was initially deployed and operated in 2002 (Aristidi et al. (2003), but the measurements were later contested due to probable internal turbulence inside the telescope due to differential heating of the tube. The following year, the telescope tube was replaced and an additional "torus" aperture was manufactured on site to make additional measurements of the isoplanatic angle (Aristidi et al. (2004)). Instantaneous seeing was obtained by extrapolating the data using a double exposure time of 5 and 10 ms.

The results presented below are daytime measurements made between late November 2003 and early February 2004 with a total of 17148 data points. At any given site, daytime seeing measurements are systematically higher than their respective nighttime because the solar radiation is partially reflected by the ground in the thermal infrared. This causes additional turbulence in the boundary layer and therefore worsen the seeing. Daytime measurements are however useful to solar astronomers and also give a ceiling value to what the nighttime conditions may be like.

The seeing results were found to be exceptional for daylight conditions. The median seeing was $0.54''$ with a minimum of $0.10''$. The statistical distribution of the data is represented in Fig 6.9. It can be noted that such distribution and mean value are typical of the nighttime conditions at the best temperate sites. The isoplanatic angle is also extremely wide. Using another telescope mask, 6328 measurements of the isoplanatic angle were obtained with a mean and median seeing of $6.8''$. This is far better than the average isoplanatic angle found at temperate sites, typically between $1''$ and $2''$. The wide angle is a good indication that the high altitude turbulence conditions are very good. Such a combination of seeing and isoplanatic angle is very encouraging for the prospect of using adaptive optics at Dome C. However, most of the interest in the site is in the nighttime conditions. The question is then: can we deduce some information about the nighttime turbulence conditions from the combined DIMM and SODAR measurements made in summer?

Figure 6.10 shows a representative time-series of the seeing taken during
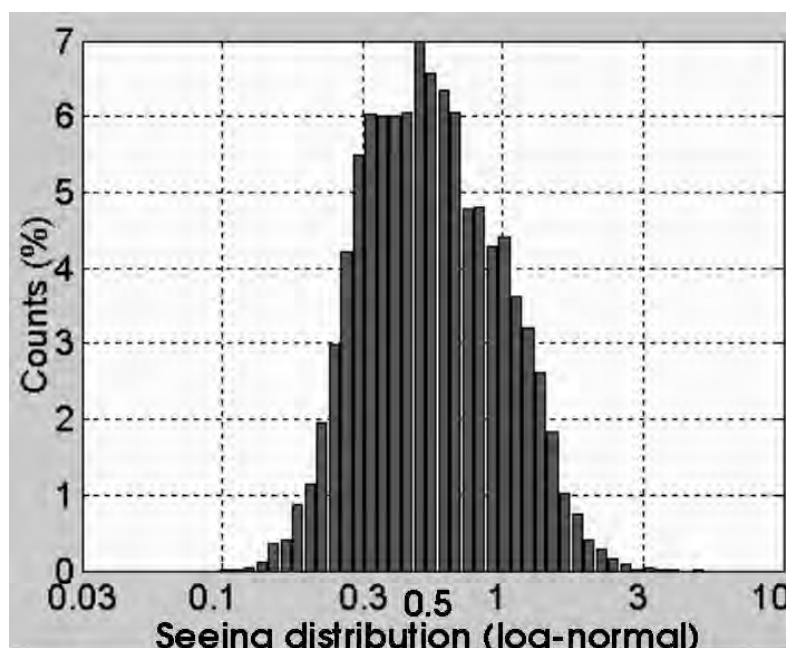
Figure 6.9: Distribution of the summer DIMM results. The mean seeing is
0.65″, the median 0.54″ with a standard deviation of 0.39″.

daytime. It shows that when the sun elevation is increasing (increasing
heat flux), the seeing conditions are unstable and oscillate between 0.5″ and
2″. In the afternoon the scatter in the data decreases and as the sun goes
down and a minimum is reached at around 17:00 with a seeing between
0.2″ and 0.4″. The seeing then finally increases again also increasing slowly
in scatter. It is important to point out that such time-series was observed
systematically everyday with the seeing reaching its minimum at the same
time of the day.

The explanation behind this behaviour can be found in the ground layer.
The ground layer inversion is where diurnal variations are the most obvi-
ous. In order to investigate this effect a series of continuous weather balloon
launches was made on January 26 2004. Due to hardware limitation, we
were able to make one balloon launch every two hours. In Fig 6.10 we show
the results of the temperature profiles for the first 100 m. Unfortunately two
balloons (04:00 and 20:00) didn't return data until the balloon had reached
the first kilometer due to a problem of synchronisation with the receiving
station. Nevertheless, the figure shows the behaviour of the temperature
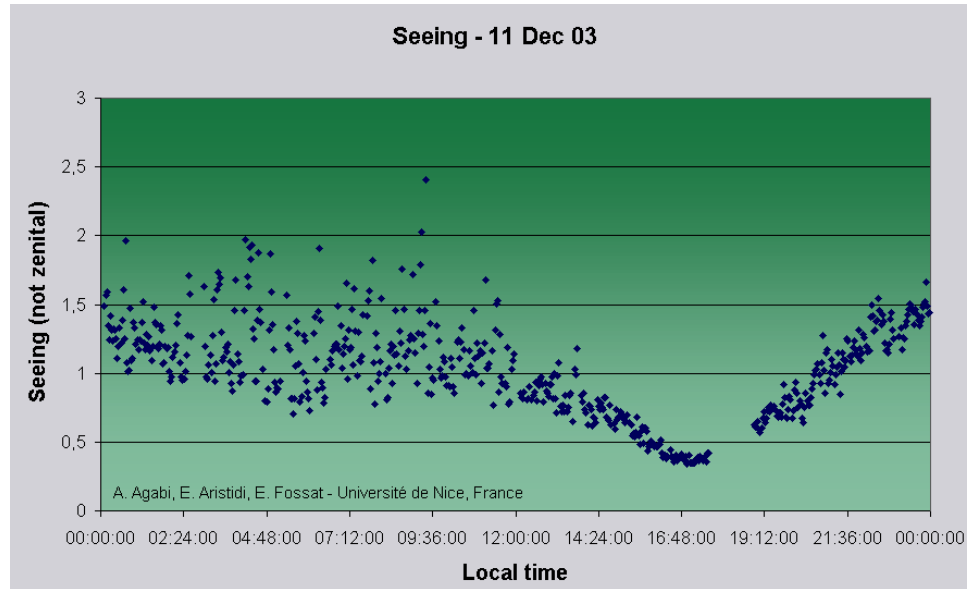
Figure 6.10: Example of the daily behaviour taken by the daytime seeing (Aristidi, *private communication*)

inversion as a function of time. In the middle of the afternoon, the temperature profile is flat. The ground and the surrounding air are in thermal equilibrium and no turbulence can be produced. This is apparent with in the DIMM data as the seeing continuously improves during the afternoon. Later in the day, the ground cools and the inversion sets in place (see 22:05 and 0:01 in Fig 6.11), with a large gradient in the first 30 m. At this point the seeing increases but remains stable as can be seen from the small scatter in the DIMM data. After midnight, the sun elevation increases again and the grounds heats up. Surprisingly, there is no symmetry between the cooling and the heating of the surface. When the ground cools, a very sharp gradient gets into place. The heating on the other hand "breaks" the inversion, extending it in altitude (see 6:10 and 8:35). At this point the seeing increases and loses coherence. This lack of symmetry is clearly visible in the SODAR data. As described in the previous chapter, turbulence in visible above 30 m between the early morning and the early afternoon. This is good agreement with the behaviour of ground thermal gradient and the DIMM data. From the three instruments, we can conclude that the daytime seeing can be classified into three regimes:
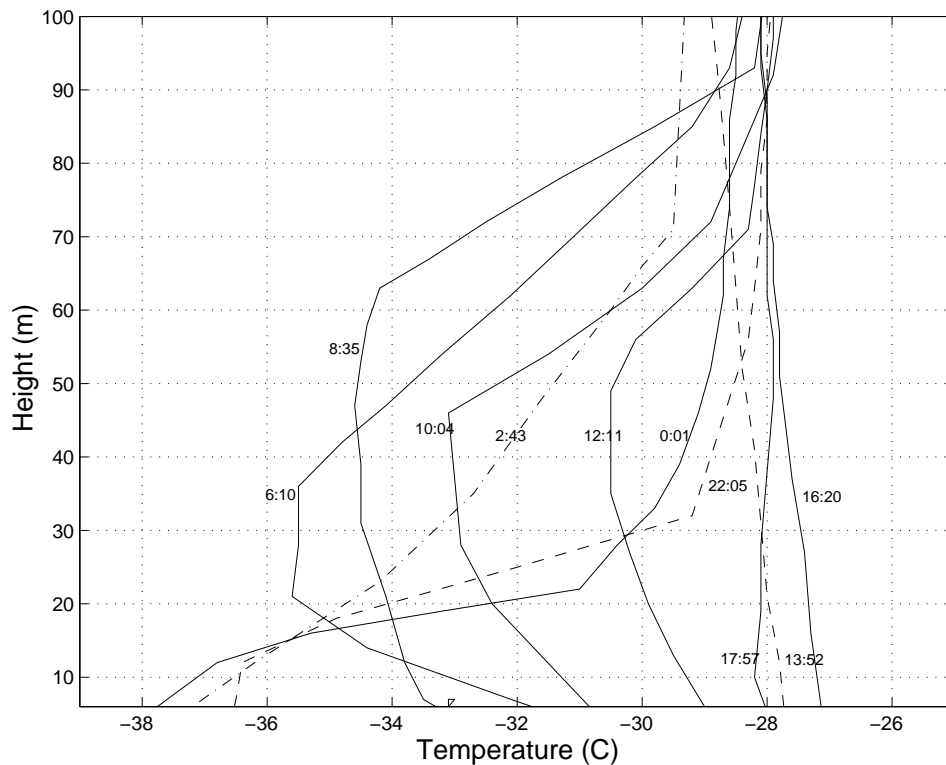
Figure 6.11: Temperature profiles taken in the ground layer at different time during the day on January 26 2004 (Aristidi et al. (2005)).

1. The middle afternoon presents a thermal equilibrium between the ground and the air. No ground layer turbulence is generated, the seeing is the best at this time.

2. The ground cools. A stable inversion is set and the ground layer seeing component worsens the seeing.

3. The ground warms up. The inversion is mixed by convection and the seeing worsens further, losing temporal coherence (typical of convective turbulence).

Since we are mainly interested in the nighttime seeing, one must wonder if any information can be inferred from the daytime DIMM data. As the answer lies in the temperature inversion, we must look at inversion data available at other, comparable sites. Such data is available from Vostok and can be found in Schwerdtfeger (1984). In summer, the temperature

inversion present at Vostok follows the same pattern than Dome C's but since Vostok is on a slope, the inversion extends to a higher altitude than Dome C. In winter the inversion remains stable and low until the diurnal cycles resume later in the year. This behaviour is also true for all inland stations in Antarctica while on the coast the inversion is only present in winter with a much smaller temperature gradient extended very high in altitude. The winter thermal inversion at Dome C is therefore expected to be defined by a very large temperature gradient as it is the case at 22:05 and 00:01 on Fig 6.10. This would confirm the discovery made with the SODAR data in winter that the turbulence, if any, is located below 30 m. However, the DIMM results show that this inversion degrades the seeing from $0.3''$ to $0.6''$. We must expect that below the SODAR range is located a non-negligible source of turbulence that could contribute up to $0.3''$ to the total seeing although because of the absence of solar radiation in winter this contribution should be lower. This theory needs to be validated in winter by turbulence measurements in the first 30 m of the atmosphere.

6.2.2 Preliminary MASS results

The summer 2003-2004 coincided also with the installation of a MASS (Multi Aperture Scintillation Sensor) in the AASTINO. Attached to an 8 cm refractive telescope, this version of the MASS was the first to be operated indoors. This decision was made because of the temperature rating of the MASS which was not suitable to the winter temperatures of Antarctica. The instrument looks through a glass window replacing one of the port holes on the building ceiling. The stars required for the observations are tracked with a siderostat that reflect the light into the telescope via a flat mirror. While strong turbulence is formed at the window boundary due to the large temperature difference between the inside and the outside, the MASS is completely insensitive to it (see Chapter 4.3).

The MASS worked successfully in its first winter and data was gathered almost continuously from early March to the end on May (Lawrence et al. (2004a)). C_N^2 profiles at 0.5, 2, 4, 8 and 16 km were used in addition to the SODAR profiles (from 30 to 500 m) to obtain seeing and isoplanatic angles. The results obtained are nothing short of spectacular with the lowest average seeing ever recorded on earth. The statistics are compared with other sites on Fig 6.12 and show that with a mean seeing of $0.27''$ Dome C offers the
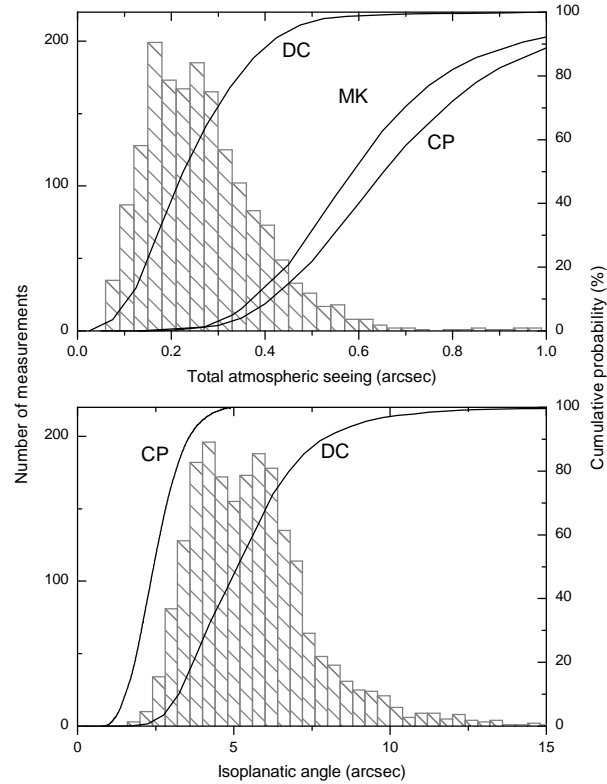
Figure 6.12: Statistics of the nighttime seeing and isoplanatic angle measured by the MASS in 2004 compared with Mauna Kea (MK) and Cerro Paranal (CP).

best conditions. The isoplanatic angle is also far superior at Dome C with a mean of $5.7''$ while most other sites do not exceed $2''$. This difference is explained by the absence of high altitude turbulence. The MASS profiles show no evidence of jets or turbulence related to the stratospheric vortex that creates high wind speeds at an altitude of 20 km. The strongest layer in the free atmosphere is at the tropopause (6 km) and confirms the prediction made using the Richardson criterion in Chapter 2.

It is interesting to note that the mean seeing found by the combination of the MASS and SODAR $(0.27'')$ instruments is in good agreement with the summer DIMM data taken at 5 pm when the temperature inversion disappears$(\simeq 0.3'')$. Indeed the SODAR is not sensitive to turbulence below

30 m and therefore does not measure the contribution of the ground layer shown to be bounded below this altitude. Our current measurements therefore correspond to the seeing a telescope placed above the inversion layer would see. To be able to make more conclusion about the free atmosphere of Dome C, further measurements are required. The last measurements made on May 5, are during the coreless winter but have not explored it with sufficient statistics. It is however clear from our knowledge of the stability of the winter conditions at the South Pole that the current data are a good indication of what is expected to be found all winter long and therefore that Dome C is the site with the best high angular resolution potential currently explored.

Chapter 7

Adaptive Optics Performance

7.1 General Considerations

Currently one of the fastest growing technologies in astronomy, Adaptive Optics (AO) aims at increasing the resolution of ground based telescopes by matching the shape of one, or several, deformable mirrors to the shape of the wavefront. This technology enables one to overcome the natural seeing and eventually reach the diffraction limit of the telescope. Of course, the level of improvement depends on the AO system itself but it also depends on the intensity and distribution of the turbulence in the atmosphere. As we have seen earlier, the South Pole is a site with a unique turbulence profile. Its high isoplanatic angle and long coherence time makes it a good candidate for AO despite the high integrated turbulence. At Dome C, the situation is even better since the atmosphere has the same qualities as the South Pole, but with a much less intense boundary layer turbulence. Performance estimates of a classical AO system (one deformable mirror conjugated to infinity) at the South Pole can be found in Lawrence (2003).

For tip-tilt (low order correction) or high order correction, the residual phase variance, which is one of the figures used to determine the quality of the correction, can be written as a series of several terms:

$$\sigma_{tilt}^2 = \sigma_{res}^2 + \sigma_{ta}^2 + \sigma_{snr}^2 + \sigma_{bw}^2 + \sigma_{ca}^2. \tag{7.1}$$

The first, third and fifth terms, respectively the tip-tilt residual, the signal-to-noise error and the centroid anisoplanatism are strongly dependent on the value of r_0 and are the largest source of phase error at a site like South Pole where the seeing is poor. However, the tip-tilt anisoplanatism error σ_{ta}^2 and the bandwidth error σ_{bw}^2 are small contributors to the total error in Antarctica where the high altitude turbulence and wind speed are low. Since Dome C matches all the above requirement, we can expect that AO will perform better there than at any other known site. In this chapter we will look into the details of another type of adaptive optics whose characteristics fits the turbulence conditions in Antarctica: Ground Layer Adaptive Optics.

7.2   Ground Layer Adaptive Optics

While most large telescopes are now equipped with adaptive optics systems (AO), their angle of correction is limited to a few arc seconds. The problem of anisoplanatism can be partly compensated by laser guide stars, however, for wide field correction the solution proposed is the conjugation of several deformable mirrors (DM) with the major turbulent layers. This technique, yet to be operational, will offer the resolution of the current AO systems over fields of a few arc minutes.

The drawback of multi-conjugate adaptive optics (MCAO), beside the complexity, is the cost. For some science programs, such as galaxy surveys, where the sources are extended and the diffraction limit is not essential for their conduct, an MCAO system is not justified. Rigaut (2001), therefore proposed a subset of MCAO, borrowing its concept of height conjugation but using and conjugating only one DM to the surface layer of the atmosphere. Wide field adaptive optics (WFAO), or ground layer adaptive optics (GLAO) as it will be referred in this paper, is capable of offering a significantly improved resolution over a large field of view. This technique is motivated by the knowledge that the surface layer is usually the most intense turbulence layer of all, as shown in Table 7.1. Conjugating near the ground also greatly improves the isoplanatic angle, which makes the correction of this layer valid over a large field.

The requirements of this type of AO call for a site with the largest proportion of turbulence in the atmospheric boundary layer, which must also be as low as possible. This characteristic is fulfilled at the South Pole. As

Table 7.1: Summary of the total and boundary layer (BL) seeing (ε) statistics at several major site. This table is adapted from Marks et al. (1999)

Site	Total ε (″)	BL ε (″)	% of ε in BL	BL height	Ref.
Mauna Kea, Hawaii	0.74	0.52	70	-	Roddier et al. (1990)
Cerro Paranal, Chile	0.73	0.55	75	2000	Murtagh and Sarazin (1993)
La Silla, Chile	0.97	0.85	87	800 - 1000	Murtagh and Sarazin (1993)
La Palma, Canary Is	0.96	0.73	76	1 - 2000	Vernin and Munoz-Tunon (1992)
South Pole	1.86	1.78	96	220	Marks et al. (1999)

shown in Table 7.1, 96% of the seeing is generated within a boundary layer 220 m high. The South Pole is located far from the latitudes where hot and cold air meet to create jets at the top of the troposphere. It is therefore free of high altitude turbulence. This peculiarity gives the South Pole a naturally high isoplanatic angle (Travouillon et al. (2003b) & Marks et al. (1999)). The boundary layer, however, is very active. Katabatic winds, originating from the top of the Antarctic plateau, create a convective layer with a large temperature gradient. This layer generates an average of $1.78''$ of seeing, making the site a poor candidate for high spatial resolution imaging. Despite this, it offers the best sky background of any ground based site between infrared and millimetre wavelengths (e.g. Peterson and Radford (2003) & Lawrence et al. (2002)). The atmospheric stability combined with the extremely cold temperature and water vapour absorption outweighs the disadvantage of the seeing limited spatial resolution for many types of observations. The design of an Antarctic GLAO system is therefore easily justified. Wide field surveys could, for example, be done faster at the South Pole than at any other ground based site.

7.2.1 The Simulation and GLAO principles

PAOLA (Jolissaint et al. (2003)) is an analytical, IDL based, simulation package that calculates the PSF of an aberrated wavefront after AO correction. In GLAO mode, PAOLA computes the residual phase power spectrum conjugating the deformable mirror at altitude h_c:

$$W_{GLAO}(f, h_c, \theta, \Omega) = k^2 \int_0^\infty W_N F_N^2(f, |z - h_c|, \theta, \Omega) dz. \qquad (7.2)$$

This residual is a function of the Von Karman refractive index power spectrum W_N, which depends on the intensity and distribution of the turbulence coefficient C_N^2 and outer-scale L_0:

$$W_N = (2\pi)^{-2/3} 0.033 C_N^2(z)(f^2 + 1/L_0^2)^{-11/6}. \qquad (7.3)$$

In this paper we will use C_N^2 profiles measured at the two sites for which details will be given in the next section. Since the outer scale of turbulence has not been physically measured we will base our results on a constant outer-scale of 30 m. The second important parameter of the residual phase

power spectrum is the refractive index transfer function F_N^2:

$$F_N^2(f,|z-h_c|,\theta,\Omega) = 1-2cos(2\pi f\cdot\theta|z-h_c|)g(f,|z-h_c|,\Omega)+g^2(f,|z-h_c|,\Omega)$$
$$(7.4)$$

The spatial filter $g(f,|z-h_c|,\Omega)$, describes the correction given to a particular layer. In PAOLA this correction is done by averaging the optical transfer function over a cone of angular size Ω. In this case the filter takes the form of an Airy function:

$$g(f,|z-h_c|,\Omega) = 2\frac{J_1(2\pi|z-h_c|tan(\Omega/2)f)}{2\pi|z-h_c|tan(\Omega/2)f} \qquad (7.5)$$

It can be noted that other authors have proposed different filters. For example, Tokovinin (2004b) proposed a Bessel function which is equivalent to averaging the transfer function over a ring while Rigaut (2001) suggested a sinc filter. Regardless of the type of filter chosen, they will only apply to spatial frequencies that the deformable mirror can correct, and depend on the actuator spacing d such that $f < 2/d$.

The GLAO system performance across a sky angle θ will be strongly dependent on the size of the cone used in the wavefront sensing. A large cone angle will produce a lower correction over a large part of the sky because of averaging. Conversely, a small cone angle will give a better estimate of the wavefront shape but only to a small angle. PAOLA takes into account other parameters of the AO system such as the fitting error, the wavefront sensor aliasing and noise, the control time lag and the anisoplanatism to give realistic performance results. The only assumption the software makes is that the wavefront is perfectly known over the cone surface. This means that the simulation results will be accurate if the system has a large number of laser guide stars or if enough natural guide stars are available within the cone angle.

In this chapter we will explore the performance of a GLAO system on a 2 m telescope operating in the I, J, H and K bands. We use a wavefront sensor integration time of 1 ms and a control loop time lag of 0.7 ms.

7.3   The South Pole Simulation

7.3.1   The C_N^2 profiles

In order to achieve realistic results of the performance of a GLAO system, we must use high spatial resolution profiles of turbulence and wind speed vectors. The high spatial resolution is important because, as shown by Vernin (2002), free atmospheric turbulence is formed in thin laminae often observed in pairs. A coarse sampling of the atmosphere, such as obtained with SCIDAR or MASS instruments, are sufficient for seeing or isoplanatic angle measurements but only approximate for GLAO simulations. We have therefore chosen to use C_N^2 and wind speed profiles obtained from balloon borne microthermal sensors. With a resolution of roughly 5 m, this is currently the finest profiling technique available.

Also important for the analysis is the issue of averaging. Can we use an average profile to determine the performance of a GLAO instrument? There are two arguments against this. The first one is closely related to the issue of spatial resolution. Turbulence peaks are typically two or three orders of magnitude above the background and only a few tens of meters thick. The process of averaging a set of microthermal profiles would therefore smooth out the C_N^2 peaks and increase the background. The topology of the average profile would therefore not correspond to one of a realistic atmosphere and create a misleading performance estimation of the AO system. The second argument comes from the importance of the isoplanatic angle. As we will show in the next section, the GLAO performance is strongly correlated to the seeing and isoplanatic angle. An average profile does not have an average isoplanatic angle. Fig 7.1 illustrates the average South Pole C_N^2 profile from 13 individual profiles. While its seeing angle corresponds to the average of all individually calculated seeing angles, the isoplanatic angle is overestimated in the average profile. Using it for the analysis would therefore bias the results towards better corrections.

In this chapter we will therefore focus on the analysis of typical profiles chosen for having both seeing and isoplanatic angles close to their respective averages. Being recognized as one of the best sites in the world, the microthermal data from Paranal (Sarazin (1995)) will provide a comparative benchmark for the performance of a GLAO system at the South Pole. Paranal clearly has a better seeing than the South Pole. However, the isopla-

natic angle of the South Pole is twice that of Paranal and can be explained by the lack of free atmosphere turbulence. This difference can be observed in Fig 7.2 which shows that the the South Pole boundary layer turbulence is more intense than at Paranal while the tropopause peaks of Paranal are non existent at the South Pole. The profiles of Fig 7.2 both have seeing and anisoplanatism values near the median of their respective sites. They will therefore be used in the analysis to represent the typical profiles of each site.
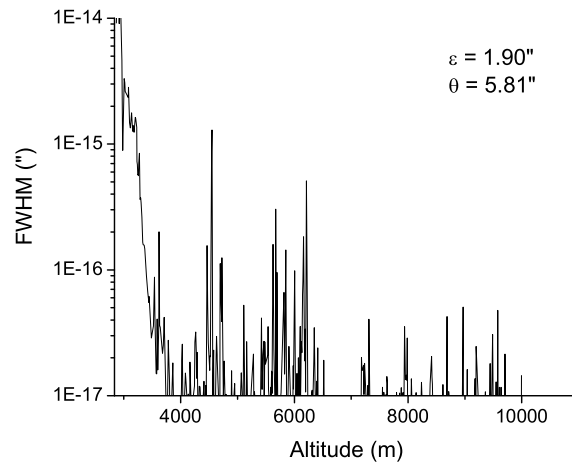
Figure 7.1: Average of the 13 South Pole C_N^2 profiles (From Marks et al. (1999)). ε is the seeing angle and θ the isoplanatic angle calculated from this profile. The ground level of the South Pole is at the altitude of 2835m.

7.3.2   South Pole Results and Discussion

In this section we will present the performance of a specific GLAO system on a 2 m telescope. This mirror size has been chosen as several IR telescopes of this size are currently proposed for Antarctica. The AO rectified long exposure PSF will be expressed in term of residual full width half-maximum (FWHM) in arc seconds to make easy comparison with the uncorrected seeing conditions.

Table 7.2 summarizes the characteristics of the GLAO system. We will look at the performance of the system as a function of corrected field (ie. the distance between the science object and the guide star) in I (880 nm), J (1.2
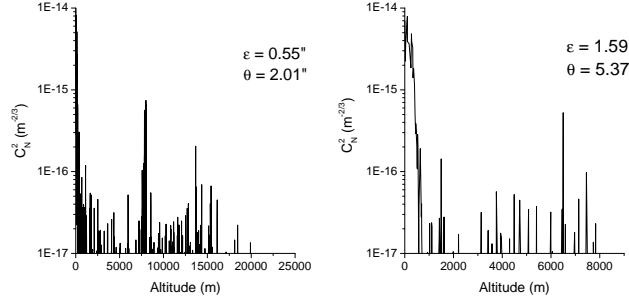
Figure 7.2: Typical C_N^2 profiles at the South Pole (right) and Cerro Paranal (left). The seeing ε and the isoplanatic angle θ are given in the diagram.

μm), H (1.65 μm) and K (2.2 μm) bands. The actuator pitch was chosen to be equal to the value of the Fried parameter in the I band and kept at this value for all the other bands in order to minimise the fitting error. While several turbulence and wind profiles will be used in this analysis, the outer scale of turbulence which is not experimentally measured will be assumed constant for all simulations and chosen to the commonly accepted value of 30 m.

Table 7.2: Summary of the parameters used in this analysis. The intrinsic parameters to the system are chosen to match the parameters chosen in Jolissaint et al. (2003) for the purpose of comparison. These parameters are consistent with existing systems.

Primary mirror diameter	2 m	AO loop time-lag	0.7 ms
Secondary mirror diameter	0.56 m	Outer scale	30 m
Actuator pitch	r_0 @ I band	Field of correction	$0'$ to $10'$
WFS integration time	1 ms	WFS cone size	$0'$ to $10'$

Before estimating the performance of this system, we need to consider the altitude of conjugation. As shown in Jolissaint et al. (2003), the optimal height of conjugation is not simply the ground. It is influenced by the overall distribution of the seeing in the atmosphere. This distribution is centered at a weighted altitude $\langle H \rangle = (\int h^{5/3} C_N^2(h) dh / \int C_N^2(h) dh)^{3/5}$. Sites with high altitude turbulence will therefore have an optimal conjugation shifted

toward this height. At the South Pole the majority of turbulence is so close to the ground that this effect is non-existent. Fig 7.3 Shows the value of the residual FWHM calculated from the typical profile as a function of height conjugation. We have found that the performance of the system decreases with increasing height conjugation, while it remains acceptable up to 400 m. It can be noted that $\langle H \rangle$ is low (lower than the top of the boundary layer) and indeed within the range of acceptable conjugation. In the rest of this paper the GLAO system studied will be conjugated to a height of 100 m at the South Pole and 120 m at Paranal.
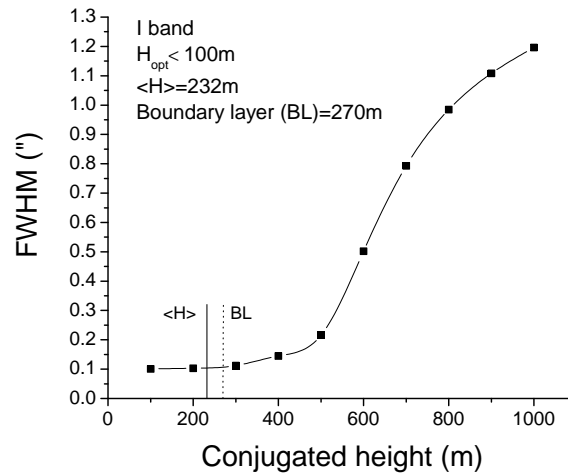
Figure 7.3: Comparison of the residual seeing as function of conjugation height using the typical South Pole profile.

The key result is the amount of residual seeing as a function of field size. In standard AO systems, the field size is restricted to the isoplanatic angle, that is an order of a few arc seconds. Beyond it, the correction quickly fades. In GLAO a much wider field of correction can be achieved, although the correction may not be as strong. In Fig 7.4 we show the results of this correction at the South Pole for WFS cones ranging from 1' to 29' using the typical turbulence profile. The system performance can therefore be estimated by the lower envelope of these curves. It shows that about 80% of the natural seeing can be eliminated in a field of 4' depending on the wavelength used. In the J, H and K bands the improvement is more

apparent. The best correction is obtained in the I band over a small field but it degrades more rapidly at wider field than it does for longer wavelengths.
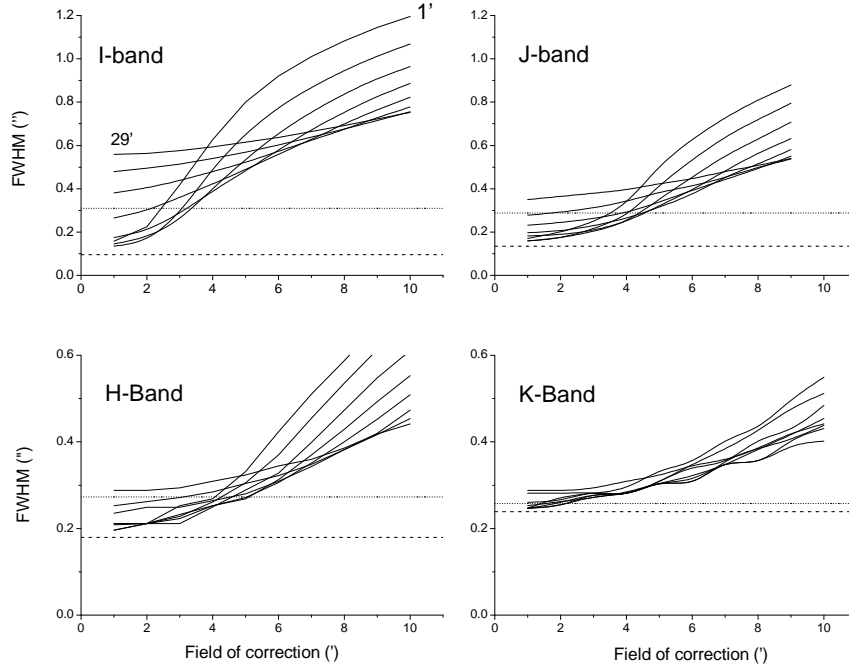
Figure 7.4: Residual FWHM as a function of corrected field for I, J, H and K bands for the South Pole typical profile. Each curve corresponds to a different cone angle from $1'$ to $29'$ with steps of $4'$. The upper line corresponds to 20% of the natural seeing and the bottom line to the diffraction limit.

The suitability of the site cannot be inferred from a single profile. We have therefore calculated the residual seeing using all the available microthermal profiles at the South Pole and Paranal. Due to the extraordinary long demand on computing power required, the two worst profiles at the South Pole have been excluded from the calculation. The comparison was carried out in the I band for fields of $1'$ and $10'$ using their respective optimal WFS cone angle. The results are expressed in Table 7.3 along with the original seeing at 500 nm and isoplanatic angle of each profile. While Paranal starts with a median natural seing much lower than the South Pole, we find that the corrected seeing of the two sites is comparable for both nar-

row and wide fields of view. This is an important result as the only weakness of the South Pole is its poor r_0. Equipped with a GLAO system, a telescope at the South Pole can achieve the same resolution than it can at Paranal while taking advantage of the superior sensitivity. It is interesting to note that at both sites, the results of the smaller field are far less variable than at the larger field. At $1'$ the residual seeing almost systematically reaches $0.15''$ while at 10' it can either reach this same value or exceed $1''$ in case of bad seeing and isoplanatic angle.

In order to further investigate the effect of the seeing and isoplanatic angle on the performance of our system, we show in Fig 7.5 and 7.6 the residual seeing of several representative profiles as a function of field size along with the average residual calculated using all profiles. As we expect, profiles with better isoplanatic angles produced better overall correction. However, it is the combination of both seeing and isoplanatic angle that drives the extent of this correction over larger fields. In nights of good seeing and isoplanatic angle, the GLAO system will therefore give excellent correction over a very wide field. In the case of the South Pole where the boundary layer turbulence dominates, it is the seeing angle that has large variations while the isoplanatic angle is always very good. The GLAO system will therefore give more consistent results for small angle corrections while the larger fields of view will see more variations. At Paranal, it is the opposite situation. The seeing is more stable while the isoplanatic angle changes more frequently. We have then more variation of the performance for small fields and less deterioration for wider fields.

To further explore the comparison of the South Pole with other sites, we have investigated the performance of the GLAO system on a 20 m telescope. Using the same GLAO properties, Jolissaint et al. shows their Figure 4, the performances of Mauna Kea, Cerro Tololo and Cerro Paranal using average profiles. In order to make a fair comparison, we have computed the I band performance of a 20 m telescope using the South Pole average profile and retaining the parameters of table 7.2. The results are displayed in Fig 7.7 Unlike Mauna Kea and Cerro Tololo where the performance drops sharply over the first $2'$ of field, the South Pole achieves a corrected seeing below $0.2''$ within a field of $3.5'$ and an impressive $0.05''$ in the first $2'$. If field size is the priority over the quality of the correction, Cerro Paranal is the best performer of the 4 sites with a residual seeing systematically below $0.3''$ over

Table 7.3: Turbulence characteristics of all profiles used in the analysis and the residual FWHM after GLAO correction for a corrected field of 1' and 10' at I band. The seeing (ε) and the isoplanatic angle (θ) are expressed in arc seconds at a wavelength of 500 nm.

Flight #	South Pole				Cerro Paranal			
	ε	θ	res. ε for 1'	res. ε for 10'	ε	θ	res. ε for 1'	res. ε for 10'
1	1.86	5.63	0.14	0.40	0.82	4.03	0.13	0.3
2	0.59	4.81	0.13	0.16	0.58	3.53	0.14	0.27
3	2.12	1.46	1.05	1.28	1.49	0.41	0.73	0.92
4	1.26	4.04	0.17	0.35	0.54	2.04	0.18	0.28
5	2.06	3.92	0.13	0.73	0.46	1.71	0.16	0.19
6	1.47	5.51	0.13	0.43	2.7	2.45	1.12	1.76
7	5.44	4.33	-	-	0.82	1.74	0.13	0.32
8	1.02	3.81	0.14	0.37	0.55	2.01	0.11	0.14
9	1.01	3.57	0.14	0.25	0.62	2.30	0.11	0.15
10	0.99	5.84	0.12	0.23	0.62	2.79	0.12	0.28
11	4.07	5.33	-	-	0.91	1.63	0.18	0.36
12	1.59	5.37	0.13	0.74	-	-	-	-
13	1.31	6.14	0.11	0.23	-	-	-	-
Mean	1.90	4.59	0.22	0.47	0.91	2.24	0.28	0.45
Median	1.59	5.33	0.13	0.37	0.62	2.04	0.14	0.28

a large 10' field.

Figure 7.5: Residual FWHM of several C_N^2 profiles obtained at the South Pole with different combinations of seeing angle and isoplanatic angles. The average correction was calculated using all 13 profiles and a WFS cone angle of 5'.

7.4   Dome C Simulation

7.4.1   The profiles

While the South Pole is well suited to the use of GLAO, it is of great interest to estimate the performance level that can be achieved at Dome C. It is true that the low altitude atmospheric turbulence is significantly reduced at this site and the relative gain cannot be expected to be as significant as the South Pole. However, the motivation to use GLAO at Dome C is two fold. First, our current knowledge of the Dome C turbulence profile is restricted to the atmosphere above the first 30 m. While this part of the atmosphere is not significant to large observatories where the primary mirror is likely to be placed above this level, it can be potentially crucial for smaller projects to have a method to remove this layer of turbulence. Also, the GLAO system may bring the seeing level low enough to open a new range of science requiring a specific resolution.

To quantify the correction that the same GLAO system can achieve at
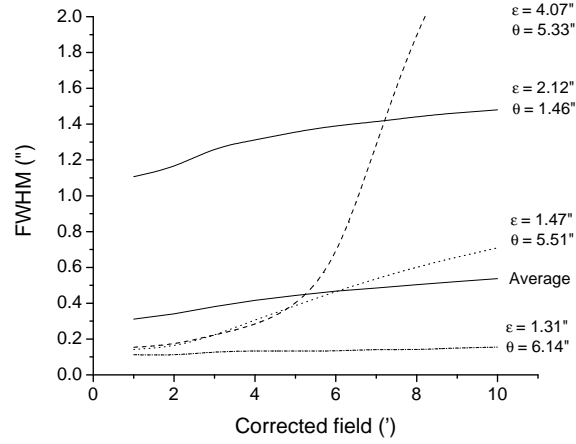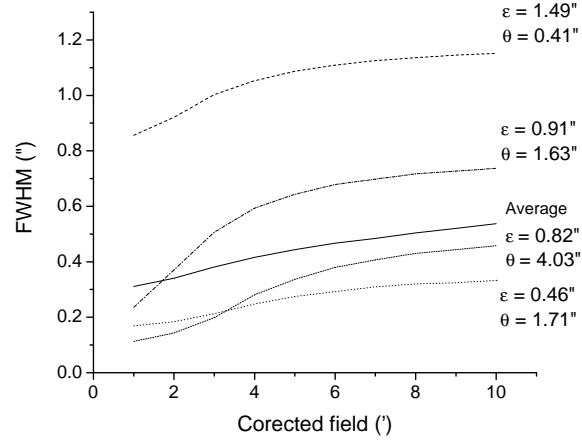
Figure 7.6: Residual FWHM of several C_N^2 profiles obtained at Paranal with different combinations of seeing angle and isoplanatic angles. The average correction was calculated using all 11 profiles and a WFS cone angle of 5'.
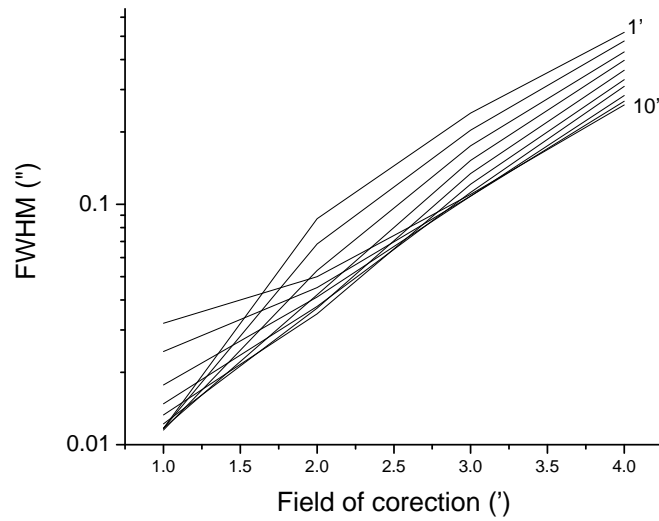

Figure 7.7: Performance estimates of a 20m class telescope at the South Pole in the I band for cone angles ranging from 1' to 10'

Dome C, we have run the same simulation on C_N^2 profiles obtained in the 2004 winter using rigourously the same hardware parameters. As no microthermal profile is yet available at Dome C. We use the turbulence data from the SODAR (30 to 500 m) and MASS (500 m to 22 km) obtained in the first half of the 2004 winter(Lawrence et al. (2004a)). The two instruments have worked simultaneously between the March 24 and May 3 of 2004 accumulating a total of 2670 combined profiles. The large amount of data available and its temporal continuity is very valuable as it gives us more reliable statistic of the performance of the system when compared to the South Pole simulations. As the SODAR temporal resolution is limited to one profile every 30 minutes, we have extrapolated the data to fit the temporal resolution of the MASS which can achieve up to one profile every two minutes. Since the MASS profiles start at 500 m, we only used the SODAR profiles up to that altitude.

7.4.2 Dome C Results and Discussion

The first consideration we need to make concerns the wavelength coverage where GLAO is beneficial. Since the seeing conditions at Dome C are very good it is easy to see that for a 2 m size telescope, the longer IR wavelengths will be diffraction limited. Indeed, we have found that at K band a 2 m telescope will be diffraction limited 89% of the time. At H and J bands, diffraction limit occurs commonly for 68 and 43% of the time respectively. It is only in the I band that diffraction limit becomes rare enough (17%) to require the use of GLAO. In the visible it is, however, essential for the telescope is never diffraction limited with natural seeing. We will therefore focus on the performance improvement brought in the V and I bands.

The simulation results in the V band are summarized in Table 7.4 and Fig 7.8. Because of the stability of the boundary layer we found that a high level of correction could be achieved for very wide fields of view. The correction as a function of field of view is illustrated in Fig 7.10 and 7.11 for V and I band respectively. On these graphs the performance is given for the best 25%, 50% and 75% C_N^2 profiles. We can see that the best 25% of the data in the I band bottoms out to diffraction limit resolution almost out to a 10′ field of view. In the V band however, the diffraction limit is still not reached even with the use of GLAO, although it gets close.

From here on, we quote the seeing correction for a field of 10′. As

expected, the improvement is not as great as it is at the South Pole. Since the natural seeing is already the best observed at a ground based site, removing the ground layer turbulence only lowers the median seeing by 35%. This gain is not enough to reach diffraction but it is still remarkable that $0.1''$ can be taken off the natural seeing over such a wide field.

Table 7.4: Statistical summary of GLAO performance at Dome C in the V band for a field of view of $10'$. The diffraction limit of a 2 m telescope at this wavelength is $0.05''$

	Mean	Median	25%	75%
Uncorrected seeing	0.28	0.27	0.18	0.34
Corrected seeing at $10'$	0.19	0.17	0.12	0.25
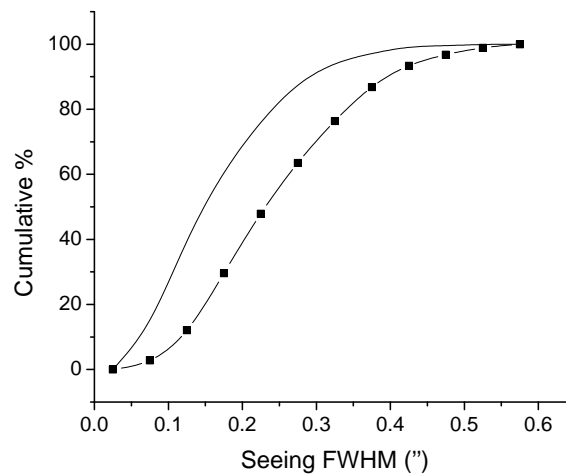
Figure 7.8: Cumulative distribution of the natural (dots) and corrected seeing (line) over a field of $10'$ in the V band at Dome C.

While the statistical results use all 2670 profiles, it is interesting to take a qualitative look at the temporal evolution of the GLAO performance. Fig 7.9 shows two time series of the natural and corrected seeing. The left-hand graph, corresponding to the data of April 1, shows that the level of correction brings the seeing almost systematically below $0.1''$. On this day, the free atmosphere was very stable and the variations of turbulence

in the boundary layer were well compensated by the system. On May 3 however the level of correction, shown on the right-hand graph, is more variable. The natural seeing, this time dominated by a turbulence layer in the troposphere, is poorer and oscillates rapidly between $0.1''$ and $0.4''$. In this type of conditions the corrected seeing is equally variable. The GLAO system is insensitive to the troposphere turbulence and while about $0.1''$ is still systematically removed the seeing variations are still large.
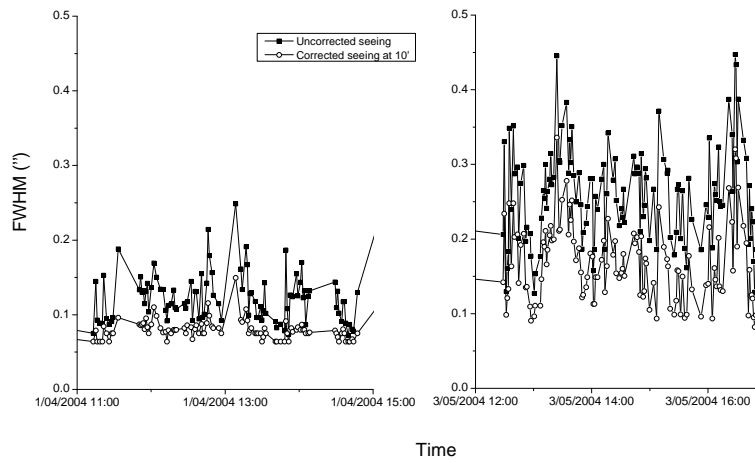
Figure 7.9: Time series of both natural and corrected seeing for April 1 and May 3, 2004 at Dome C.

Statements made earlier about the performance of GLAO in the V band also apply to the I band. An additional point however is the fact that at this wavelength the diffraction limit can be reached with a 2 m class telescope. While this is true in the natural seeing conditions for 17% of the time, GLAO can increase the total of diffraction limited time to 24% for $10'$ and 56% for $1'$ fields. At this stage is becomes obvious that GLAO would be vastly more beneficial to a larger telescope. For larger mirrors, the diffraction limit is lower and never reached by the natural seeing.

7.4.3   Simulation conclusions

We have demonstrated here that the South Pole is an excellent site for a GLAO system. It has relatively poor uncorrected seeing but the turbulence
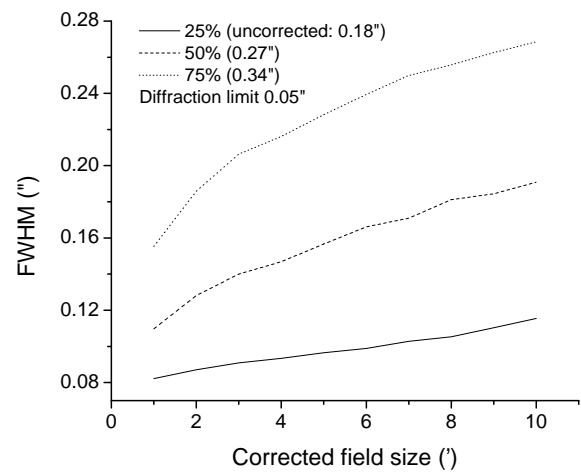
Figure 7.10: Corrected seeing as a function of field size for the best 25%, 50% and 75% profiles in the V band.
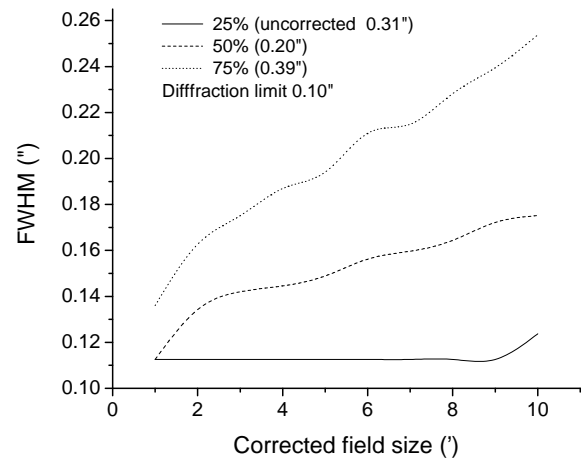
Figure 7.11: Corrected seeing as a function of field size for the best 25%, 50% and 75% profiles in the I band.

distribution in the atmosphere is unique in that its corrected seeing is better than the corrected seeing of other major observatory sites. The excellent sky transparency of the site has already been well exploited by several experiments in the sub-mm where the effect of turbulence is negligible. GLAO gives us the opportunity to develop the site in the near infrared. The combination of the low sky background with the high resolution over a wide field will make the South Pole a suitable place to conduct fast, wide-field surveys in the IR.

At Dome C, GLAO can be used to make the already excellent seeing even better. By reducing the natural seeing by $0.1''$ on average, GLAO makes a 2 m class telescope diffraction limited in the I band over a large field of view. While for such a telescope size GLAO is not necessary to achieve diffraction limit at longer wavelengths, one can see its necessity to push the performance of larger telescopes in the visible, a wavelength not normally considered achievable for AO systems.

Chapter 8

Conclusions

Starting from the principle that Antarctica offers the best conditions when it comes to infrared telescope sensitivity, the questions answered in this thesis are:

1. Can high angular resolution be achieved from Antarctica?

2. If so, can we relate the turbulence conditions to known meteorological and topographic parameters in order to generalise this knowledge to other parts of the continent?

3. What is unique about the turbulence conditions on the Antarctic plateau?

We have shown that the seeing conditions on the Antarctic plateau are strongly dependent on the ground wind conditions and the boundary layer is the section of the atmosphere that influences the seeing the most. Microthermal measurements at the South Pole and MASS profiles at Dome C have confirmed that the free atmosphere is highly stable as is expected from the presence of the polar vortex. However, SODAR measurements taken at the two sites showed that the contribution from the boundary layer can be very small in the case of Dome C or very large in the case of the South Pole. This variation can be explained and correlated with the thermal inversion and katabatic wind. At the South Pole, where the inversion is high and the wind speeds relatively high, the contribution of the boundary layer to the seeing is a high $1.7''$ while the free atmosphere is usually below $0.3''$. This level of turbulence is not suitable for high resolution imaging. In order to

improve the seeing, higher locations with the smallest slope must be selected. It is only at local maxima of the plateau that the inversion and winds will be low enough to decrease the contribution of the boundary layer.

Our SODAR measurements at Dome C have confirmed this theory with the boundary layer contributing only 0.1″ to the seeing. Compared with microthermal data from the South Pole, preliminary MASS results show also that the free atmosphere seeing is even lower than at the South Pole, although more statistics are needed to confirm this statement. We therefore have two sites that are mainly differentiated by the quality of their low-atmosphere turbulence conditions. With sky emission and absorption also improving as we reach higher points on the continent, it is expected that the ideal location on the Antarctic continent will be Dome A, the highest point on the plateau. Dome C, is however, the current best accessible site available.

More site qualification work is required at Dome C in order to appeal to a wide community of astronomers. It has been noticed at several sites that long term seeing variations occur and that seasonal effects are important. While the SODAR has shown that the boundary layer behaviour has been stable over two half-years, the MASS instrument must acquire more data from the free atmosphere to confirm the lack of turbulence above the tropopause. The stability of this region is critical to the size of isoplanatic angle and therefore of the use of adaptive optics at Dome C.

We must also quantify the turbulence in the first 30 m of the atmosphere. Our work has confirmed previous observations that the winter inversion is located below this altitude. Since the inversion is the cause much turbulence at the South Pole, we can also expect some turbulence at Dome C. An educated guess would be that it would be less intense at Dome C because of the lower wind speed, however it remains crucial to quantify the contribution of the first 30 m as well as its distribution and evolution.

The prospects for adaptive optics can also be inferred from our measurements. With current developments aiming to correct multiple layers of turbulence, the characteristics of the turbulence profile at South Pole and Dome C show that adaptive optics can perform very well at these sites. At the South Pole, the quasi-totality of the turbulence is located within the first 300 m of the atmosphere. Ground layer conjugated adaptive optics is therefore the best method to correct the aberration caused by the atmosphere,

allowing for ultra-wide corrected fields. The naturally wide isoplanatic angle present at both sites means that even unconjugated adaptive optics can use wider fields than temperate sites. While it remains to be properly measured, we can expect that Dome C will have the longest coherence time measured at any site to date. This will ease the bandwidth constraints of an adaptive optics system build for this site. The optimum type of adaptive optics for Dome C remains to be determined and measurements of the ground layer turbulence will determine whether a ground layer conjugation is necessary or if the tropopause is the major layer to be corrected.

The uniqueness of the turbulence conditions in Antarctica is obviously associated to the unique climatic conditions. The simplicity of the topography is advantageous to computational hydrodynamic modeling of the turbulence field. The lack of features means that a large section of the continent could be modeled using boundary conditions such as the weather balloon data taken at Dome C and South Pole. Such computation could help us identify points of the plateau with the best seeing conditions even before sending people to new remote locations. The vastness of the continent means that we must reply on such techniques and on the correlation between turbulence and the weather parameters more easily accessible.

The future of ground based astronomy lies in Antarctica as it offers "near-space" conditions. The low temperature, pressure, turbulence and the extremely stable atmosphere will lead astronomers to build their observatories on the cold continent. We are now far from the times where the heroism of the early explorers was highlighted by the difficulty to survive, let alone operate on this continent. Antarctica is now more accessible than ever, with several countries operating successfully year-round bases. The logistics necessary to support astronomy are already well in place at the South Pole and there remain no technical barriers to exploit the advantages offered by even higher sites like Dome C.

Bibliography

A. Abahamid, A. Jabiri, J. Vernin, Z. Benkhaldoun, M. Azouit, and A. Agabi. Optical turbulence modeling in the boundary layer and free atmosphere using instrumented meteorological balloons. *AAP*, 416:1193–1200, March 2004.

A. Agabi, J. Borgnino, F. Martin, A. Tokovinin, and A. Ziad. G.s.m: A grating scale monitor for atmospheric turbulence measurements. ii. first measurements of the wavefront outer scale at the o.c.a. *AAPS*, 109:557–562, March 1995.

R. Angel, J.S. Lawrence, and J.W.V. Storey. Proceedings of the 2nd bckaskog workshop on extremely large telescopes, bckaskog castle, sweden, 9-11 september 2003. volume 406, pages 19–22, 2004.

E. Aristidi, A. Agabi, E. Fossat, T. Travouillon, M. Azouit, Vernin J., A. Ziad, F. Martin, and G. Robuchon. Site testing at dome c : seeing and isoplanatic angle in summer 2003. *AA*, in preparation, 2004.

E. Aristidi, A. Agabi, J. Vernin, M. Azouit, F. Martin, A. Ziad, and E. Fossat. Antarctic site testing: First daytime seeing monitoring at dome c. *AAP*, 406:19–22, July 2003.

E. Aristidi, K. Agabi, M. Azouit, E. Fossat, J. Vernin, T. Travouillon, J. S. Lawrence, C. Meyer, J. W. V. Storey, B. Halter, W. L. Roth, and V. Walden. An analysis of temperatures and wind speeds above Dome C, Antarctica. *aap*, 430:739–746, February 2005.

M. C. B. Ashley, P. W. Brooks, and J. P. Lloyd. Remote control of astronomical instruments via the Internet. *PASA*, 13:17–21, January 1996.

M.C.B. Ashley, M.G. Burton, P.G. Calisse, A. Phillips, and J.W.V. Storey. Site testing at dome c - cloud statisitics from the icecam experiment. *Special Session 2, 25th IAU General Assembly, Sydney July 2003, Highlights of Astronomy, ASP Conf. Series*, 13(in press), 2003.

R. Avila, J. Vernin, M. R. Chun, and L. J Sanchez. Turbulence and wind profiling with generalized scidar at cerro pachon. In *Proc. SPIE Vol. 4007, p. 721-732, Adaptive Optical Systems Technology, Peter L. Wizinowich; Ed.*, pages 721–732, July 2000.

R. Avila, J. Vernin, and S. Cuevas. Turbulence profiles with generalized scidar at san pedro mártir observatory and isoplanatism studies. *PASP*, 110:1106–1116, September 1998.

R. Avila, J. Vernin, and E. Masciadri. Whole atmospheric-turbulence profiling with generalized scidar. *AO*, 36:30, 1997.

R. Avila, J. Vernin, and L. J. Sánchez. Atmospheric turbulence and wind profiles monitoring with generalized scidar. *AAP*, 369:364–372, April 2001.

M. Azouit, J. Vernin, R. Barletti, G. Ceppatelli, and N. Righini, A.a nd Speroni. Remote sensing of atmospheric turbulence by means of a fast optical method - a comparison with simultaneous in situ measurements. *Journal of Applied Meteorology*, 19:834–838, 1980.

J. Bally, D. Theil, Y. Billawalla, D. Potter, R. F. Loewenstein, F. Mrozek, and J. P. Lloyd. A hartmann differential image motion monitor (h-dimm) for atmospheric turbulence characterisation. *PASA*, 13:22–27, January 1996.

J.E Barnes. Private communication, 2004.

P. Beckmann. *Probability in Communication Engineering*. Brace and Word, New york, 1967.

F. Beyrich. Mixing height estimation in the convective boundary layer using sodar data. *Bound.-Layer Meteor.*, 74:1–18, 1995.

M. Boccas, M. C. B. Ashley, A. Phillips, A. Schinckel, and J. W. V. Storey. Antarctic fiber optic spectrometer. *PASP*, 110:306–316, March 1998.

J. Borgnino. Estimation of the spatial coherence outer scale relevant to long baseline interferometry and imaging in optical astronomy. *AO*, 29:1863, May 1990.

J. Borgnino, M. Azouit, J. Vernin, R. Barletti, G. Ceppatelli, L. Paterno, A. Righini, and N. Speroni. Turbulence around a solar telescope as deduced from angle of arrival statistics - a comparison with microthermal measurements. *AAP*, 79:184–189, October 1979.

J. L. Bufton. Comparison of vertical profile turbulence structure with stellar observations. *AO*, 12(8):1785–1793, 1973.

M. Burton, D. K. Aitken, D. A. Allen, M. C. B. Ashley, M. G. Burton, R. D. Cannon, B. D. Carter, G. S. Dacosta, M. A. Dopita, and M. L. Duldig. The scientific potential for astronomy from the antarctic plateau. *PASA*, 11:127–150, August 1994.

M. G. Burton, M. C. B. Ashley, J. W. V. Storey, M. A. Dopita, A. Lancon, J. Mould, P. R. Wood, P. Hall, and M. Duldig. JACARA's plans. *PASA*, 13:33–34, January 1996.

P. G. Calisse, M. C. Ashley, M. G. Burton, J. R. Lawrence, M. A. Phillips, J. W. Storey, J. B. Peterson, and S. H. Radford. New submm site testing results from dome c, antarctica. *Astronomy in Antarctica, 25th meeting of the IAU, Special Session 2, 18 July, 2003 in Sydney, Australia*, 2, 2004.

M. Candidi and A. Ferrari. Concordia station at dome-c site for astronomical research. *Astronomy in Antarctica, 25th meeting of the IAU, Special Session 2, 18 July, 2003 in Sydney, Australia*, 2, 2003.

A. Capanni and G. Gualtieri. Sodar applications for estimating boundary layer parameters. In *Proc. SPIE Vol. 3866, p. 33-44, Optics in Atmospheric Propagation and Adaptive Systems III, Anton Kohnle; John D. Gonglewski; Eds.*, pages 33–44, December 1999.

M-L. Chanin. An execptional situation in the antarctic stratosphere in 2002. In E. Fossat and M. Candidi, editors, *The scientific outlook for Astronomy and Astrophysics Research at the CONCORDIA station: Recommendations for future developments*, volume 2, page 19, 2003.

C. E. Coulman, J. Vernin, and A. Fuchs. Optical seeing-mechanism of formation of thin turbulent laminae in the atmosphere. *AO*, 34:5461–+, August 1995.

K. Creath. Phase measurement interferometry techniques. In E.Wolf, editor, *Progress in Optics*, volume 26, pages 351–391, 1988.

G. H. Crescenti. A look back on two decades of doppler sodar comparison studies. *Bulletin of the American Meteorological Society*, 78:651–651, April 1997.

G.H. Crescenti. The degradation of doppler sodar performance due to noise. In *Proc., International Symposium on Measurement of Toxic and Related Air Pollutants, Durham, NC, Apr. 29-May 1, Air & Waste Management Assoc.*, pages 538–547, 1997b.

G.H. Crescenti. Some performance statistics of doppler sodars as a function of atmospheric conditions. In *Fourth International Symposium on Tropospheric Profiling: Needs and Technologies, Snowmass, CO, Sept. 21-25, Univ. Colorado,*, pages 67–69, 1998.

J. T. Dempsey, J. W. V. Storey, M. C. B. Ashley, M. G. Burton, P. G. Calisse, and M. A. Jarnyk. AFOS: probing the UV-visible potential of the Antarctic plateau. In *UV and Gamma-Ray Space Telescope Systems. Edited by Hasinger, Günther; Turner, Martin J. L. Proceedings of the SPIE, Volume 5492, pp. 811-821 (2004).*, pages 811–821, September 2004.

J. H. Doolittle. Technical report LMSC-F171145, Lockheed, 1986.

M. A. Dopita, P. R. Wood, and G. R. Hovey. An automated dimm telescope for antarctica. *PASA*, 13:39–43, January 1996.

S.A. Ehgamberdiev, A.K. Baijumanov, S.P. Ilyasov, M. Sarazin, Y.A. Tillayev, A.A. Tokovinin, and A. Ziad. *AASR*, 145:293–304, 2000.

F. F. Forbes. Near-ground atmospheric turbulence effects. In *Active telescope systems; Proceedings of the Meeting, Orlando, FL, Mar. 28-31, 1989 (A90-30852 12-74). Bellingham, WA, Society of Photo-Optical Instrumentation Engineers, 1989, p. 28-33.*, pages 28–31, September 1989.

E. Fossat, G. Grec, and M. Pomerantz. Solar pulsations observed from the geographic south pole - initial results. *Solar Physics*, 74:59–63, 1981.

D. L. Fried. Statistics of a geometric representation of wavefront distortion. *Journal of the Optical Society of America*, 55:1427–1435, 1965.

D. L. Fried. Optical resolution through a randomly inhomogeneous medium for very long and very short exposures. *Journal of the Optical Society of America Journal*, 56:1372, 1966.

D. L. Fried. Differential angle of arrival: Theory, evaluation and measurement feasibility. *Radio Science*, 10:71–76, 1975.

A. Fuchs. *Contribution a l'étude de l'apparition de la turbulence optique dans les couches minces. Concept du Scidar generalisé*. PhD thesis, Université de Nice-Sophia Anitipolis, France, 1995.

A. Fuchs, M. Tallon, and J. Vernin. Focusing on a turbulent layer: Principle of the "generalized scidar". *PASP*, 110:86–91, January 1998.

T. Fusco, J-M. Conan, V. Michau, G. Rousset, and L. Mugnier. Post-processing for anisoplanatic ao corrected images. *SPIE*, 4007:1044, 2000.

G. Grec, E. Fossat, and M. A. Pomerantz. Solar oscillations: full disk observations from the geographic south pole. *Nature*, 288(541-544), 1980.

A. E. Gur'yanov, M. A. Kallistratova, A. S. Kutyrev, I. V. Petenko, P. V. Shcheglov, and A. A. Tokovinin. The contribution of the lower atmospheric layers to the seeing at some mountain observatories. *AAP*, 262: 373–381, August 1992.

O. Hainaut. http://www.eso.org/astclim/lasilla, 2004.

C.M. Harris. Absorption of sound in air versus humidity and temperature. *Jour. Acous. Soc. Am*, 40(1):148–159, 1966.

N. Hirasawa, M. Hayashi, S. Kaneto, and T. Yamanouchi. Jare data reports 238. Technical report, Meteorology (Tokyo: Nat. Inst. of Polar Research), 1999.

R. Hosfeld. Comparisons of stellar scintillations with image motion. *JOSA*, 44:284, 1954.

B. T. Indermuehle, M. C. Burton, and S. T. Maddison. History of astrophysics in antarctica. *PASA*, 22:73–90, 2005.

L. Jolissaint, J.P. Veran, and J.A. Stoesz. Upper performance limit of wide field adaptive optics. *To be published in the proceedings of the conference 2nd Backaskog workshop on Extremely Large Telescopes, September*, 2003.

G. Y. Jumper and E. D. Murphy. Effect of balloon wake on thermosonde results. In *AIAA plasmadynamics and laser conference*, 2002.

B. Kern, T. A. Laurence, C. Martin, and P. E. Dimotakis. Temporal coherence of individual turbulent patterns in atmospheric seeing. *AO*, 39: 4879–4885, September 2000.

J.C. King and J. Turner. *Antarctic Meteorology and Climatology*. Cambridge University Press, 1997.

V. A. Klueckers, N. J. Wooder, T. W. Nicholls, M. J. Adcock, I. Munro, and J. C. Dainty. Profiling of atmospheric turbulence strength and velocity using a generalised scidar technique. *AAPS*, 130:141–155, May 1998.

A.N. Kolmogorov. *Dan.S.S.S.R.*, 30(4):229, 1941.

V. Kornilov, A. A. Tokovinin, O. Vozyakova, A. Zaitsev, N. Shatsky, S. F. Potanin, and M. S. Sarazin. Mass: a monitor of the vertical turbulence distribution. In *Adaptive Optical System Technologies II. Edited by Wizinowich, Peter L.; Bonaccini, Domenico. Proceedings of the SPIE, Volume 4839, pp. 837-845 (2003).*, pages 837–845, February 2003.

V. G. Kornilov and A. A. Tokovinin. Measurement of the turbulence in the free atmosphere above mt. maĭdanak. *Astronomy Reports*, 45:395–408, May 2001.

V. Kotroni, Y. Lemaitre, and M. Petitdidier. Dynamics of a low-level jet observed during the fronts 87 experiment. *Quart. J. Roy. Meteor. Soc.*, 120:277–303, 1994.

J. Krause-Polstorff, E. A. Murphy, and D. L. Walters. Instrument comparison - corrected stellar scintillometer versus isoplanometer. *AO*, 32: 4051–4057, July 1993.

O. Lardiere, P. Salinari, L. Jolissaint, M. Carbillet, A. Riccardi, and S. Esposito. In *Workshop on Extremely Large Telescopes, Bckaskog Castle, Sweden, 9-11 September 2003, Proc SPIE*, in press.

J. S. Lawrence. Adaptive optics performance from antarctica. *Astronomy in Antarctica, 25th meeting of the IAU, Special Session 2, 18 July, 2003 in Sydney, Australia*, 2, 2003.

J. S. Lawrence, M. C. Ashley, M. G. Burton, and J. W. Storey. The automated astrophysical site testing infant observatory. *Astronomy in Antarctica, 25th meeting of the IAU, Special Session 2, 18 July, 2003 in Sydney, Australia*, 2003.

J. S. Lawrence, M. C. B. Ashley, M. G. Burton, and J. W. V. Storey. Design and performance of the douglas mawson telescope. In *Survey and Other Telescope Technologies and Discoveries. Edited by Tyson, J. Anthony; Wolff, Sidney. Proceedings of the SPIE, Volume 4836, pp. 129-137 (2002).*, pages 129–137, December 2002.

J. S. Lawrence, M. C. B. Ashley, M. G. Burton, and J. W. V. Storey. Observations of the antarctic infrared sky spectral brightness. In *Survey and Other Telescope Technologies and Discoveries. Edited by Tyson, J. Anthony; Wolff, Sidney. Proceedings of the SPIE, Volume 4836, pp. 176-179 (2002).*, pages 176–179, December 2002b.

J. S. Lawrence, M. C. B. Ashley, A. Tokovinin, and T. Travouillon. Exceptional astronomical seeing conditions above dome c in antarctica. *Nature*, 431:278–281, September 2004a.

J.S. Lawrence. Infrared and submillimeter atmospheric characteristics of high antarctic plateau sites. *PASP*, 116:482–492, May 2004.

C.G. Little. Acoustic methods for the remote probing of the lower atmosphere. In *Proc. IEEE*, volume 57, pages 571–8, 1969.

J. P. Lloyd, B. R. Oppenheimer, and J. R. Graham. The potential of differential astrometric interferometry from the high antarctic plateau. *Publications of the Astronomical Society of Australia*, 19:318–322, 2002.

R. F. Loewenstein, C. Bero, J. P. Lloyd, F. Mrozek, J. Bally, and D. Theil. Astronomical seeing at the south pole. In *ASP Conf. Ser. 141: Astrophysics From Antarctica*, pages 296–+, 1998.

G. C. Loos and C. B. Hogge. Turbulence of the upper atmosphere and isoplanatism. *AO*, 18:2654, August 1979.

S.D Lord. A new software tool for computing earth's atmospheric transmission of near and far-infrared radiation. Technical report, NASA-TM-103957, 1993.

R.F. Lutomirski and H.T. Yura. *J. Opt. Soc. Am.*, 61:482, 1971.

R. D. Marks, J. Vernin, M. Azouit, J. W. Briggs, M. G. Burton, M. C. B. Ashley, and J. F. Manigault. Antarctic site testing - microthermal measurements of surface-layer seeing at the south pole. *AAPS*, 118:385–390, August 1996.

R. D. Marks, J. Vernin, M. Azouit, J. F. Manigault, and C. Clevelin. Measurement of optical seeing on the high antarctic plateau. *AAPS*, 134: 161–172, January 1999.

F. Martin, R. Conan, A. Tokovinin, A. Ziad, H. Trinquet, J. Borgnino, A. Agabi, and M. Sarazin. Optical parameters relevant for high angular resolution at paranal from gsm instrument and surface layer contribution. *AAPS*, 144:39–44, May 2000.

F. Martin, A. Tokovinin, A. Agabi, J. Borgnino, and A. Ziad. G.s.m.: a grating scale monitor for atmospheric turbulence measurements. i. the instrument and first results of angle of arrival measurements. *AAPS*, 108: 173–180, November 1994.

H. M. Martin. Image motion as a measure of seeing quality. *PASP*, 99: 1360–1370, December 1987.

E. Masciadri, R. Avila, and L. J. Sanchez. 3d optical turbulence characterization for the new class of adaptive optics techniques. In *Beyond conventional adaptive optics : a conference devoted to the development of adaptive optics for extremely large telescopes. Proceedings of the Topical Meeting held May 7-10, 2001, Venice, Italy. Edited by E. Vernet,*

R. Ragazzoni, S. Esposito, and N. Hubin. Garching, Germany: European Southern Observatory, 2002 ESO Conference and Workshop Proceedings, Vol. 58, ISBN 3923524617, p. 361, pages 361–+, 2002.

E. Masciadri, R. Avila, and L. J. Sánchez. First evidence of the finite horizontal extent of the optical turbulence layers. implications for new adaptive optics techniques. *AAP*, 382:378–388, January 2002.

G. Mastrantonio, V. Malvestuto, S. Argentini, T. Georgiadis, and A. Viola. Evidence of a convective boundary layer developing on the antarctic plateau during the summer. *Meteorol Atmos. Phys.*, 71:127–132, 1999.

T. Mefford. Noaa cmdl, http://www.cmdl.noaa.gov, 2004.

F. Murtagh and M. Sarazin. Nowcasting astronomical seeing - a study of eso la silla and paranal. *PASP*, 105:932–939, September 1993.

W. D. Neff. *An observational and numerical study of the atmospheric boundary layer overlying the East Antarctic ice sheet.* PhD thesis, Wave propagation Laboratory, Colorado, 1981.

W.D. Neff. Observations of complex terrain flows using acoustic sounders: Echo interpretation. *Bound.-Layer Meteor.*, 42:207–228, 1988.

A.M. Obukhov. *Izv. Akad. Nauk S.S.S.R., Ser Geograf. Geofiz.*, 13(58), 1949.

G. R. Ochs, T. Wang, R. S. Lawrence, and S. F. Clifford. Refractive-turbulence profiles measured by one-dimensional spatial filtering of scintillations. *AO*, 15:2504–2510, October 1976.

S. P. Oncley. Flux parameterization techniques in the atmospheric surface layer. *Ph.D. Thesis*, March 1989.

P. Pant, C. S. Stalin, and R. Sagar. Microthermal measurements of surface layer seeing at devasthal site. *AAPS*, 136:19–25, April 1999.

P. Paranthoen. Systeme d'etalonnage dynamique des thermometres a fil froid. Technical report, In. Report. Lab. de Thermodynamique. Universite de Rouen, 1985.

T.R. Parish and D.H. Bromwich. The surface windfield over the antarctic ice sheets. *Nature*, 328:51–54, 1987.

T.R. Parish and J.J Cassano. Diagnosis of the katabatic wind influence on the wintertime antarctic surface wind field from numerical simulations. *Monthly Weather Review*, 131:1128, 2002.

J. Peterson and S. Radford. Submillimeter Opacity and Stability at the South Pole. *Astronomy in Antarctica, 25th meeting of the IAU, Special Session 2, 18 July, 2003 in Sydney, Australia*, 2, 2003.

P. Pettré and S. Argentini. On the vertical velocity sodar measurement in the region of dumont d'urville, east antarctica. *GRL*, 28:783–+, March 2001.

M. A. Pomerantz. Interview with m. a. pomerantz conducted in his san rafael, california home on may 10, 2000. Polar Oral History Program, The Ohio State University Archives, 2000.

J.-L. Prieur, G. Daigne, and R. Avila. Scidar measurements at pic du midi. *AAP*, 371:366–377, May 2001.

R. Racine. Temporal fluctuations of atmospheric seeing. *PASP*, 108:372–+, April 1996.

R. Racine and B. L. Ellerbroek. Profiles of nighttime turbulence above mauna kea and isoplanatism extension in adaptive optics. In *Proc. SPIE Vol. 2534, p. 248-257, Adaptive Optical Systems and Applications, Robert K. Tyson; Robert Q. Fugate; Eds.*, pages 248–257, August 1995.

F.M. Ralph, C. Mazaudier, M. Crochet, and S.V. Venkateswaran. Doppler sodar and radar wind profiler observations of gravity waves activity associated with a gravity current. *Mon. Wea. Rev.*, 121:444–463, 1993.

J.M. Rees and S.D. Mobbs. *Q. J. R. Meteorol. Soc.*, 114(939-966), 1988.

F. Rigaut. Ground-conjugate wide field adaptive optics for the elts. In Ragazzoni R. Esposito S. Hubin N. Vernet, E., editor, *Behond Conventional Adaptive Optics*, volume 58 of *ESO Conference & Workshop Proceedings*, pages 11–16, 2001.

A. Rocca, F. Rodier, and J. Vernin. Detection of atmospheric turbulent layers by patiotemporal and spatioangular correlation measurements of stellar-ligth scintillation. *JOSA*, 64:1000, 1974.

F. Roddier. The effects of atmospheric turbulence in optical astronomy. In *Progress in optics. Volume 19. Amsterdam, North-Holland Publishing Co., 1981, p. 281-376.*, pages 281–376, 1981.

F. Roddier, L. Cowie, J. E. Graves, A. Songaila, and D. McKenna. Seeing at mauna kea - a joint uh-un-noao-cfht study. In *Advanced technology optical telescopes IV; Proceedings of the Meeting, Tucson, AZ, Feb. 12-16, 1990. Part 1 (A91-23201 08-89). Bellingham, WA, Society of Photo-Optical Instrumentation Engineers, 1990, p. 485-491.*, pages 485–491, July 1990.

L. J. Sánchez, D. X. Cruz, R. Avila, A. Agabi, M. Azouit, S. Cuevas, F. Garfias, S. I. González, O. Harris, E. Masciadri, V. G. Orlov, J. Vernin, and V. V. Voitsekhovich. Contribution of the surface layer to the seeing at san pedro mártir: Si-mul-ta-neous microthermal and dimm measurements. In *Revista Mexicana de Astronomia y Astrofisica Conference Series*, pages 23–30, September 2003.

M Sarazin. Site atmospheric characterization. In M. Cullum-ESO, editor, *AO'95: Adaptive Optics Topical Meeting*, Garching, October 2-6 1995.

M. Sarazin and F. Roddier. The eso differential image motion monitor. *AAP*, 227:294–300, January 1990.

M. S. Sarazin. Automated seeing monitoring for queue-scheduled astronomical observations [3125-40]. In *Proc. SPIE Vol. 3125, Progagation and Imaging Through the Atmosphere, Luc R. Bossonnette and Christopher Dainty, Eds., p.366*, pages 366–+, 1997.

W. Schwerdtfeger. *Weather and Climate of the Antarctic*. Number 15 in Developments in atmospheric science. Elsevier, 1984.

C. S. Stalin, R. Sagar, P. Pant, V. Mohan, B. Kumar, Y. C. Joshi, R. K. S. Yadav, S. Joshi, R. Chandra, A. K. Durgapal, and W. Uddin. Seeing and microthermal measurements near devasthal top. *Bulletin of the Astronomical Society of India*, 29:39–52, March 2001.

C. R. Stearns, L. M. Keller, G. A. Weidner, and M. Sievers. Monthly mean climatic data for antarctic automatic weather stations. In D. H. Bromwich and C. R. Streans, editors, *Antarctic meteorology and climatology: Studies based on automatic weather stations*, volume 61 of *Antarctic research*, pages 1–21, 1993.

J. Stock and G. Keller. *Stars and Stellar Systems*, volume 1, page 138. Uni. Chicago Press, 1960.

J. W. V. Storey, M. C. B. Ashley, M. Boccas, M. A. Phillips, and A. E. T. Schinckel. Infrared sky brightness monitors for antarctica. *PASP*, 111: 765–771, June 1999.

J. W. V. Storey, M. C. B. Ashley, and M. G. Burton. An automated astrophysical observatory for antarctica. *PASA*, 13:35–38, January 1996.

I.E. Tabacco, A. Passerini, F. Corbelli, and M.R. Gorman. Determination of the surface and bed topography at dome concordia. Private communication, 2002.

V.I. Tatarski. *Wave propagation in a turbulent medium*. Dover, New York, 1961.

A. Tokovinin. From differential image motion to seeing. *PASP*, 114:1156–1166, October 2002.

A. Tokovinin. Measurement of seeing and the atmospheric time constant by differential scintillations. *AO*, 41:957–964, February 2002b.

A. Tokovinin. New instruments to see the seeing. Technical report, Article in NOAO/NSO Newsletter 77, 32-34, 2004.

A. Tokovinin. Seeing improvement with ground-layer adaptive optics. *PASP*, submitted, 2004b.

A. Tokovinin, S. Baumont, and J. Vasquez. Statistics of turbulence profile at cerro tololo. *MNRAS*, 340:52–58, March 2003.

A. Tokovinin, V. Kornilov, N. Shatsky, and O. Voziakova. Restoration of turbulence profile from scintillation indices. *MNRAS*, 2003.

A. A. Tokovinin. A new method of measuring atmospheric seeing. *Astronomy Letters*, 1998.

A. A. Tokovinin, A. Ziad, F. Martin, R. Avila, J. Borgnino, R. Conan, and M. S. Sarazin. Wavefront outer-scale monitoring at la silla. In *Proc. SPIE Vol. 3353, p. 1155-1162, Adaptive Optical System Technologies, Domenico Bonaccini; Robert K. Tyson; Eds.*, pages 1155–1162, September 1998.

T. Travouillon, M. C. B. Ashley, Burton M. G., J.S. Lawrence, and J. W. V. Storey. Low atmosphere turbulence at dome c. preliminary results. *Societa Astronomica Italiana Memorie Supplement*, 2:150–+, 2003.

T. Travouillon, M.C.B. Ashley, M.G. Burton, J.W.V. Storey, P. Conroy, G. Hovey, M. Jarnyk, R. Sutherland, and R.F. Loewenstein. Automated shack-hartmann seeing measurements at the south pole. *AAP*, 409:1169–1173, October 2003a.

T. Travouillon, M.C.B. Ashley, M.G. Burton, J.W.V. Storey, and R.F. Loewenstein. Atmospheric turbulence at the south pole and its implications for astronomy. *AAP*, 400:1163–1172, March 2003b.

J. Vernin. Astronomical site selection - a new meteorological approach. In *Proc. SPIE.*, volume 628, pages 142–147, 1986.

J. Vernin. Mechanism of formation of optical turbulence (invited speaker). In *ASP Conf. Ser. 266: Astronomical Site Evaluation in the Visible and Radio Range*, pages 2–+, 2002.

J. Vernin and M. Azouit. Image processing adapted to the atmosphere speckle. i. speckle formation in turbulent atmosphere. statistical properties. *Journal of Optics*, 14:5–9, January 1983.

J. Vernin and M. Azouit. Image processing adapted to the atmospheric speckle. ii. remote sounding of turbulence by means of multidimensional analysis. *Journal of Optics*, 14:131–142, May 1983b.

J. Vernin and C. Munoz-Tunon. Optical seeing at La Palma Observatory. I - General guidelines and preliminary results at the Nordic Optical Telescope. *AAP*, 257:811–816, April 1992.

J. Vernin and C. Munoz-Tunon. Optical seeing at la palma observatory. 2: Intensive site testing campaign at the nordic optical telescope. *AAP*, 284: 311–318, April 1994.

J. Vernin and C. Munoz-Tunon. Measuring astronomical seeing: The da/iac dimm. *PASP*, 107:265–272, March 1995.

J. Vernin and C. Muñoz-Tuñón. The temporal behaviour of seeing. *New Astronomy Review*, 42:451–454, November 1998.

J. Vernin and F. Roddier. Experimental determination of two-dimensional spatiotemporal power spectra stellar light scintillation. evidence for a multiplayer structure of the air turbulence in the upper troposphere. *JOSA*, 63:3, 1973.

V. P. Walden, M. S. Town, B. Halter, and J. W. V. Storey. First Measurements of the Infrared Sky Brightness at Dome C, Antarctica. *pasp*, 117: 300–308, March 2005.

R. W. Wilson. Slodar: measuring optical turbulence altitude with a shackhartmann wavefront sensor. *MNRAS*, 337:103–108, November 2002.

R.W. Wilson. private communication. 2004.

A. M. Yaglom. *Dan. S.S.S.R.*, 69(6):743, 1949.

C. Yague, G. Maqueda, and J. M. Rees. *Dynamics of Atmospheres and Oceans*, 34(2-4):205–223, 2001.

A Ziad. *Estimation des echelles limites de coherence spatiale des fronts d'onde et optimisation des observations a haute resolution angulaire en astronomie.* PhD thesis, Universite de Nice, Departement d'Astrophysique, 1993.

A. Ziad, R. Conan, A. Tokovinin, F. Martin, and J. Borgnino. From the grating scale monitor to the generalized seeing monitor. *AO*, 39:5415–5425, October 2000.

A. Ziad, A. Jabiri, Z. Benkhaldoun, F. Martin, R. Conan, M. Lazrek, and J. Borgnino. The first optical characterization of the oukaimeden site with the generalized seeing monitor (gsm). *AAP*, 365:324–329, January 2001.